

---

# Wideband Impedance Boundary Conditions for FE/DG Methods for Solving Maxwell Equations in Time Domain

---

Zur Erlangung des akademischen Grades Doktor-Ingenieur (Dr.-Ing.)  
genehmigte Dissertation von M.Sc. Irene Woyna aus Tampere, Finnland  
Juni 2014 — Darmstadt — D 17



TECHNISCHE  
UNIVERSITÄT  
DARMSTADT

Fachbereich Elektrotechnik und  
Informationstechnik  
Institut für Theorie Elektromag-  
netischer Felder (TEMF)

Wideband Impedance Boundary Conditions for FE/DG Methods for Solving  
Maxwell Equations in Time Domain

Vom Fachbereich Elektrotechnik und Informationstechnik der Technischen Uni-  
versität Darmstadt zur Erlangung des akademischen Grades eines Doktor-  
Ingenieurs (Dr.-Ing.) genehmigte Dissertation von M.Sc. Irene Woyna aus Tam-  
pere, Finnland

1. Gutachten: Prof. Dr.-Ing. Thomas Weiland
2. Gutachten: Prof. Dr.-Ing. Irina Munteanu

Tag der Einreichung: 19.11.2013

Tag der Prüfung: 21.5.2014

Darmstadt, 2014 — D 17



---

Erklärung laut §9 PromO

---

Ich versichere hiermit, dass ich die vorliegende Dissertation allein und nur unter Verwendung der angegebenen Literatur verfasst habe. Die Arbeit hat bisher noch nicht zu Prüfungszwecken gedient.

Darmstadt 11.11.2013

Irene Woyna, M.Sc.

---

# Contents

1. Introduction	7
1.1. Motivation	7
1.2. Related Works	9
1.3. Outline	11
2. Continuous Electrodynamics	13
2.1. Maxwell's Equations	13
2.2. Constitutive Relations	16
2.3. Boundary Conditions	17
2.3.1. Magnetic Flux Density	18
2.3.2. Displacement Field	19
2.3.3. Electric Field	19
2.3.4. Magnetic Field	20
2.4. Electromagnetic Wave Equation	21
2.5. Electromagnetic Wave at Interface	22
2.5.1. Dielectric - Dielectric	23
2.5.2. Dielectric - Conductor	24
2.6. Conservation Laws	29
2.6.1. Poynting's Theorem	29
2.6.2. Current Continuity	30
3. Discrete Electrodynamics	32
3.1. Introduction	32
3.2. Finite Element Method	33
3.2.1. Mesh	34
3.2.2. Basis Functions	34
3.3. DG-FEM for Maxwell's Equations	36
3.4. Discretization of Time	39
3.4.1. Leapfrog Integration	39
3.4.2. Verlet Integration	40
4. Dispersive Boundary Conditions in Frequency Domain	41
4.1. Introduction	41

---

4.2.	Standard Impedance Boundary Condition (SIBC) . . . . .	42
4.2.1.	Skin Effect . . . . .	42
4.2.2.	Surface Impedance . . . . .	44
4.3.	Corrugated Surface Boundary Condition (CSBC) . . . . .	46
4.4.	Impedance Transmission Boundary Condition (ITBC) . . . . .	48
4.4.1.	Two-Port Transmission Line . . . . .	49
4.4.2.	Thin Conductive Sheet . . . . .	51
4.5.	Dispersive Boundary Conditions for DG-FEM . . . . .	52
4.5.1.	SIBC . . . . .	53
4.5.2.	CSBC . . . . .	57
4.5.3.	ITBC . . . . .	58
4.6.	FD Solver Implementation . . . . .	60
4.7.	Numerical Examples . . . . .	63
4.7.1.	Resonator Losses . . . . .	64
4.7.2.	Resonator with Lossy Walls . . . . .	66
4.7.2.1.	Q Factor of Cavity Resonator . . . . .	66
4.7.2.2.	SIBC Convergence Study . . . . .	68
4.7.2.3.	CSBC Convergence Study . . . . .	69
4.7.3.	Resonator Partitioned by Thin Conductive Sheet . . . . .	73
4.7.3.1.	Effect of Sheet Thickness . . . . .	75
4.7.3.2.	ITBC Convergence Study . . . . .	77
5.	Dispersive Boundary Conditions in Time Domain . . . . .	84
5.1.	Introduction . . . . .	84
5.1.1.	Significance of Dispersivity in TD Simulations . . . . .	85
5.2.	Rational Approximation of Impedance Functions in FD . . . . .	87
5.3.	Transform from FD into TD . . . . .	92
5.3.1.	Linearity and Causality of a Physical System . . . . .	92
5.3.2.	Laplace Transform . . . . .	93
5.3.3.	Recursive Convolution (RC) . . . . .	94
5.3.4.	Auxiliary Differential Equation (ADE) . . . . .	96
5.4.	TD Solver Implementation . . . . .	98
5.4.1.	DG-FEM in Time Domain with RC . . . . .	99
5.4.2.	DG-FEM in Time Domain with ADE . . . . .	101
5.4.3.	Comparison of ADE and RC Methods . . . . .	102
5.5.	Numerical Examples . . . . .	105
5.5.1.	Prony's Method . . . . .	106
5.5.2.	Cavity Resonator with Lossy Walls . . . . .	107
5.5.2.1.	Q factor of Cavity Resonator . . . . .	107

---



5.5.2.2. SIBC Convergence Study . . . . .	109
5.5.2.3. Accuracy and Performance of ADE and RC . . .	112
6. Summary . . . . .	123
6.1. Conclusion . . . . .	123
6.2. Outlook . . . . .	125
A. Appendix . . . . .	126
B. Register . . . . .	128
Acronyms . . . . .	131

---

# Abstract

In this work, dispersive surface impedance boundary conditions are applied to Discontinuous Galerkin Method (DG-FEM) in the time and frequency domains, on a wide frequency band. Three different kinds of surface impedance boundary conditions are considered, namely Standard Impedance Boundary Condition (SIBC) for modeling smooth conductor surfaces with high conductivity, Corrugated Surface Boundary Condition (CSBC) for modeling corrugated conducting surfaces, and Impedance Transmission Boundary Condition (ITBC) for modeling electrically thin conductive sheets.

Two different schemes for modeling dispersive surface impedance boundary conditions on a wide frequency band are presented, one in the frequency domain, and another in the time domain. In the frequency domain, a procedure for solving a complex nonlinear eigenvalue problem (EVP) arising from applying the dispersive impedance boundary conditions to the discrete Maxwell's equations, is presented. The procedure is based on fixed point iteration, and it enables to solve for the nonlinear EVP as a linear EVP, and therefore to simplify the computational task significantly. In the time domain scheme, the dispersive boundary conditions are first approximated in the frequency domain as series of rational functions, and then transformed into the time domain by means of Laplace transform. The time stepping schemes for time domain simulations are obtained by means of Recursive Convolution (RC) and Auxiliary Differential Equation (ADE) methods.

The frequency domain scheme, as well as the time domain scheme, are verified and validated by investigating the Q factors and the fundamental frequencies of different resonant structures. Numerical examples are given, and convergence studies are performed. The results are compared with the analytical results, as well as results obtained by commercial softwares. The developed schemes appear to be computationally efficient, and the accuracy very high, already with coarse meshes and low basis function orders.

---

# Zusammenfassung

Die vorliegende Arbeit zentralisiert die Anwendung dispersiver Oberflächenimpedanz-Randbedingung in einem breiten Frequenzbereich auf die diskontinuierliche Galerkin Methode (DG-FEM) im Zeit- und Frequenzbereich. Dabei werden mit der Standard Impedance Boundary Condition (SIBC) zur Modellierung glatter Leiteroberflächen hoher Leitfähigkeit, der Corrugated Surface Boundary Condition (CSBC) zur Modellierung rauher Leiteroberflächen sowie der Impedance Transmission Boundary Condition (ITBC) zur Modellierung elektrisch dünner Leiterscheiben drei verschiedene Oberflächen-Impedanz-Randbedingungen untersucht.

Zur Modellierung dispersiver Oberflächenimpedanz-Randbedingungen in einem breiten Frequenzbereich werden Methoden sowohl im Zeit- als auch im Frequenzbereich betrachtet. Im Frequenzbereich wird eine Lösungsmethode komplexer, nichtlinearer Eigenwert Probleme (EVP) beschrieben, welche auf der Anwendung dispersiver Oberflächenimpedanz-Randbedingungen auf die diskrete Maxwell-Gleichung basiert. Hierbei wird das nichtlineare Eigenwertproblem mittels Fixpunktiteration in ein lineares Eigenwertproblem überführt, was den numerischen Lösungsprozess erheblich vereinfacht. Bei der Methode im Zeitbereich werden die dispersiven Randbedingungen zunächst als Folge rationaler Funktionen in den Frequenzbereich approximiert, bevor sie mit Hilfe der Laplace-Transformation in den Frequenzbereich zurücktransformiert werden. Die verwendeten Zeitschrittverfahren der Zeitbereichssimulation ergeben sich aus der Recursive Convolution (RC) und der Auxiliary Differential Equation (ADE) Methode.

Die dargestellten Frequenz- und Zeitbereichsmethoden werden in einer Untersuchung des Q-Faktors sowie der Grundfrequenzen verschiedener Resonatoren verifiziert und validiert. Neben numerischen Beispielen werden Konvergenzstudien durchgeführt, deren Ergebnisse sowohl mit dem analytisch gewonnen Ergebnis als auch mit dem Ergebnis kommerzieller Softwareprogrammen verglichen werden. Die entwickelten Methoden erweisen sich numerisch effizient und zeigen bereits bei groben Gittern und Basisfunktionen niedriger Ordnung eine hohe Genauigkeit.



---

# 1 Introduction

In this chapter, the introduction for the thesis is given. First, the motivation for the topic of the thesis is explained, and the research question is placed. Secondly, as a state of the art, a literature review of the topics directly related to the thesis is given. Thirdly, after the state of the art, the outline of the thesis is given.

---

## 1.1 Motivation

---

The Maxwell's equations form the basis of electrodynamics. Solving for the Maxwell's equations analytically is possible only in a few special cases. Therefore, in general, one needs to resort to numerical methods to find the solution for the Maxwell's equations. Solving the Maxwell's equations numerically is known as electromagnetic modeling. In a nutshell, electromagnetic modeling can be considered as approximating and solving the Maxwell's equations in a computational domain, which imitates the reality. Electromagnetic modeling can be divided into three phases: Pre-processing, solving, and post-processing.

Preprocessing phase includes the choice of the numerical modeling method, based on the problem type, as well as discretization of the computational domain and time. In pre-processing phase, several simplifications can be done to save memory and computing time. The computational domain can be truncated due to symmetry, and often also the dimensionality can be reduced from 3D to 2D, or 1D. The domain can be truncated also by boundary conditions. Widely used boundary conditions are e.g. Perfect Electric Conductor (PEC) for excluding perfect (or almost perfect) conductors from the computational domain, and Absorbing Boundary Condition (ABC) or Perfectly Matched Layer (PML) to avoid modeling of free space surrounding the structure to be modeled. A third type of commonly used boundary conditions surface impedance boundary conditions, which enable excluding imperfectly conducting bodies from the computational domain. Further problem simplifications, include reduction of the Maxwell's equations. Terms of the Maxwell's equations can be dropped out e.g. depending on the frequency scale of the problem in hand, or conductivity of the structures to be modeled. E.g. if the frequencies are low, the time dependencies of the Maxwell's equations can be dropped out, and the problem reduces into quasistatic or static problem.

---

Solving includes, as the name suggests, solving for the Maxwell's equations with possible simplifications done in the pre-processing phase. Solving methods can be roughly divided into time domain and frequency domain methods. Solving is typically the most time consuming part of electromagnetic modeling, and therefore a suitable choice of solving method is important. Also the aforementioned choices made in pre-processing phase are important to diminish the solving time. Post-processing phase consists of processing of data given by the solving process. The outputs of the solving process are typically electromagnetic fields or potentials. Often in post-processing phase some other data is calculated from the primary data. These secondary data include e.g. scattering parameters, radar cross section, Lorentz forces, or quality factors, just to mention a few.

This thesis focuses on SIBC boundary conditions in the time domain, i.e. especially in the preprocessing and solving phases of the electromagnetic modeling flow. Modeling of conductors in a computational domain is expensive, since the mesh needed for resolving the conductors is very dense compared to the mesh without conductors. A dense mesh leads to a high memory consumption, and, in the time domain, additionally to a small time step, and therefore to long simulation times. For these reasons, it is highly desirable to exclude the conductors from the computational domain. This can be done by removing the conducting medium from the computational domain, and replacing the surface of the conductor with a sufficient boundary condition. In general, surface impedance boundary conditions include impedance functions, which are functions of frequency, i.e. the impedance functions are dispersive. This makes the impedance boundary conditions straightforwardly suitable for frequency domain simulations. However, in the time domain, applying surface impedance boundary conditions is somewhat more complicated.

Many electromagnetic problems, e.g. problems including transient signals, consist of a wide band of frequencies. Solving for the wideband electromagnetic problems is typically done in the time domain, since time domain simulations allow for solving for the whole frequency band at a single simulation run. When impedance boundary conditions are applied to a wideband electromagnetic problem, taking the dispersivity of the impedance functions into account is especially important to obtain correct results. Applying dispersive surface impedance boundary conditions to time domain simulations requires an approximation of the functions associated with impedance boundary conditions. This approximation is a

---

trade-off between the accuracy of the approximations, the required computational resources, and the width of the frequency band.

In this thesis, the focus is on pre-processing and solving phases of the electromagnetic modeling flow. The aim of the thesis is the truncation of the computational domain, by excluding imperfectly conductive bodies from the computational domain by utilizing dispersive surface impedance boundary conditions. Different kinds of surface impedance boundary conditions are applied, and the dispersivity of the boundary conditions is considered. Furthermore, schemes for solving the Maxwell's equations with dispersive surface impedance boundary conditions on a wide frequency band, in frequency and time domains are introduced. The target of the thesis can be summarized in the following research question: How to model dispersive surface impedance boundary conditions accurately and efficiently on a wide frequency band? Before moving to answering the question, in the following sections, a state of the art, and an outline of the thesis are given.

---

## 1.2 Related Works

---

Finite Element Method (FEM) [103] is a widely known and used numerical method in electrodynamics. It is very accurate in modeling complex geometries and an efficient tool for solving electromagnetic problems in the frequency domain in scientific applications, as well as in commercial softwares. However, applying FEM to the time domain leads to implicit and therefore unefficient time-stepping scheme.

In contrast, Finite-Difference Time-Domain Method (FDTD) [99] and Finite Integration Technique (FIT) [96] are very efficient in time domain simulations, since the obtained time-stepping scheme is explicit. Additionally, FDTD/FIT methods are very intuitive, and therefore the implementation is straightforward. FDTD/FIT methods are extremely widely used, also in commercial softwares. However, both of the methods are at most second order accurate, and modeling arbitrary structures is not accurate. Also modeling of boundaries can be inaccurate, since the electric and magnetic fields are not colocated in the computational mesh.

Discontinuous Galerkin Finite Element Method (DG-FEM) [97], [18], [17], [47], [48] had increased its popularity recently in electromagnetic simulations. It combines the advantages of FEM and FDTD/FIT methods, i.e. the modeling of arbitrary structures is accurate, and the time domain scheme is explicit and

---

therefore efficient. A major disadvantage of DG-FEM method is, that it can cause so called spurious modes to the solution [92]. However, several schemes exists to overcome this problem, given in e.g. [46], [23], [33], [13], [14], [2].

Standard Impedance Boundary Condition (SIBC) connects the tangential electric field with the tangential magnetic field on the surface of a conductor. Applying SIBC allows for excluding the conductor from the computational domain, and makes the simulations significantly cheaper. In its simplest, first order form [59], [88], SIBC takes into account the material parameters of the conductor, and it is sufficiently accurate, especially with high-frequency simulations [51]. Also higher order SIBCs exists [85], [69]. They consider also the curvature of the conductor surface, as well as the variation of electromagnetic field in the tangential direction, unlike first order SIBC.

SIBCs are capable to model thick conductors [90], i.e. conductors, whose thickness is significantly larger than the skin depth at the frequency in question. If the thickness of the conductor is of similar magnitude as the skin depth, the conductor becomes partially transparent for the electromagnetic field and the SIBC model fails [90]. To model thin conductive sheets, the transmission line theory can be exploited, as done in e.g. [50], [1], and [87]. The theory has been applied in electromagnetic modeling in e.g. [95], [26], [25], [86], and [63] with FDTD method. Within this thesis, the transmission line theory based boundary condition, used for modeling thin conductive sheets, is referred to as Impedance Transmission Boundary Condition (ITBC).

When the surface of the conductor is not smooth, standard SIBC and ITBC underestimate the losses on the surface, and are therefore not accurate. These rough surfaces are referred to as Corrugated Surfaces (CS) within this thesis, and the boundary condition used to model the rough surfaces to as Corrugated Surface Boundary Condition (CSBC). Modeling of CSs is based on the theory presented in [70], [27], and [16]. Hammerstad [44] empirically fitted a function to model corrugated surfaces based on the theory. His approach have been applied in electromagnetic modeling in e.g. [61]. Also other empirical models have been developed and applied in electromagnetic simulations, see e.g. [65], [79], [89], [43], [36], [15]. Furthermore, models for 2D surface roughnesses are presented in [94] and [49].

SIBC, ITBC, and CSBC connect the tangential electric field with the tangential magnetic field on the surface of a conductor via a frequency dependent, or dis-

---

persive, impedance functions [88], [50], [44]. Therefore, they are straightforward to apply in frequency domain simulations as done in e.g. [53], [100], [57], and [60].

In the time domain, modeling of dispersive boundary conditions becomes more complicated. The dispersivity of the impedance function can be considered by e.g. Auxiliary Differential Equation (ADE) methods. Although in this thesis the idea is to exclude the dispersive media from the computational domain, the methods for modeling dispersive media can be applied as well. A few research works, in which ADE method is used for modeling dispersive media are e.g. [93], [31], [81]. ADE method is also used for modeling open boundary conditions, such as PML, in e.g. [76] and [32]. Another popular method to take the dispersivity into account, is Recursive Convolution (RC) method [71]. RC method have been widely applied for FDTD/FIT methods to model SIBC and ITBC in the time domain: [86], [95], [20], [102], [66], [55], [3], as well as modeling open boundary conditions as ABC in e.g. [9]. Different approaches to model dispersive boundary conditions are given in e.g. [6], [5], [67]. Higher order SIBC is considered for FDTD method in e.g. [28]. Another methods for modeling dispersive media are proposed in e.g. [64], [29], [42] and [62].

Regardless of the popularity of utilizing FDTD/FIT in electromagnetic modeling and applying impedance boundary conditions, the disadvantages of the methods remain: The poor performance in modeling complex geometries and boundaries. Therefore it would be desirable to utilize the impedance boundary conditions in FEM method, and in the time domain especially in DG-FEM method. Impedance boundary conditions with FEM/DG-FEM are presented in e.g. [12], [4], [56], [77], [41] and [82]. However, these papers consider magnetoquasistatic problems, i.e. they exclude high-frequency applications and full-wave equations. Additionally, in [83], time domain FEM formulations for different thin conductive sheets are presented, but the dispersivity of the functions is not considered. In [30], [35] open boundary conditions are modeled in the time domain with DG-FEM.

---

### 1.3 Outline

---

After this introduction, the rest of the thesis is organized as follows: Chapter 2 explains the basis of electromagnetic theory, namely the Maxwell's equations. Additionally, analytic boundary conditions and conservation laws are introduced, focusing on the essential aspects for this thesis. Chapter 3 gives the overview of the topics of discrete electrodynamics which are important in this thesis, includ-

---

ing spatial discretization of the computational domain by means of FEM/DG-FEM, as well as temporal discretization of an electromagnetic problem by means of Leapfrog and Verlet integration.

In Chapter 4, a detailed description of selected frequency dependent impedance boundary conditions is given, namely SIBC, ITBC and CSBC. The theory behind these boundary conditions, as well as applying these dispersive boundary conditions in frequency domain electromagnetic modeling, is explained. Additionally, and the most importantly, a novel scheme to solve for the wideband electromagnetic problems iteratively in the frequency domain with DG-FEM and dispersive impedance boundary conditions is proposed. Finally, the proposed scheme is verified by numerical examples and convergence studies.

First, Chapter 5 describes methods to approximate the frequency dependent impedance functions in the frequency domain. Second, the transformation from frequency domain to time domain is explained, and two different methods, namely ADE and RC are introduced. Thirdly, and most importantly, a novel semi-implicit scheme for solving for the electromagnetic problems in the time domain with dispersive boundary conditions with DG-FEM in the time domain is proposed, and the scheme is verified by numerical examples and convergence studies.

In Chapter 6, the summary of the thesis, as well as the outlook, are given. Also the contribution of the author is clarified.

---

## 2 Continuous Electrodynamics

In this chapter, some basic concepts of the electromagnetic theory are recalled. The chapter is kept relatively short, and it gives only an overview on the important aspects of the electromagnetic theory concerning this thesis. To get more detailed understanding about the topics in this chapter, the author recommends the book "Foundations of Electromagnetic Theory" by John R. Reitz et. al. [80].

In addition to the Maxwell's equations, the most important topic for the rest of the thesis is can be found in Section 2.5.2. The section describes the behaviour of the electromagnetic wave on the interface of dielectric and conductor. This topic is relatively rarely found in the literature, while refreshing exception being the book "Electromagnetic Theory" by Julius A. Stratton [91].

---

### 2.1 Maxwell's Equations

---

The Maxwell's equations form the foundation of classical electrodynamics. The Maxwell's equations are a mathematical expression for certain experimental results, and cannot be derived from other laws of nature. The differential form of Maxwell's equations in a macroscopic<sup>1</sup> form read:

$$\nabla \times \vec{E} = -\frac{\partial \vec{B}}{\partial t} \quad (2.1)$$

$$\nabla \times \vec{H} = \vec{J}_f + \frac{\partial \vec{D}}{\partial t} \quad (2.2)$$

$$\nabla \cdot \vec{B} = 0 \quad (2.3)$$

$$\nabla \cdot \vec{D} = \rho_f. \quad (2.4)$$

Equation (2.1) is known as Faraday's law, (2.2) as Ampère's law, (2.3) as Gauss' law for magnetic fields, and (2.4) as Gauss' law for electric fields. The vector fields in Equations (2.1)-(2.4) and their units are the following:

---

<sup>1</sup> Maxwell's equations in macroscopic scale factor out the bounded charges and currents i.e. those induced by magnetization and polarization of the medium

$$\vec{E} \quad \text{Electric field (strength)} \quad [\text{V/m}] \quad (2.5)$$

$$\vec{D} \quad \text{(Electric) displacement field} \quad [\text{C/m}^2] \quad (2.6)$$

$$\vec{H} \quad \text{Magnetic field (strength)} \quad [\text{A/m}] \quad (2.7)$$

$$\vec{B} \quad \text{Magnetic flux density} \quad [\text{T}]. \quad (2.8)$$

Additionally,  $\vec{J}_f$  is the free electric current density and  $\rho_f$  the free electric charge density. Free densities mean that the bounded current or charge densities caused by the polarization or magnetization of the medium are excluded. Let  $V$  be a volume in  $\mathbb{R}^3$ ,  $S$  a surface with a boundary, and  $\partial$  a boundary operator. Now, The Maxwell's equations can be written in an integral form:

$$\oint_{\partial S} \vec{E} \cdot d\vec{l} = - \int_S \frac{\partial \vec{B}}{\partial t} \cdot d\vec{A} \quad (2.9)$$

$$\oint_{\partial S} \vec{H} \cdot d\vec{l} = \int_S \left( \vec{J}_f + \frac{\partial \vec{D}}{\partial t} \right) \cdot d\vec{A} \quad (2.10)$$

$$\int_V \vec{B} \cdot d\vec{A} = 0 \quad (2.11)$$

$$\int_V \vec{D} \cdot d\vec{A} = \int_V \rho_f dV. \quad (2.12)$$

The integral form is more general, because it allows also discontinuities of the electromagnetic field, which exist e.g. on a boundary of two media. In a microscopic<sup>3</sup> form the Maxwell's equations read as:

$$\nabla \times \vec{E} = - \frac{\partial \vec{B}}{\partial t} \quad (2.13)$$

---

<sup>3</sup> The Maxwell's equations in microscopic scale include charges and currents at the atomic level and are considered as Maxwell's equations in a vacuum.



$$\nabla \times \vec{B} = \mu_0 \vec{J} + \mu_0 \epsilon_0 \frac{\partial \vec{E}}{\partial t} \quad (2.14)$$

$$\nabla \cdot \vec{B} = 0 \quad (2.15)$$

$$\nabla \cdot \vec{E} = \frac{\rho}{\epsilon_0}, \quad (2.16)$$

where  $\vec{J}$  is the total electric current density and  $\rho$  the total electric charge density, including both, free and bounded current and charge densities. Additionally,  $\epsilon_0$  is the electric permittivity of a vacuum, and  $\mu_0$  the magnetic permeability of a vacuum. The same equations in an integral form read as:

$$\oint_{\partial s} \vec{E} \cdot d\vec{l} = - \int_s \frac{\partial \vec{B}}{\partial t} \cdot d\vec{A} \quad (2.17)$$

$$\oint_{\partial s} \vec{B} \cdot d\vec{l} = \int_s \left( \mu_0 \vec{J} + \mu_0 \epsilon_0 \frac{\partial \vec{E}}{\partial t} \right) \cdot d\vec{A} \quad (2.18)$$

$$\int_V \vec{B} \cdot d\vec{A} = 0 \quad (2.19)$$

$$\int_V \vec{E} \cdot d\vec{A} = \int_V \frac{\rho}{\epsilon_0} dV. \quad (2.20)$$

The total current and charge densities are defined as

$$\rho = \rho_f - \nabla \cdot \vec{P} \quad (2.21)$$

$$\vec{J} = \vec{J}_f + \nabla \times \vec{M} + \frac{\partial \vec{P}}{\partial t}, \quad (2.22)$$

where the vector fields  $\vec{M}$  and  $\vec{P}$  are the magnetization field and the polarization field of the medium, respectively. The magnetization field  $\vec{M}$  is the density of magnetic dipole moments in the medium, and the polarization field  $\vec{P}$  the density of electric dipole moments in the medium.

---

## 2.2 Constitutive Relations

---

In order to join the electromagnetic field quantities with each other, constitutive relations are needed. The constitutive relations for electrodynamics in the frequency domain, in the absence of permanent polarization, read as

$$\vec{D}(\omega) = \varepsilon_0 \vec{E} + \vec{P} = \varepsilon(\vec{r}, \omega, \vec{E}) \vec{E}(\omega) \quad (2.23)$$

$$\vec{B}(\omega) = \mu_0 (\vec{H} + \vec{M}) = \mu(\vec{r}, \omega, \vec{H}) \vec{H}(\omega) \quad (2.24)$$

$$\vec{J}(\omega) = \sigma(\vec{r}, \omega, \vec{E}) \vec{E}(\omega), \quad (2.25)$$

where  $\varepsilon(\vec{r}, \omega, \vec{E})$ ,  $\mu(\vec{r}, \omega, \vec{H})$  and  $\sigma(\vec{r}, \omega, \vec{E})$  are the electrical permittivity, permeability and conductivity of the medium, respectively. These quantities are later referred to as material parameters. In general, the material parameters are tensors of second rank, but for isotropic medium, they are nonlinear scalars. Yet, permeability and permittivity are defined as

$$\varepsilon(\vec{r}, \omega, \vec{E}) = [1 + \chi_e(\vec{r}, \omega, \vec{E})] \varepsilon_0 = \varepsilon_r(\vec{r}, \omega, \vec{E}) \varepsilon_0 \quad (2.26)$$

$$\mu(\vec{r}, \omega, \vec{H}) = [1 + \chi_m(\vec{r}, \omega, \vec{H})] \mu_0 = \mu_r(\vec{r}, \omega, \vec{H}) \mu_0, \quad (2.27)$$

where  $\chi_e(\vec{r}, \omega, \vec{E})$ ,  $\chi_m(\vec{r}, \omega, \vec{H})$ ,  $\varepsilon_r(\vec{r}, \omega, \vec{E})$  and  $\mu_r(\vec{r}, \omega, \vec{H})$  are electric susceptibility, magnetic susceptibility, relative permeability and relative permittivity, respectively. The quantities  $\varepsilon_0$  and  $\mu_0$  are the permittivity and the permeability of a vacuum. Additionally, the magnetization field  $\vec{M}$  and the polarization field  $\vec{P}$  are defined as

$$\vec{M}(\omega) = \chi_m(\vec{r}, \omega, \vec{H}) \vec{H}(\omega) \quad (2.28)$$

$$\vec{P}(\omega) = \varepsilon_0 \chi_e(\vec{r}, \omega, \vec{E}) \vec{E}(\omega). \quad (2.29)$$

If the magnetic susceptibility  $\chi_m(\vec{r}, \omega, \vec{H})$  of the medium is zero, the medium is considered as non-magnetic. Consequently the relation between the magnetic flux density  $\vec{B}$  and magnetic field  $\vec{H}$  is linear. Respectively, if the electric susceptibility  $\chi_e(\vec{r}, \omega, \vec{E})$  is zero, the medium is considered as dielectric, and the relation between the displacement field  $\vec{D}$  and the electric field  $\vec{E}$  is linear. If the conductivity  $\sigma(\vec{r}, \omega, \vec{E})$  is nonzero, the medium is considered as conductor.

The abovementioned constitutive relations are defined in the frequency domain. The time domain formulations for the constitutive relations (2.23), (2.24), and (2.25) read as

$$\vec{D}(t) = \varepsilon(\vec{r}, t, \vec{E}) * \vec{E}(t) = \int_{-\infty}^{\infty} \varepsilon(\vec{r}, t - \tau, \vec{E}) \vec{E}(t) d\tau \quad (2.30)$$

$$\vec{B}(t) = \mu(\vec{r}, t, \vec{H}) * \vec{H}(t) = \int_{-\infty}^{\infty} \mu(\vec{r}, t - \tau, \vec{H}) \vec{H}(t) d\tau \quad (2.31)$$

$$\vec{J}(t) = \sigma(\vec{r}, t, \vec{E}) * \vec{E}(t) = \int_{-\infty}^{\infty} \sigma(\vec{r}, t - \tau, \vec{E}) \vec{E}(t) d\tau, \quad (2.32)$$

where  $*$  is the convolution operator. Similarly, the time domain formulations for the magnetization field  $\vec{M}$  (2.28) and the polarization field  $\vec{P}$  (2.29) read in the time domain as

$$\vec{M}(t) = \chi_m(\vec{r}, t, \vec{H}) * \vec{H}(t) = \int_{-\infty}^{\infty} \chi_m(\vec{r}, t - \tau, \vec{H}) \vec{H}(t) d\tau \quad (2.33)$$

$$\vec{P}(t) = \varepsilon_0 \chi_e(\vec{r}, t, \vec{E}) * \vec{E}(t) = \varepsilon_0 \int_{-\infty}^{\infty} \chi_e(\vec{r}, t - \tau, \vec{E}) \vec{E}(t) d\tau. \quad (2.34)$$

In this thesis, the material parameters are assumed to be linear and homogeneous, and therefore the dependencies on electric and magnetic fields,  $\vec{E}$  and  $\vec{H}$ , respectively, as well as on location  $\vec{r}$ , can be dropped out. However, the material parameters depend on angular frequency  $\omega$  and time  $t$  within this thesis. For the sake of clarity, also these dependencies are dropped out.

---

### 2.3 Boundary Conditions

---

The behaviour of the electromagnetic wave at the interface of two media can be deduced from the Maxwell's equations. In this section, the boundary conditions for the magnetic flux density and the electric field are derived in a detailed way,

the derivation of the boundary conditions for the displacement field and the magnetic field follow these derivations.

---

### 2.3.1 Magnetic Flux Density

---

Let us assume a flat, pillbox-shaped cylinder, placed on the interface such that the bottom and the top of it are parallel to the interface, see Figure 2.1.

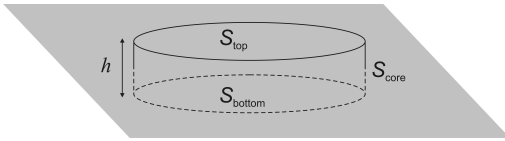


Figure 2.1: A pillbox-shaped cylinder illustrating the derivation of the boundary condition for the magnetic flux density and the displacement field [80].

The integrand of Gauss' law (2.19) can be divided into three parts, corresponding to the top, the bottom and the core of the cylinder:

$$\oint_S \vec{B} \cdot d\vec{A} = \int_{S_{\text{top}}} \vec{B} \cdot d\vec{A}_{\text{top}} + \int_{S_{\text{bottom}}} \vec{B} \cdot d\vec{A}_{\text{bottom}} + \int_{S_{\text{core}}} \vec{B} \cdot d\vec{A}_{\text{core}}. \quad (2.35)$$

If both media are nonmagnetic ( $\chi_m = 0$ , see Section 2.2), letting the height  $h$  of the cylinder approach zero, the integral over the core of the cylinder approaches zero. As the height of the cylinder is infinitesimal, the normal vectors of the bottom and the top are of equal magnitude, but have different signs. Let us denote and  $d\vec{A} = d\vec{A}_{\text{top}} = -d\vec{A}_{\text{bottom}}$ , and eventually Equation (2.35) can be rewritten as:

$$\int_{S_{\text{top}}} \vec{B} \cdot d\vec{A} = \int_{S_{\text{bottom}}} \vec{B} \cdot d\vec{A}, \quad (2.36)$$

or equivalently:

$$\vec{n} \cdot (\vec{B}_{\text{top}} - \vec{B}_{\text{bottom}}) = 0, \quad (2.37)$$

where  $\vec{n}$  is the outward pointing normal vector of the top of the cylinder. In words, the normal component of the magnetic field density is continuous over the interface of two media, when the media are nonmagnetic.

---

### 2.3.2 Displacement Field

---

Let us apply the same pillbox-approach as with magnetic flux density in Equation (2.35) to the displacement field (2.20):

$$\oint_S \vec{D} \cdot d\vec{A} = \int_{S_{\text{top}}} \vec{D} \cdot d\vec{A}_{\text{top}} + \int_{S_{\text{bottom}}} \vec{D} \cdot d\vec{A}_{\text{bottom}} + \int_{S_{\text{core}}} \vec{D} \cdot d\vec{A}_{\text{core}} = \int_V \rho_f dV. \quad (2.38)$$

After shrinking the cylinder on the same manner as with the magnetic flux density, we get a boundary condition for the displacement field:

$$\int_{S_{\text{top}}} \vec{D} \cdot d\vec{A} - \int_{S_{\text{bottom}}} \vec{D} \cdot d\vec{A} = \sigma_s, \quad (2.39)$$

or equivalently:

$$\vec{n} \cdot (\vec{D}_{\text{top}} - \vec{D}_{\text{bottom}}) = \sigma_s, \quad (2.40)$$

where the integral of the free charge density  $\rho_f$  over the infinitesimal volume has reduced into the surface charge density  $\sigma_s$ . Therefore, the normal component of the displacement field is discontinuous over the interface.

---

### 2.3.3 Electric Field

---

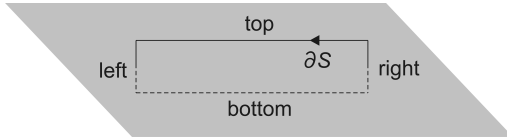


Figure 2.2: The path illustrating the derivation of the boundary condition for electric and magnetic fields [80].

To derive the boundary condition for the electric field, we place a rectangular path around the interface as shown in Figure 2.2. The integrand of the Faraday's law (2.17) can be divided into four parts, corresponding to the four edges of the path:

$$\oint_{\partial S} \vec{E} \cdot d\vec{l} = \int_{\text{left}} \vec{E} \cdot d\vec{l}_{\text{left}} + \int_{\text{top}} \vec{E} \cdot d\vec{l}_{\text{top}} + \int_{\text{right}} \vec{E} \cdot d\vec{l}_{\text{right}} + \int_{\text{bottom}} \vec{E} \cdot d\vec{l}_{\text{bottom}} = - \int_S \frac{\partial \vec{B}}{\partial t} \cdot d\vec{A}. \quad (2.41)$$

Again, we shrink the path such that the lengths of the left and right edges approach zero, and we get:

$$\int_{\text{top}} \vec{E} \cdot d\vec{l}_{\text{top}} + \int_{\text{bottom}} \vec{E} \cdot d\vec{l}_{\text{bottom}} = - \int_S \frac{\partial \vec{B}}{\partial t} \cdot d\vec{A}. \quad (2.42)$$

As the lengths of the left and right edges are infinitesimal, we can write  $\vec{dl} = d\vec{l}_{\text{top}} = -d\vec{l}_{\text{bottom}}$ . Furthermore, the area of the surface  $S$  surrounded by the path, approaches zero, and consequently also the integral of the magnetic field density over the surface  $S$  vanishes. Eventually, we can write the boundary condition for the electric field:

$$\int_{\text{bottom}} \vec{E} \cdot d\vec{l} = \int_{\text{top}} \vec{E} \cdot d\vec{l}, \quad (2.43)$$

or equivalently

$$\vec{n} \times (\vec{E}_{\text{top}} - \vec{E}_{\text{bottom}}) = 0. \quad (2.44)$$

In words, the tangential component of the electric field is continuous over the interface.

---

### 2.3.4 Magnetic Field

---

Let us use the same approach as for the electric field in Equation (2.41). The Ampère's law (2.18) with the integrand divided into four parts, reads as:

$$\begin{aligned}
\oint_{\partial S} \vec{H} \cdot d\vec{l} &= \int_{\text{left}} \vec{H} \cdot d\vec{l}_{\text{left}} + \int_{\text{top}} \vec{H} \cdot d\vec{l}_{\text{top}} + \int_{\text{right}} \vec{H} \cdot d\vec{l}_{\text{right}} \\
&+ \int_{\text{bottom}} \vec{H} \cdot d\vec{l}_{\text{bottom}} = - \int_S \frac{\partial}{\partial t} \left( \vec{J}_f + \frac{\partial \vec{D}}{\partial t} \right) \cdot d\vec{A}.
\end{aligned} \tag{2.45}$$

Shrinking the loop makes the integral of the displacement field to vanish, and reduces the integral of the current density into the surface current density  $j_s$ :

$$\int_{\text{top}} \vec{H} \cdot d\vec{l}_{\text{top}} + \int_{\text{bottom}} \vec{H} \cdot d\vec{l}_{\text{bottom}} = -j_s, \tag{2.46}$$

or equivalently:

$$\vec{n} \times (\vec{H}_{\text{top}} - \vec{H}_{\text{bottom}}) = j_s. \tag{2.47}$$

In words, the tangential magnetic field is discontinuous over the interface.

---

## 2.4 Electromagnetic Wave Equation

---

The electromagnetic wave equation is a second order partial differential equation, which describes the propagation of the electromagnetic wave in a vacuum or in a medium. The equation can be derived from the Maxwell's equations by taking the curl of the both sides of the Faraday's law (2.13), applying the Ampère's law (2.14) and the constitutive relation (2.25):

$$\nabla \times \nabla \times \vec{E} + \sigma \mu \frac{\partial \vec{E}}{\partial t} + \epsilon \mu \frac{\partial^2 \vec{E}}{\partial t^2} = 0. \tag{2.48}$$

The wave equation for the magnetic field  $\vec{H}$  can be derived correspondingly:

$$\nabla \times \nabla \times \vec{H} + \sigma \mu \frac{\partial \vec{H}}{\partial t} + \epsilon \mu \frac{\partial^2 \vec{H}}{\partial t^2} = 0. \tag{2.49}$$

Useful form of the electromagnetic wave equation is so called time harmonic wave equation. When electromagnetic field variation with respect to time is

sinusoidal, the time derivative  $\partial/\partial t$  can be replaced with the factor  $j\omega$ , where  $\omega$  is the angular frequency of the wave, and Equation (2.48) takes the form

$$\nabla \times \nabla \times \vec{E} + j\omega\sigma\mu\vec{E} - \epsilon\mu\omega^2\vec{E} = 0, \quad (2.50)$$

or - by applying vector identity  $\nabla \times (\nabla \times \vec{A}) = \nabla(\nabla \cdot \vec{A}) - \nabla^2\vec{A}$  and Gauss' law for electric fields (2.4) - equivalently as

$$\nabla^2\vec{E} - k^2\vec{E} = 0, \quad (2.51)$$

where

$$k = \sqrt{j\omega\sigma\mu - \epsilon\mu\omega^2} \quad (2.52)$$

is the wave number. The wave number is the magnitude of the wave vector  $\vec{k}$ . The real part of the wave number describes the propagation of the wave in the medium. This propagation constant is denoted with  $\beta$ . The imaginary part describes the attenuation of the wave. It is called attenuation constant and denoted with  $\alpha$ . Additionally, the direction of the wave vector describes the direction of the propagation of the wave. The simplest, and very useful, though strictly speaking unphysical, solution for the time-harmonic wave equation (2.5.2) is monochromatic plane wave <sup>1</sup>:

$$\vec{E}(\vec{r}, t) = \text{Re} \{ \vec{E}_0(\vec{r}) e^{j(\omega t - \vec{k} \cdot \vec{r})} \}, \quad (2.53)$$

where  $\vec{E}_0$  is the complex amplitude of the wave, and  $\vec{r}$  the position vector.

---

## 2.5 Electromagnetic Wave at Interface

---

The behaviour of the electromagnetic wave on the interface of two media is of high importance in this thesis. Later, in Chapter 4, the approximative boundary conditions for the electromagnetic wave are derived, and in this section the theoretical background for the approximations is given.

First, in Section 2.5.1, the behaviour of the electromagnetic wave on the interface of two dielectrics is explained. This case is commonly known as Snell's law, and it

---

<sup>1</sup> Only a wave at infinite distance of the source would be a true plane wave. However, almost any physical wave can be locally approximated as a plane wave.



is significantly simpler than the following case: Behaviour of the electromagnetic wave on the interface of a dielectric and a conductor. The latter case is elaborated in Section 2.5.2.

---

### 2.5.1 Dielectric - Dielectric

---

Let us assume an electromagnetic monochromatic plane wave (2.53) incident to the interface, see Figure 2.3. The incident, reflected, and transmitted waves are given respectively by <sup>1</sup>:

$$\vec{E}_1 = \vec{E}_{10}(\vec{r})e^{j(\vec{k}_1 \cdot \vec{r} - \omega t)} \quad (2.54)$$

$$\vec{E}_{1'} = \vec{E}_{10'}(\vec{r})e^{j(\vec{k}_{1'} \cdot \vec{r} - \omega t)} \quad (2.55)$$

$$\vec{E}_2 = \vec{E}_{20}(\vec{r})e^{j(\vec{k}_2 \cdot \vec{r} - \omega t)}, \quad (2.56)$$

where

$$\vec{k}_1 = k_1 \vec{n}_1 \quad (2.57)$$

$$\vec{k}_{1'} = k_{1'} \vec{n}_{1'} \quad (2.58)$$

$$\vec{k}_2 = k_2 \vec{n}_2, \quad (2.59)$$

are the corresponding wave vectors.

On the interface the incident wave must match to the reflected and transmitted wave. Consequently, the exponent of Equation (2.54) needs to be equal to the exponents of Equations (2.55) and (2.56):

$$\vec{k}_1 \cdot \vec{r}_0 - \omega t = \vec{k}_{1'} \cdot \vec{r}_0 - \omega t = \vec{k}_2 \cdot \vec{r}_0 - \omega t. \quad (2.60)$$

Obviously the frequencies of the waves are equal. Additionally, the phases of the waves need to match on the boundary:

$$\vec{k}_1 \cdot \vec{r}_0 = \vec{k}_{1'} \cdot \vec{r}_0 = \vec{k}_2 \cdot \vec{r}_0. \quad (2.61)$$

---

<sup>1</sup> The physical wave is the real part of the wave presented here, but  $\text{Re}\{\}$  is dropped out for convenience. This is also conventional notation of the electromagnetic wave.

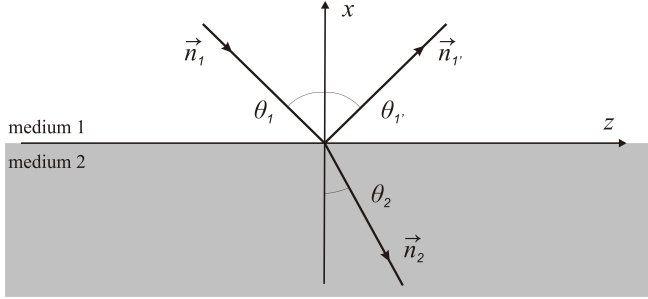


Figure 2.3.: Reflection and refraction of an electromagnetic wave on an interface of two media.

Applying vector calculus identities, and noting that  $\vec{r}_0$  and  $\vec{n}$  are perpendicular at the interface, (2.61) can be written as

$$\vec{n} \times \vec{k}_1 = \vec{n} \times \vec{k}_2 = \vec{n} \times \vec{k}_{1'}. \quad (2.62)$$

As  $|\vec{n} \times \vec{k}_1| = k_1 \sin \theta_1$ , and respectively for reflected and transmitted waves, we can deduce that

$$k_1 \sin \theta_1 = k_{1'} \sin \theta_{1'}, \quad (2.63)$$

$$k_1 \sin \theta_1 = k_2 \sin \theta_2. \quad (2.64)$$

Since incident and reflected waves are propagating in the same medium, the wave numbers  $k_1$  and  $k_{1'}$  have to be equal, as well as the angles of incidence and reflection. The equation for incident and refracted waves (2.64) is known as Snell's law.

---

## 2.5.2 Dielectric - Conductor

---

On the interface of a conductive medium, Snell's law leads into a complex refraction angle  $\theta_2$ . As an interface of a conductor is of great importance in this thesis, the physical meaning of the complex angle is analyzed in details. This analysis is taken from [91]. Let us assume again a plane wave incident to an interface as in Figure 2.3. In this particular case, the medium (1) is assumed to be a dielectric,

and medium (2) a conductor. Therefore the squares of the wave numbers  $k_1$  and  $k_2$  (2.52) for the media are given as:

$$k_1^2 = \omega^2 \epsilon_1 \mu_1 \quad (2.65)$$

$$k_2^2 = \omega^2 \epsilon_2 \mu_2 + j \omega \sigma \mu_2. \quad (2.66)$$

Let us divide the wave numbers into real and imaginary parts:

$$k_1 = \alpha_1 \quad (2.67)$$

$$k_2 = \alpha_2 + j\beta_2. \quad (2.68)$$

The angle of refraction is defined by Snell's law (2.64) and can be written as

$$\sin \theta_2 = \frac{k_1}{k_2} \sin \theta_1 = \frac{\alpha_1}{\alpha_2 + j\beta_2} \sin \theta_1 = (a - jb) \sin \theta_1, \quad (2.69)$$

and furthermore

$$\begin{aligned} \alpha_1 \sin \theta_1 &= (a - jb)(\alpha_2 + j\beta_2) \sin \theta_1 \\ &= (a\alpha_2 + b\beta_2) \sin \theta_1 + j(a\beta_2 - b\alpha_2) \sin \theta_1. \end{aligned} \quad (2.70)$$

As  $\alpha_1$ , as well as  $\sin \theta_1$ , are both real by the definitions (2.67) and (2.68), we can deduce that

$$a\alpha_2 + b\beta_2 = \alpha_1 \quad (2.71)$$

$$a\beta_2 - b\alpha_2 = 0. \quad (2.72)$$

The complex cosine can be written as

$$\begin{aligned} \cos \theta_2 &= \sqrt{1 - \sin^2 \theta_2} \\ &= \sqrt{1 - (a^2 - b^2 - 2jab) \sin^2 \theta_1} \\ &= r e^{j\gamma} = r \cos \gamma + jr \sin \gamma. \end{aligned} \quad (2.73)$$

Let us analyze the phase  $\vec{k}_2 \cdot \vec{r}$  of the wave in medium (2):

$$\vec{k}_2 \cdot \vec{r} = k_2 \vec{n}_2 \cdot \vec{r} = (\alpha_2 + j\beta_2)(-x \cos \theta_2 + z \sin \theta_2). \quad (2.74)$$

Recalling the relations for  $\sin \theta_2$  (2.69) and  $\cos \theta_2$  (2.73), the phase can be written as

$$\begin{aligned} k_2 \vec{n}_2 \cdot \vec{r} = & xr(\alpha_2 \cos \gamma - \beta \sin \gamma) - jxr(\beta_2 \cos \gamma - \alpha_2 \sin \gamma) \\ & + z(a\alpha_2 + b\beta_2) \sin \theta_1 + jz(a\beta_2 - b\alpha_2) \sin \theta_1. \end{aligned} \quad (2.75)$$

Applying the relations (2.71) and (2.72), the phase can be written as:

$$\vec{k}_2 \cdot \vec{r} = xr(\alpha_2 \cos \gamma - \beta \sin \gamma) - jxr(\beta_2 \cos \gamma - \alpha_2 \sin \gamma) + z\alpha_1 \sin \theta_1. \quad (2.76)$$

Denoting

$$r(\beta_2 \cos \gamma - \alpha_2 \sin \gamma) = p \quad (2.77)$$

$$r(\alpha_2 \cos \gamma - \beta \sin \gamma) = q, \quad (2.78)$$

we get

$$k_2 \vec{n}_2 \cdot \vec{r} = -xq - jxp + z\alpha_1 \sin \theta_1. \quad (2.79)$$

The refracted wave within the medium (2) (2.56) can now be written as

$$\vec{E}_2 = \vec{E}_{20} e^{px} e^{j(-qx + \alpha_1 z \sin \theta_1 - \omega t)}. \quad (2.80)$$

Clearly the surfaces of constant amplitude are the planes

$$px = \text{constant}, \quad (2.81)$$

which means that the planes of the constant amplitude are parallel to the interface. The planes of constant phase are the planes

$$-qx + \alpha_1 z \sin \theta_1 = \text{constant}. \quad (2.82)$$

Therefore, the wave in medium (2) is an inhomogeneous plane wave, and the direction of propagation is determined by the normal to the planes of constant phase. The angle of propagation  $\Psi$  of this wave is defined as

$$-x \cos \psi + z \sin \psi = \text{constant}. \quad (2.83)$$

After normalizing Equation (2.83) we obtain

$$\cos \psi = \frac{q}{\sqrt{q^2 + \alpha_1^2 \sin^2 \theta_1}} \quad (2.84)$$

$$\sin \psi = \frac{\alpha_1 \sin \theta_1}{\sqrt{q^2 + \alpha_1^2 \sin^2 \theta_1}}. \quad (2.85)$$

Next, we assume that the medium (2) is a good conductor. This assumption can be formulated as follows: Let us first rewrite the wave equation as

$$\nabla^2 \vec{E} - j\omega\mu(\sigma + \epsilon\omega)\vec{E} = 0. \quad (2.86)$$

If we assume that the conduction current  $\vec{J} = \sigma\vec{E}$  is much greater than the displacement current  $\partial\vec{D}/\partial t$ , or in other words,  $\sigma$  in Equation (2.86) is much greater than  $\omega\epsilon$ , we can neglect the latter and the equation reads as

$$\nabla^2 \vec{E} - j\omega\mu\sigma\vec{E} = 0. \quad (2.87)$$

Now the square of the wave number  $k$  can be written as

$$k^2 \approx j\omega\mu\sigma, \quad (2.88)$$

and consequently the real and imaginary parts of the wave number  $k_2$  are equal:

$$\alpha_2 = \beta_2 = \sqrt{\frac{\omega\mu_2\sigma}{2}}. \quad (2.89)$$

Using this assumption, we can deduce (see details in e.g. [91], [80]) following equation for  $q$  (2.78):

$$q \approx \sqrt{\frac{\omega\mu_1\sigma}{2}}, \quad (2.90)$$

and furthermore for the sine of the refracted wave (2.85)

$$\sin \Psi = \sqrt{\frac{2\omega\mu_1\epsilon_1}{\mu_2\sigma}} \sin \theta_1. \quad (2.91)$$

Equation (2.91) shows, that as the conductivity increases or the frequency decreases, the planes of the constant phases align themselves with the plane of the constant amplitude, and the wave propagates normal to the surface within the conductor. This effect can be also seen in Figure 2.4, where the ratio  $\sin \Psi / \sin \theta_1$  is plotted with respect to conductivity at a few frequencies.

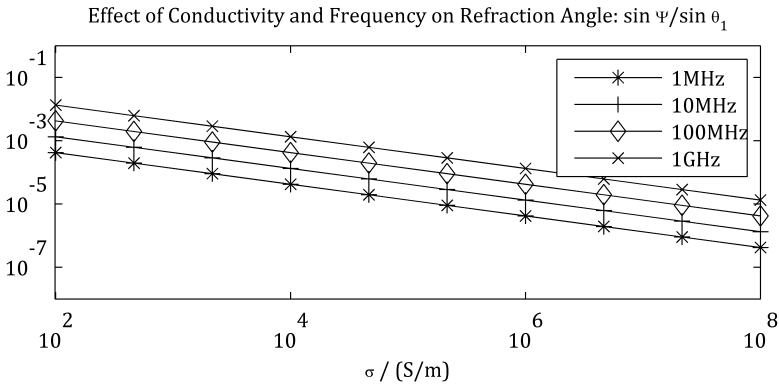


Figure 2.4.: The ratio  $\sin \Psi / \sin \theta_1$  with respect to conductivity  $\sigma$ . The curves are plotted at four frequencies between 1MHz and 1GHz. The curves show that when the conductivity increases, the ratio is really small and consequently the wave in the conductor propagates normal to the interface. Already with conductivity  $\sigma = 100\text{S/m}$  and frequency 1GHz, the ratio is 1%, and the wave can be considered propagating normal to the interface.

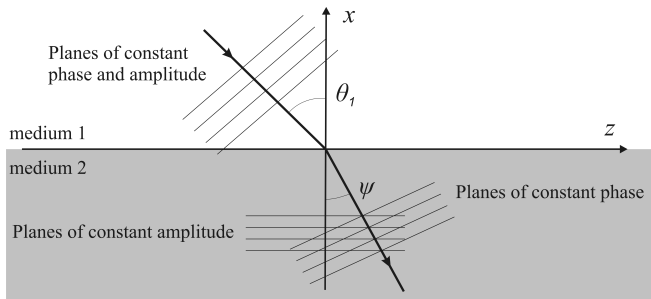


Figure 2.5.: Refraction in a conductive medium. According to [91], page 502.

---

## 2.6 Conservation Laws

---

Electromagnetic conservation laws state that certain properties of an isolated physical system are conserved when the system develops. In this section, two important conservation laws in electrodynamics are introduced: In Poynting's theorem the conserved property of a system is energy, and in Current Continuity law, the conserved property is electric charge.

---

### 2.6.1 Poynting's Theorem

---

In this chapter, the law for conservation of energy for electromagnetic field is derived. Let us start by taking the scalar product of  $\vec{E}$  with the Faraday's law (2.1), and of  $\vec{H}$  with Equation (2.2). Subtracting these equations from each other, we get

$$\vec{H} \cdot \nabla \times \vec{E} - \vec{E} \cdot \nabla \times \vec{H} = -\vec{H} \cdot \frac{\partial \vec{B}}{\partial t} - \vec{E} \cdot \frac{\partial \vec{D}}{\partial t} - \vec{E} \cdot \vec{J}_f. \quad (2.92)$$

Applying vector identity  $\nabla \cdot (\vec{A} \times \vec{B}) = \vec{B} \cdot \nabla \times \vec{A} - \vec{A} \cdot \nabla \times \vec{B}$ , we obtain

$$\nabla \cdot (\vec{E} \times \vec{H}) = -\vec{H} \cdot \frac{\partial \vec{B}}{\partial t} - \vec{E} \cdot \frac{\partial \vec{D}}{\partial t} - \vec{E} \cdot \vec{J}_f. \quad (2.93)$$

Let us denote the vector product  $\vec{E} \times \vec{H}$  as  $\vec{S}$ , which is known as the Poynting vector, and integrate Equation (2.93) over a volume  $V$ :

$$\int_V \nabla \cdot \vec{S} dV = - \int_V \left( \vec{H} \cdot \frac{\partial \vec{B}}{\partial t} + \vec{E} \cdot \frac{\partial \vec{D}}{\partial t} \right) dV - \int_V \vec{E} \cdot \vec{J}_f dV. \quad (2.94)$$

Applying the divergence theorem and reorganizing the terms, we obtain so called Poynting's theorem:

$$- \int_V \vec{E} \cdot \vec{J}_f dV = - \int_V \left( \vec{H} \cdot \frac{\partial \vec{B}}{\partial t} + \vec{E} \cdot \frac{\partial \vec{D}}{\partial t} \right) dV + \oint_S \vec{S} \cdot \vec{dA}. \quad (2.95)$$

If we assume that  $\vec{H}$  and  $\vec{B}$ , as well as  $\vec{E}$  and  $\vec{D}$ , depend on each other linearly, we can rewrite Equation (2.95) as

$$- \int_V \vec{E} \cdot \vec{J}_f dV = \frac{1}{2} \frac{\partial}{\partial t} \int_V (\vec{H} \cdot \vec{B} + \vec{E} \cdot \vec{D}) dV + \oint_S \vec{S} \cdot \vec{dA}. \quad (2.96)$$

or

$$\underbrace{- \int_V \vec{E} \cdot \vec{J}_f dV}_{(1)} = \underbrace{\int_V \frac{\partial W}{\partial t} dV}_{(2)} + \underbrace{\oint_S \vec{S} \cdot \vec{dA}}_{(3)}, \quad (2.97)$$

where  $W$  is the energy stored in the electromagnetic field in  $V$ . The terms in Poynting's theorem can be interpreted as follows:

- (1) The energy transformed from the electromagnetic form into another form, e.g. heat or mechanical energy
- (2) The rate of change of electromagnetic energy stored in the volume  $V$
- (3) The power flow into or out from the volume  $V$ .

---

## 2.6.2 Current Continuity

---

The electric current  $I$  entering an arbitrary volume  $V$  is given by the integral



---

$$I = - \int_V \vec{J} \cdot d\vec{A} = - \int_V \nabla \cdot \vec{J} dV. \quad (2.98)$$

At the same time, the electric current into the fixed volume  $V$  is defined as a rate of change of electric charge density in the volume:

$$I = - \int_V \frac{\partial \rho}{\partial t} dV. \quad (2.99)$$

Combining Equation (2.98) with Equation (2.99) gives:

$$\int_V \left( \frac{\partial \rho}{\partial t} + \nabla \cdot \vec{J} \right) dV = 0. \quad (2.100)$$

As the volume  $V$  is arbitrary, Equation (2.99) holds at each point and can be written as

$$\frac{\partial \rho}{\partial t} + \nabla \cdot \vec{J} = 0. \quad (2.101)$$

This is known as the current continuity law. The current continuity law states that the electric charge cannot be created or destroyed, i.e. the total electric charge is always conserved.

---

## 3 Discrete Electrodynamics

In the previous chapter, the essential theory of continuous electrodynamics was shortly introduced. In the chapters following this chapter, the methods for solving the electromagnetic problems with dispersive impedance boundary conditions numerically are proposed and verified. The aim of this chapter is to span the gap between the theory of electrodynamics, and the following chapters. Namely, this chapter introduces the methods to discretize the computational domain spatially and temporally.

---

### 3.1 Introduction

---

The analytical solution for the Maxwell's equations exist only for a few particular cases. In general, one has to resort to numerical methods to find the solution. Numerical methods for solving the Maxwell's equations are often referred to as discrete electrodynamics, due to the discretization of the variables, which is involved to numerical methods. Discretization means replacing the continuous variables, like space and time, with their discrete counterparts. Numerical methods that are widely used for solving the Maxwell's equations include e.g. FDTD, FIT, FEM, DG-FEM, Finite Volume Method (FVM) and Method of Moments (MoM).

Aforementioned methods can be, in general, used for solving the Maxwell's equations in the frequency or in the time domain. In the frequency domain, one solves the problem at a single frequency, and the implementation is rather straightforward. However, time domain methods are able to catch transient signals and solve for several frequencies at a single simulation run.

In this thesis the focus is on FEM, and especially DG-FEM, which can be understood as a special case of FEM. The rationale for this choice is that DG-FEM combines many of the advantages of the aforementioned numerical methods: DG-FEM is spatially accurate, and the time stepping scheme is explicit. In this chapter an overview DG-FEM is given, and applying the method for solving the Maxwell's equations is explained. Finally, an overview of discretizing the time using Leapfrog and Verlet integrations is given. As further reading on the topics of this chapter, the author recommends the books "The Finite Element Method in

---

Electromagnetics" by J.M Jin [54] and "Nodal Discontinuous Galerkin Methods" by J.S. Hesthaven and T. Warburton [48].

---

### 3.2 Finite Element Method

---

The Finite Element Method (FEM) is a numerical method for solving a Partial Differential Equation (PDE). FEM has its basis in solving structural and elasticity problems, which have inherited some terminology to FEM. To give an overview of solving a PDE with FEM, let us assume a PDE with an operator  $\mathbf{L}$  and a solution  $u(x)$ :

$$\mathbf{L}u(x) = 0, \quad x = x_1 \dots x_2, \quad (3.1)$$

where the interval  $x = x_1 \dots x_2$  is a one-dimensional domain  $\Omega$ .

As FEM is an approximative numerical method, the next step is to approximate the PDE. The approximative PDE with an approximative solution  $\tilde{u}(x)$  reads as

$$\mathbf{L}\tilde{u}(x) \approx 0, \quad x = x_1 \dots x_2. \quad (3.2)$$

The approximative solution  $\tilde{u}(x) \approx u(x)$  is defined as

$$\tilde{u}(x) = \sum_{j=1}^N u_j \varphi_j(x), \quad x = x_1 \dots x_2, \quad (3.3)$$

where  $u_j$  are the Degree of Freedom (DoF)s,  $N$  the number of degrees of freedom, and  $\varphi_j$  a set of the shape, or basis, functions.

To find the best approximation  $\tilde{u}(x)$  of the exact solution  $u(x)$ , we define a residual  $R$  as a difference of the exact (3.1) and the approximated (3.2) PDEs:

$$R = \mathbf{L}[\tilde{u}(x) - u(x)] = \mathbf{L}\tilde{u}(x). \quad (3.4)$$

Furthermore, we utilize the weighted residual method to find the approximative solution:

$$\int_{x_1}^{x_2} R \cdot w_i(x) = 0 \quad \forall i = 1, 2, \dots, N, \quad (3.5)$$

---

where  $w_i(x)$  are linearly independent weight, or test, functions. In this thesis, we use the Galerkin method, where the weight functions  $w_i(x)$  are equal to the basis functions  $\varphi_j(x)$ .

Further important steps in finding the approximative solution by means of FEM include discretization the domain  $\Omega$  into a finite element mesh, and choosing the basis functions. An overview of these steps is given in the following two subsections.

---

### 3.2.1 Mesh

---

In order to find a numerical solution for a PDE by means of FEM, the domain  $\Omega$  is divided into finite elements  $e$ .  $N_e$  elements together build a finite element mesh. For practical reasons, the element domains are usually of a simple geometrical form: Lines in one dimension, triangles or quadrilaterals in two dimensions, and tetrahedra or hexahedra in three dimensions. The mesh can be also called a computational domain.

Depending on the dimension of the mesh, an element includes nodes, edges, faces and volumes. The degrees of freedom can be associated with any of these. See an example of a three-dimensional hexahedral mesh element in Figure 3.1.

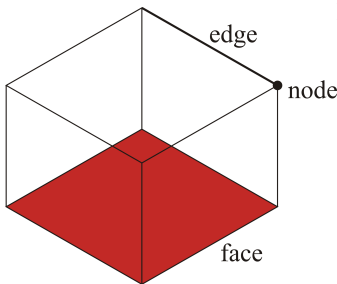


Figure 3.1: A hexahedral element of a three-dimensional finite element mesh. The node is the boundary of the edge, which is a boundary of the face, which is the boundary of the element.

The mesh is regular, when the elements are non-overlapping, the mesh covers the domain  $\Omega$ , and the intersection of two elements is either empty, a node, an edge, or a face.

---

### 3.2.2 Basis Functions

---

The choice of the basis functions  $\varphi_j$  in Equation (3.3) is arbitrary to a certain extent. However, some types of basis functions are more suitable to approximate certain physical quantities than the others. In this thesis we focus

solely on the Maxwell's equations in three dimensions, and therefore we use two kinds of basis functions:  $\mathbf{H}(\text{curl})$ -conformal higher order edge basis functions, and  $\mathbf{H}(\text{div})$ -conformal higher order face basis functions. The definitions of these basis functions are given in [101].

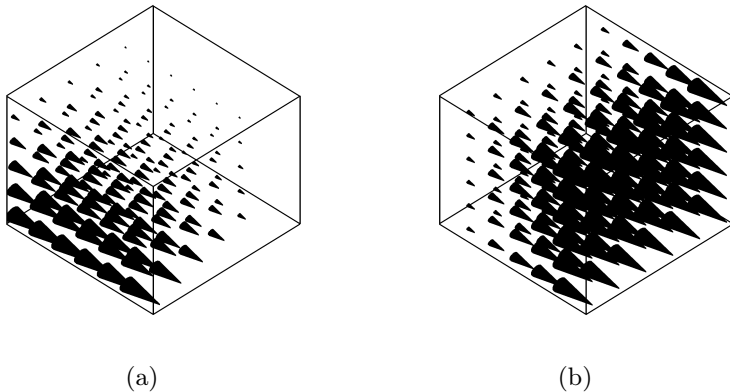


Figure 3.2.:  $\mathbf{H}(\text{curl})$ -conformal edge basis function (a), and  $\mathbf{H}(\text{div})$ -conformal face basis function. The polynomial order of both of the basis functions is zero, i.e. the basis function has a constant value over the edge (a) or the face (b).

To give an impression of these basis functions, the lowest order edge and face basis functions are schematically illustrated in Figures 3.2(a) and (b), respectively. The order refers to the polynomial order of the basis functions, while the lowest order is zero. This means that the basis functions have a constant value over the edge (edge basis function) or over the face (face basis function), as can be seen in Figures 3.2(a) and (b), respectively.

An important feature of these basis functions is, that they provide continuity over the interface: Edge basis functions tangential continuity, and face basis functions normal continuity. Let us recall the continuity conditions for the electromagnetic field in Sections 2.3.1-2.3.4. As stated, the magnetic flux density  $\vec{B}$  and the displacement field  $\vec{D}$  are normally continuous over the interface, while the electric field  $\vec{E}$  and the magnetic field  $\vec{H}$  are tangentially continuous over the interface. Therefore the natural selection is, to associate the magnetic flux density and the displacement field with the  $\mathbf{H}(\text{div})$ -conformal edge basis functions, and the electric field and the magnetic field with the  $\mathbf{H}(\text{curl})$ -conformal face basis functions.

Another important property of FEM basis functions is the global continuity. In FEM, the basis functions are continuous and have a compact support within the domain  $\Omega$ . These properties lead to a continuity of the approximate solution, and to a sparse FEM system matrix. However, the inverse of the FEM matrix is dense and that leads into inefficient time stepping scheme, since the matrix needs to be inverted at every time step. An approach to overcome this problem is not to require a global continuity of the basis functions, but to define the basis functions only within one element. This approach is called Discontinuous Galerkin Finite Element Method (DG-FEM). The differences between the basis functions for FEM and DG-FEM are schematically illustrated in Figures 3.3 (a) and (b), respectively.

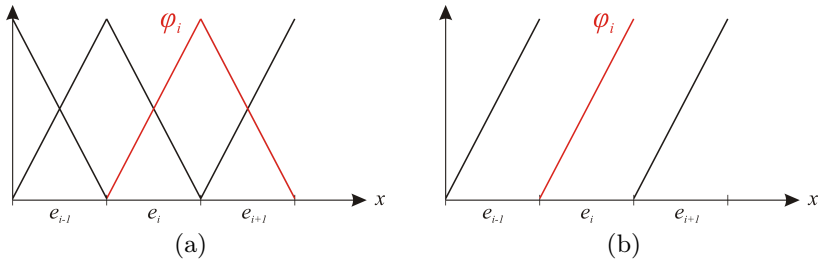


Figure 3.3.: A schematic illustration of an one-dimensional nodal basis function for FEM (a) and for DG-FEM (b). The FEM basis function has a compact support, i.e. it is defined in the element  $e_i$  and  $e_{i+1}$ . Conversely, the DG-FEM basis function is defined only in the element  $e_i$ , and there is no continuity on the element interfaces.

---

### 3.3 DG-FEM for Maxwell's Equations

---

Let us assume a three dimensional domain  $\Omega$  and recall the Maxwell's equations (2.1)-(2.4), as well as the constitutive equations (2.23)-(2.25). Additionally, let us assume a medium without current or charge densities for simplicity. The equations can be written as:

$$\begin{cases} \nabla \times \vec{E}(t, \vec{r}) + \frac{\partial}{\partial t} \mu \vec{H}(t, \vec{r}) = 0 & \text{in } \Omega \\ \nabla \times \vec{H}(t, \vec{r}) - \frac{\partial}{\partial t} \varepsilon \vec{E}(t, \vec{r}) = 0 & \text{in } \Omega. \end{cases} \quad (3.6)$$

These equations are now the exact PDEs (3.1). Let us approximate the electric field  $\vec{E}$  as an approximation  $\tilde{E}$ , and the magnetic field  $\vec{H}$  as  $\tilde{H}$ , as given in Equation (3.3):

$$\tilde{E}(t, \vec{r}) \approx \tilde{E}(t, \vec{r}) = \sum_{i=1}^{N_E} \sum_{p=1}^{\mathcal{P}} e^{ip}(t) \varphi_E^{ip}(\vec{r}) \quad (3.7)$$

$$\tilde{H}(t, \vec{r}) \approx \tilde{H}(t, \vec{r}) = \sum_{i=1}^{N_H} \sum_{p=1}^{\mathcal{P}} h^{ip}(t) \varphi_H^{ip}(\vec{r}), \quad (3.8)$$

where  $\varphi_E^{ip}(\vec{r})$  are  $\mathbf{H}(\text{curl})$ -conforming edge basis functions,  $\varphi_H^{ip}(\vec{r})$  are  $\mathbf{H}(\text{div})$ -conforming face basis functions,  $e^{ip}$  and  $h^{ip}$  the time-dependent degrees of freedom,  $N_E$  and  $N_H$  the corresponding numbers of degrees of freedom, and  $\mathcal{P}$  the polynomial order of the basis functions. The basis functions are defined such, that they are continuous within a element  $V_j$ , and vanish everywhere else. Let us drop out the temporal ( $t$ ) and spatial ( $\vec{r}$ ) dependencies for simplicity.

Following the Galerkin weighted residual method (3.5), the weak DG-FEM formulation reads as:

$$\int_{V_j} (\nabla \times \varphi_H^{jq}) \cdot \tilde{E} dV_j + \int_{\partial V_j} (\vec{n} \times \tilde{E}^*) \cdot \varphi_H^{jq} \vec{dA}_j + \int_{V_j} \frac{d}{dt} \mu_j \tilde{H} \cdot \varphi_H^{jq} dV_j = 0 \quad (3.9)$$

$$\int_{V_j} (\nabla \times \varphi_E^{jq}) \cdot \tilde{H} dV_j + \int_{\partial V_j} (\vec{n} \times \tilde{H}^*) \cdot \varphi_E^{jq} \vec{dA}_j - \int_{V_j} \frac{d}{dt} \varepsilon_j \tilde{E} \cdot \varphi_E^{jq} dV_j = 0, \quad (3.10)$$

$\forall j = 1 \dots N, \forall q = 1 \dots \mathcal{P}$ .  $V_j$  is the volume of the element domain,  $\vec{n}$  is the normal vector of the element interface, and the quantities  $\vec{n} \times \tilde{E}^*$  and  $\vec{n} \times \tilde{H}^*$  are known as numerical fluxes (see Equations (3.11) and (3.12) and the explanation later). Furthermore, the degrees of freedom depend only on the temporal variable, as well as basis functions only on the spatial variable. Therefore the time derivative and the degrees of freedom can be taken out from the integral. Additionally, we assume that material parameters do not depend on time.

Due to the discontinuity of the basis functions, the tangential electric and magnetic field approximations,  $\tilde{E}^*$  and  $\tilde{H}^*$ , are not uniquely defined at the element interfaces. Therefore, numerical fluxes [47] need to be introduced on the inter-

face. In this thesis, the central flux approach [10], [34] is utilized. The numerical flux for the electric field at the interface is defined as:

$$\vec{n} \times \tilde{E}^* = \frac{1}{2} \vec{n} \times (\tilde{E}^- + \tilde{E}^+), \quad (3.11)$$

where  $\tilde{E}^-$  is the approximative electric field (3.7) in the element  $j$ , and  $\tilde{E}^+$  in the neighboring element. The numerical flux is defined equivalently for the magnetic field:

$$\vec{n} \times \tilde{H}^* = \frac{1}{2} \vec{n} \times (\tilde{H}^- + \tilde{H}^+). \quad (3.12)$$

Finally we obtain the FEM Maxwell's equations in matrix form:

$$\begin{cases} \mathbf{C}_B \mathbf{e} + \mathbf{M}_\mu \frac{d}{dt} \mathbf{h} = 0 \\ \mathbf{C}_D \mathbf{h} - \mathbf{M}_\epsilon \frac{d}{dt} \mathbf{e} = 0, \end{cases} \quad (3.13)$$

where  $\mathbf{e}$  and  $\mathbf{h}$  are vectors including the electric and magnetic degrees of freedom, matrices  $\mathbf{C}_B$  and  $\mathbf{C}_D$  given elementwise as

$$C_B^{jq \ ip} = \delta_{ij} \int_{V_j} (\nabla \times \varphi_H^{jq}) \cdot \varphi_E^{ip} dV_j + \frac{1}{2} \int_{\partial V_j} (\vec{n} \times \varphi_E^{ip}) \cdot \varphi_H^{jq} d\vec{A}_j \quad (3.14)$$

$$C_D^{jq \ ip} = \delta_{ij} \int_{V_j} (\nabla \times \varphi_E^{jq}) \cdot \varphi_H^{ip} dV_j + \frac{1}{2} \int_{\partial V_j} (\vec{n} \times \varphi_H^{ip}) \cdot \varphi_E^{jq} d\vec{A}_j, \quad (3.15)$$

and matrices  $\mathbf{M}_\mu$  and  $\mathbf{M}_\epsilon$  elementwise as:

$$M_\mu^{jq \ ip} = \delta_{ij} \int_{\Omega_j} \mu_j \varphi_H^{jq} \cdot \varphi_H^{ip} dV_j, \quad (3.16)$$

$$M_\epsilon^{jq \ ip} = \delta_{ij} \int_{\Omega_j} \epsilon_j \varphi_E^{jq} \cdot \varphi_E^{ip} dV_j. \quad (3.17)$$



---

Regardless of many advantages of the DG-FEM method, there is one important drawback in the method. Namely, due to the discontinuity of the basis functions, DG-FEM suffers from so called spurious modes [92]. This problem can be avoided by using penalization methods, proposed in e.g. [46] and [33]. In this thesis, the penalization method proposed by Gjonaj and Weiland in [33] is used to avoid the spurious modes at the frequencies of interest. Additionally, due to the compact support of the basis functions, the number of degrees of freedom is higher in DG-FEM, than in FEM.

---

### 3.4 Discretization of Time

---

Discretization of time means replacing the continuous temporal variable  $t$  with its discrete counterpart in an interval  $t = 0..T$ . The discrete time variable is defined only at certain time instances, and the difference between the instances is called time step, denoted as  $\Delta t$ . The interval  $t = 0..T$  in the discrete time domain is defined as  $t = 0, \Delta t, 2\Delta t, \dots, N\Delta t$ , where  $N$  is the number of time steps. In the discrete time domain, the integration of time is replaced with numerical integration schemes. The Maxwell's equations (2.1)-(2.4), as well as the DG-FEM discretized Maxwell's equations (3.13) are a Hamiltonian system [68], [58], [74]. Therefore, symplectic numerical integration schemes [84] can be utilized. In the following, a short overview of two symplectic integrators, the Leapfrog and the Verlet integrators are given.

---

#### 3.4.1 Leapfrog Integration

---

Let us recall the DG-FEM discretized Maxwell's equations (3.13):

$$\begin{cases} \mathbf{C}_B \mathbf{e} + \mathbf{M}_\mu \frac{d}{dt} \mathbf{h} = 0 \\ \mathbf{C}_D \mathbf{h} - \mathbf{M}_\epsilon \frac{d}{dt} \mathbf{e} = 0. \end{cases} \quad (3.18)$$

As a Hamiltonian system [58], the equations above can be solved by the Leapfrog method:

$$\begin{cases} \mathbf{C}_B \mathbf{e}^n + \mathbf{M}_\mu \frac{1}{\Delta t} (\mathbf{h}^{n+\frac{1}{2}} - \mathbf{h}^{n-\frac{1}{2}}) = 0 \\ \mathbf{C}_D \mathbf{h}^{n+\frac{1}{2}} - \mathbf{M}_\epsilon \frac{1}{\Delta t} (\mathbf{e}^{n+1} - \mathbf{e}^n) = 0, \end{cases} \quad (3.19)$$


---

where  $\mathbf{e}^n$  is the electric field at time instant  $n\Delta t$ , and respectively for the other time instants, as well as the magnetic field. Consequently, we obtain the following time stepping scheme for solving electric and magnetic fields:

$$\begin{cases} \mathbf{h}^{n+\frac{1}{2}} = \mathbf{h}^{n-\frac{1}{2}} - \Delta t \mathbf{M}_\mu^{-1} \mathbf{C}_B \mathbf{e}^n \\ \mathbf{e}^{n+1} = \mathbf{e}^n + \Delta t \mathbf{M}_\epsilon^{-1} \mathbf{C}_D \mathbf{h}^{n+\frac{1}{2}}. \end{cases} \quad (3.20)$$

The leapfrog method is the simplest symplectic integrator, and it is very cheap.

---

### 3.4.2 Verlet Integration

---

The Verlet integration is also a symplectic numerical integrating scheme [74], and unlike the Leapfrog method, it allows to solve for the field quantities at the same time instants [74]. The Verlet scheme reads for Maxwell's equations as:

$$\begin{cases} \mathbf{C}_B \mathbf{e}^n + \mathbf{M}_\mu \frac{1}{\Delta t/2} (\mathbf{h}^{n+\frac{1}{2}} - \mathbf{h}^{n-\frac{1}{2}}) = 0 \\ \mathbf{C}_D \mathbf{h}^{n+\frac{1}{2}} - \mathbf{M}_\epsilon \frac{1}{\Delta t} (\mathbf{e}^{n+1} - \mathbf{e}^n) = 0 \\ \mathbf{C}_B \mathbf{e}^{n+1} + \mathbf{M}_\mu \frac{1}{\Delta t/2} (\mathbf{h}^{n+\frac{3}{2}} - \mathbf{h}^{n+\frac{1}{2}}) = 0. \end{cases} \quad (3.21)$$

Consequently, we obtain the following time stepping scheme for solving electric and magnetic fields:

$$\begin{cases} \mathbf{h}^{n+\frac{1}{2}} = \mathbf{h}^{n-\frac{1}{2}} - 2\Delta t \mathbf{M}_\mu^{-1} \mathbf{C}_B \mathbf{e}^n \\ \mathbf{e}^{n+1} = \mathbf{e}^n + \Delta t \mathbf{M}_\epsilon^{-1} \mathbf{C}_D \mathbf{h}^{n+\frac{1}{2}} \\ \mathbf{h}^{n+\frac{3}{2}} = \mathbf{h}^{n+\frac{1}{2}} - 2\Delta t \mathbf{M}_\mu^{-1} \mathbf{C}_B \mathbf{e}^{n+1}. \end{cases} \quad (3.22)$$

In time domain simulations within this thesis (see Section 5), the Verlet-scheme is utilized due to its accuracy.

---

# 4 Dispersive Boundary Conditions in Frequency Domain

In the previous chapter, the inevitable step from continuous electrodynamics towards electromagnetic modeling was taken. This means, methods for discretizing the computational domain in space and time were introduced, in terms of well-known tools of computational electrodynamics, as DG-FEM, and Leapfrog and Verlet integration.

This chapter considers electromagnetic modeling itself, in the Frequency Domain (FD). It is divided into two main parts, while first introduces dispersive impedance boundary conditions SIBC, CSBC, and ITBC. The second part presents the implementations of the impedance boundary conditions to frequency domain DG-FEM, as well as a scheme for solving the nonlinear, complex Eigenvalue Problem (EVP), raising from the electromagnetic problem with dispersive impedance boundary conditions, iteratively as a linear EVP. The scheme has been published by the author in [98]. This iterative scheme allows for taking into account the dispersivity of the impedance boundary conditions into account, and solving for wideband electromagnetic problems in the frequency domain.

---

## 4.1 Introduction

---

Boundary conditions in electromagnetic modeling save significantly computational resources, and are therefore very important. Boundary conditions allow for excluding certain structures of the computational domain: Instead of modeling the structure itself, only the surface of the excluded structure is modeled. Although the computational resources are saved, the accuracy is preserved. Impedance boundary conditions are aimed to exclude conductive, lossy media from the computational domain. In this chapter selected impedance boundary conditions are introduced.

Conductivity of a medium is in general a function of frequency, i.e. the conductivity is a dispersive function. The dispersive nature of the conductivity needs to be taken into account when considering impedance boundary conditions, because they are utilized to replace conductive media. This requires a special treatment in the time domain (see Chapter 5), but is rather straightforward in the

frequency domain. Therefore an introduction to selected impedance boundary conditions, namely SIBC, CSBC and ITBC, is given in the frequency domain. The introduction covers the first part of this chapter, i.e. sections 4.2.1, 4.3, and 4.4.

The plot of the second part of this chapter (Sections 4.6 and 4.7) is to find a numerical solution for the source-free Maxwell's equations in the frequency domain in a computational domain  $\Omega$ :

$$\begin{cases} \nabla \times \vec{E} = -j\omega\vec{B} & \text{in } \Omega \\ \nabla \times \vec{H} = j\omega\vec{D} & \text{in } \Omega \\ \vec{n} \times \vec{n} \times \vec{E} = f(\omega)(\vec{n} \times \vec{H}) & \text{on } \partial\Omega. \end{cases} \quad (4.1)$$

The boundary condition  $\vec{n} \times \vec{n} \times \vec{E} = f(\omega)(\vec{n} \times \vec{H})$  connects the tangential electric field with the tangential magnetic field on the boundary surrounding the conductor excluded from the computational domain. Depending on the type of the conductor, in terms of SIBC, CSBC, or ITBC. Eventually the aim is to write Equations (4.1) in terms of DG-FEM (Section 3.3) in the following time-harmonic form:

$$\begin{cases} \mathbf{C}_B \mathbf{e}(\omega) + j\omega \mathbf{M}_\mu \mathbf{h}(\omega) = \mathbf{C}_Z \mathbf{e}_t(\omega) \\ \mathbf{C}_D \mathbf{h}(\omega) - j\omega \mathbf{M}_\epsilon \mathbf{e}(\omega) = 0, \end{cases} \quad (4.2)$$

where  $\mathbf{e}_t$  is the DG-FEM discretized counterpart for the tangential electric field  $\vec{n} \times \vec{n} \times \vec{E}$ , and the contents of the matrix  $\mathbf{C}_Z$  is explained later in this chapter. The matrices  $\mathbf{C}_B$ ,  $\mathbf{C}_D$ ,  $\mathbf{M}_\mu$ , and  $\mathbf{M}_\epsilon$  are introduced earlier in Equations (3.14)-(3.17).

---

## 4.2 Standard Impedance Boundary Condition (SIBC)

---

Standard Impedance Boundary Condition (SIBC) provides a connection between the tangential electric field and the tangential magnetic field on the surface of a conductive medium. Consequently, by applying SIBC, the conductive medium can be removed from the computational domain, and only the surface of the conductor needs to be modeled. The derivation of SIBC begins with the skin effect approximation. The approach presented here, is adapted from [90].

---

### 4.2.1 Skin Effect

---

To derive the relation between the tangential magnetic and electric fields in a conductor, we begin with an assumption, that the electromagnetic field in the

conducting medium is confined to a layer of thickness  $\Delta$  on the surface of the medium, see Figure 4.1(b). The minimum thickness  $t_{\min}$  of the conductor is assumed to be much larger than  $\Delta$ . First, let us seek for the solution for the electromagnetic field on the surface of the conducting medium. In other words, we are looking for a solution for the time harmonic wave equation (2.51) on the surface of the interface:

$$\nabla^2 \vec{E} - j\omega\mu(\sigma + j\omega\epsilon)\vec{E} = 0. \quad (4.3)$$

The second assumption is that the medium is a good conductor, i.e. the conduction current is much greater than the displacement current <sup>1</sup>. Therefore the wave equation can be reduced as in (2.87):

$$\nabla^2 \vec{E} - j\omega\mu\sigma\vec{E} = 0. \quad (4.4)$$

Third, we assume the lossy surface to be locally planar, i.e. the minimum radius of curvature  $R_{\min}$  of the structure is large compared to  $\Delta$ , see Figure 4.1(a). Now we can write the wave equation (2.87) locally in cartesian coordinates as

$$\frac{\partial^2 \vec{E}}{\partial x^2} + \frac{\partial^2 \vec{E}}{\partial y^2} + \frac{\partial^2 \vec{E}}{\partial z^2} - j\omega\mu\sigma\vec{E} = 0. \quad (4.5)$$

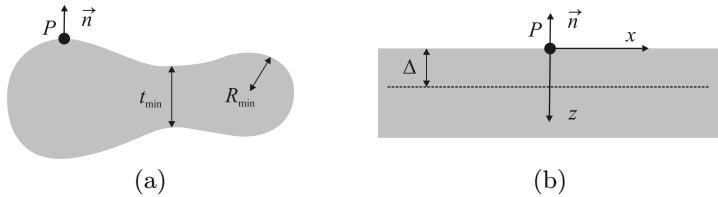


Figure 4.1.: Scheme for the skin effect approximation. The grey color denotes the conductive body. On the left side (a) are shown the prerequisites for the skin depth assumption - minimum thickness and radius of curvature of the conductive body are denoted as  $t_{\min}$  and  $R_{\min}$ , respectively. On the right side (b) is shown the layer with thickness  $\Delta$ , to which we assume the electromagnetic field to be confined. According to [90].

<sup>1</sup> Displacement current refers to the time derivative of the displacement field, i.e.  $\frac{\partial \vec{D}}{\partial t}$ , or respectively in a time-harmonic form:  $j\omega\vec{D} = j\omega\epsilon\vec{E}$ .

As the conductor is assumed to be a good conductor, the electromagnetic wave travels normal to the interface, as stated in Section 2.5. This means, that the tangential derivatives of the electric field are negligible compared to derivative in the normal direction and can be dropped out from Equation (4.5):

$$\frac{\partial^2 \vec{E}}{\partial z^2} - j\omega\mu\sigma\vec{E} = 0. \quad (4.6)$$

The solution of Equation (4.6) is a combination of exponentially growing and exponentially decaying plane wave traveling to the  $z$ -direction. Since we have assumed that the wave is confined to a layer of finite thickness, we choose the decaying solution:

$$\vec{E} = \vec{E}_0 e^{-jk_z z} = \vec{E}_0 e^{-(1+j)\sqrt{\frac{\omega\mu\sigma}{2}}z} = \vec{E}_0 e^{-(1+j)\frac{z}{\delta}}, \quad (4.7)$$

where

$$\delta = \sqrt{2/\omega\mu\sigma} \quad (4.8)$$

is so called skin depth, and  $k$  as defined in Equation (2.89). As the wave equation can be written equivalently for the magnetic field, the solution for the magnetic field is also equivalent with the electric field:

$$\vec{H} = \vec{H}_0 e^{-(1+j)\frac{z}{\delta}}. \quad (4.9)$$

The thickness  $\Delta$  can be considered as  $3\delta$ , because at  $z = 3\delta$  the amplitude of the wave have decayed into approximately 5% of the amplitude at the surface [90]. This phenomenon - electromagnetic field is confined to a thin layer of a conductor - is known as the skin effect.

---

## 4.2.2 Surface Impedance

---

Next we seek for the relation between the tangential magnetic and electric field on the surface. Taking into account the assumption of a good conductor, i.e.  $\sigma \gg \omega\epsilon$ , the time harmonic Ampere's law (2.2) can be written as

$$\nabla \times \vec{H} = (\sigma + j\omega)\vec{E} \approx \sigma\vec{E}. \quad (4.10)$$

The electric field and the magnetic field can be written elementwise as  $\vec{E} = (E_x, E_y, E_z) = E_x\hat{i} + E_y\hat{j} + E_z\hat{k}$  and  $\vec{H} = (H_x, H_y, H_z) = H_x\hat{i} + H_y\hat{j} + H_z\hat{k}$ . The tan-

gential components of the electric field at the surface can be written elementwise as

$$\sigma (E_x \hat{i} + E_y \hat{j}) = \left( \frac{\partial H_z}{\partial y} - \frac{\partial H_y}{\partial z} \right) \hat{i} + \left( \frac{\partial H_x}{\partial z} - \frac{\partial H_z}{\partial x} \right) \hat{j}. \quad (4.11)$$

After differentiating Equation (4.11) with respect to  $z$ , we obtain

$$\sigma \left( \frac{\partial E_x}{\partial z} \hat{i} + \frac{\partial E_y}{\partial z} \hat{j} \right) = \left( \frac{\partial^2 H_z}{\partial z \partial y} - \frac{\partial^2 H_y}{\partial z^2} \right) \hat{i} + \left( \frac{\partial^2 H_x}{\partial z^2} - \frac{\partial^2 H_z}{\partial z \partial x} \right) \hat{j}. \quad (4.12)$$

From Gauss' law for magnetic fields (2.3) and constitutive equation (2.24), we can conclude that

$$\frac{\partial H_z}{\partial z} = -\frac{\partial H_x}{\partial x} - \frac{\partial H_y}{\partial y}. \quad (4.13)$$

Combining Equation (4.12) and Equation (4.13) we obtain

$$\begin{aligned} \sigma \left( \frac{\partial E_x}{\partial z} \hat{i} + \frac{\partial E_y}{\partial z} \hat{j} \right) = \\ \left( -\frac{\partial^2 H_x}{\partial x \partial y} - \frac{\partial^2 H_y}{\partial y^2} - \frac{\partial^2 H_y}{\partial z^2} \right) \hat{i} + \left( \frac{\partial^2 H_x}{\partial z^2} - \frac{\partial^2 H_x}{\partial z^2} - \frac{\partial^2 H_y}{\partial x \partial y} \right) \hat{j}. \end{aligned} \quad (4.14)$$

As the conductor is good, the wave travels normal to the interface (2.91), and the tangential derivatives  $\partial/\partial x$  and  $\partial/\partial y$  can be ignored:

$$\sigma \left( \frac{\partial E_x}{\partial z} \hat{i} + \frac{\partial E_y}{\partial z} \hat{j} \right) = -\frac{\partial^2 H_y}{\partial z^2} \hat{i} + \frac{\partial^2 H_x}{\partial z^2} \hat{j}. \quad (4.15)$$

Substituting the tangential electric and magnetic fields with solutions given in (4.7) and (4.9), we get

$$-\frac{1+j}{\delta\sigma} (-H_y \hat{i} + H_x \hat{j}) = (E_x \hat{i} + E_y \hat{j}). \quad (4.16)$$

As the normal vector  $\vec{n}$  of the surface is equal to  $\hat{k}$ , we can write Equation (4.16) as a cross product with electric and magnetic fields and the normal vector  $\vec{n}$ :

$$-\frac{1+j}{\delta\sigma}\vec{n}\times\vec{H}=\vec{n}\times\vec{n}\times\vec{E}. \quad (4.17)$$

Let us denote

$$Z(\omega)=(1+j)\sqrt{\frac{\omega\mu}{2\sigma}}, \quad (4.18)$$

where  $Z(\omega)$  is surface impedance function. The more general form for the surface impedance function  $Z(\omega)$  is

$$Z(\omega)=\sqrt{\frac{j\omega\epsilon}{\sigma+j\omega\mu}}. \quad (4.19)$$

Eventually we get as a relation between the tangential electric and magnetic fields:

$$\vec{n}\times\vec{n}\times\vec{E}=Z(\omega)\vec{n}\times\vec{H}, \quad (4.20)$$

which is known as the Standard Impedance Boundary Condition (SIBC). The error made in surface impedance approximation is of order  $O(\delta^2)$  [51], i.e. the error is of order of square of the skin depth. The skin depth is inversely proportional to the frequency, and consequently the error decreases when the frequency increases. Therefore SIBC is very useful especially for high frequency applications.

---

### 4.3 Corrugated Surface Boundary Condition (CSBC)

---

The surface can be considered as smooth, if the surface roughness has much smaller dimensions than the skin depth  $\delta$  (Equation (4.8)). As the skin depth is inversely proportional to the frequency, with higher frequencies smaller roughnesses become significant. The roughness of a surface increases the losses compared to the losses of a smooth conducting surface. This increase in losses can be expressed as an increase in surface impedance function (4.19) by a correction coefficient  $K$  [36]:

$$Z_{\text{rough}}(\omega)=KZ(\omega), \quad (4.21)$$

or as an increase in attenuation constant  $\alpha$  (2.52) and decrease in the  $Q$  factor (see details in Section 4.7.1):



$$\alpha_{\text{rough}} = K\alpha \quad (4.22)$$

$$Q_{\text{rough}} = Q/K. \quad (4.23)$$

The correction coefficient  $K$  has been defined by e.g. Hammerstad and Bekkadal [44]. They fitted empirically a formula in the data obtained by Morgan [70]. The resulting formula for the correction factor is:

$$K_{\text{HCC}} = 1 + \frac{2}{\pi} \arctan \left( 1.4 \left( \frac{h_{\text{RMS}}}{\delta} \right)^2 \right), \quad (4.24)$$

where  $h_{\text{RMS}}$  is the Root Mean Square (RMS) height of the roughness as presented in Figure 4.2. The formula is known as Hammerstad's Correction Coefficient (HCC). HCC model takes only the RMS-height of the roughness into account, not the shape nor the distance of the corrugations. However, as long as the roughnesses are approximately of equal width and height the model is applicable [70]. The impedance function associated with HCC model can be written as

$$Z_{\text{HCC}}(\omega) = K_{\text{HCC}}Z(\omega). \quad (4.25)$$

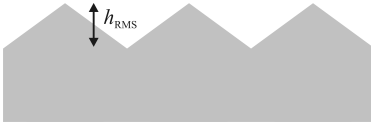


Figure 4.2: The surface approximation of the HCC model. The model takes into account only the RMS height of the surface roughness.

In Figure 4.3 is shown the effect of the surface roughness on the standard impedance function (4.19), according to the HCC model. The RMS height of the surface roughness is calculated with respect to the skin depth at the fundamental frequency of a cubical cavity resonator with edge length of 1m and the wall conductivity  $5.8 \cdot 10^7 \text{S/m}$ . This resonator is used later as a test structure in the convergence study in Section 4.7.2.3. The impedances are calculated with roughnesses of 0.1, 1, and 10 times the skin depth  $\delta$  at the fundamental frequency of the resonator.

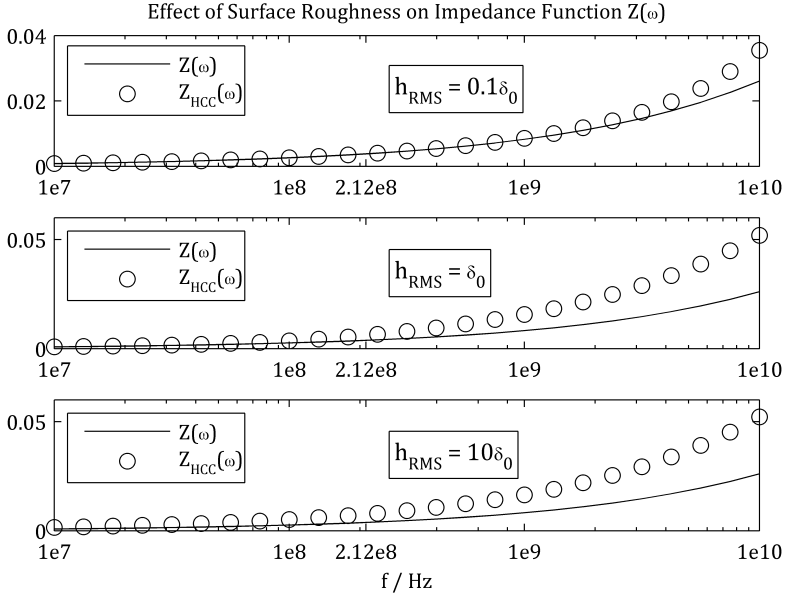


Figure 4.3.: The effect of surface roughness on the surface impedance function. Roughnesses 0.1, 1 and 10 times skin depth  $\delta_0$  are calculated with respect to the fundamental frequency ( $f_0 = 0.212\text{GHz}$ ) of cubical cavity resonator with the edge length of 1m and the wall conductivity of  $5.8 \cdot 10^7\text{S/m}$ .

---

#### 4.4 Impedance Transmission Boundary Condition (ITBC)

---

One of the limitations of the surface impedance model (Section 4.2.1) is the minimum thickness of the conductor to be modeled, see Figure 4.1(a). In [90], as the minimum thickness of a conductor to be modeled, is given three skin depths. However, let us have a closer look to the attenuation of the tangential component of the electric field of the wave traveling to  $z$ -direction (4.7), i.e. normal to the interface:

$$|\vec{E}_x(z)| = e^{-z/\delta} |\vec{E}_{x0}|, \quad (4.26)$$

where  $\vec{E}_x(z)$  is the tangential electric field at distance  $z$  from the interface, and  $\vec{E}_{x0}$  the tangential electric field at the surface. In Figure 4.4 is given an example of an attenuating wave in the conductive medium. As can be seen, at the distance

---

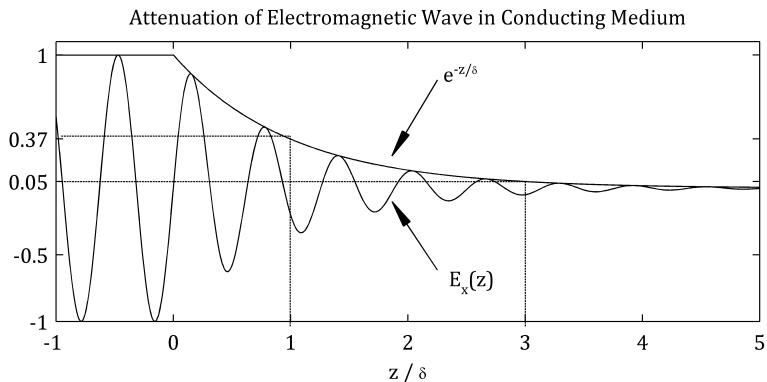


Figure 4.4.: A schematic figure of the attenuation of the electromagnetic wave in the conductive medium. The interface of the dielectric and the conductor is placed at  $z = 0$ , dielectric on the left side (negative  $z$ ) and conductor on the right side (positive  $z$ ). The wave  $E_x(z)$  is sinusoidal, therefore the envelope function  $e^{-z/\delta}$  is drawn to emphasize the attenuation. As can be seen, at  $z = \delta$ , the wave amplitude has decreased into 37% of the amplitude at the interface, and at  $z = 3\delta$  into 5%.

of one skin depth from the interface, the amplitude of the wave has decreased into 37% of the amplitude at the interface, and at the distance of three skin depths into 5%. Therefore, to model conductors with thicknesses of a few skin depths, one needs to take into account also the electromagnetic field transmitted to the other side of the conductor. In this case, the conductor is said to be partially transparent for the electromagnetic field. A conductor with thickness of the order of skin depth, is called within this thesis a thin sheet, and the impedance boundary condition applicable on surfaces of a thin sheet is called Impedance Transmission Boundary Condition (ITBC). According to [50], a thin sheet can be considered as a two-port transmission line. Therefore, before moving to the approximative boundary condition, let us have a look at the transmission line theory, and a two-port transmission line.

---

#### 4.4.1 Two-Port Transmission Line

---

The voltage  $V(z)$  and the current  $I(z)$  over a lossy transmission line can be expressed as Telegrapher's Equations:

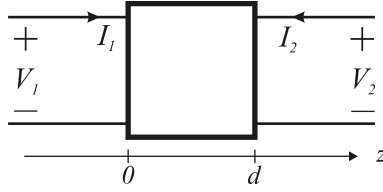


Figure 4.5.: A two-port transmission line with input voltage  $V_1$  and current  $I_1$  and output voltage  $V_2$  and current  $I_2$ . The distance between the ports is  $d$ .

$$\begin{cases} \frac{\partial^2 V(z)}{\partial z^2} = k^2 V(z) \\ \frac{\partial^2 I(z)}{\partial z^2} = k^2 I(z), \end{cases} \quad (4.27)$$

where  $k$  is the wave number within the transmission line. The general solution for the Telegrapher's Equations is

$$\begin{cases} V(z) = V_2 e^{-kz} + V_1 e^{kz} \\ I(z) = Z^{-1}(V_2 e^{-kz} + V_1 e^{kz}), \end{cases} \quad (4.28)$$

where  $Z$  is the characteristic impedance of the transmission line,  $k$  the wave number within the transmission line,  $V_1$  the input voltage,  $I_1$  the input current,  $V_2$  the output voltage, and  $I_2$  the output current (see Figure 4.5). As a specific solution for a two-port transmission line in Figure 4.5, the currents  $I_1$  and  $I_2$  into the ports 1 and 2, and the voltages  $V_1$  and  $V_2$  across the ports 1 and 2, can be written as:

$$\begin{cases} V_1 = V_2 \cosh(kd) + I_2 Z \sinh(kd) \\ I_1 = V_2 \frac{\sinh(kd)}{Z} + I_2 \cosh(kd), \end{cases} \quad (4.29)$$

where  $d$  is the distance of the ports. The solution (4.29) can also be written using impedance parameter matrix:

$$\begin{pmatrix} V_1 \\ V_2 \end{pmatrix} = \begin{pmatrix} z_{11} & z_{12} \\ z_{21} & z_{22} \end{pmatrix} \begin{pmatrix} I_1 \\ I_2 \end{pmatrix}. \quad (4.30)$$

The impedance parameters  $z_{11}$ ,  $z_{12}$ ,  $z_{21}$ , and  $z_{22}$  are defined as follows:

$$z_{11} = \frac{V_1}{I_1} \Big|_{I_2=0} = \frac{Z}{\tanh(kd)} \quad (4.31)$$

$$z_{12} = \frac{V_1}{I_2} \Big|_{I_1=0} = \frac{Z}{\sinh(kd)} \quad (4.32)$$

$$z_{21} = \frac{V_2}{I_1} \Big|_{I_2=0} = \frac{Z}{\sinh(kd)} = z_{12} \quad (4.33)$$

$$z_{22} = \frac{V_2}{I_2} \Big|_{I_1=0} = \frac{Z}{\tanh(kd)} = z_{11}. \quad (4.34)$$

Although the transmission line theory follows from the circuit analysis, which can be considered as a simplification of the Maxwell's equations, these impedance parameters are useful also for modeling thin conductive sheets in terms of the Maxwell's equations. This aspect is clarified in the next section.

---

#### 4.4.2 Thin Conductive Sheet

---

Let us next assume a thin conductive sheet shown in Figure 4.6. The sheet is a good conductor, i.e. the conduction current is much greater than the displacement current <sup>2</sup>. Therefore the material parameters of the sheet fulfill the condition  $\sigma \gg \epsilon\omega$  (2.87). The sheet has a nonzero thickness  $d$ , while the other two spatial dimensions are large compared to the thickness of the sheet. The minimum radius of the curvature is also much greater than the thickness  $d$ . The conditions are in agreement with Section 4.2.1.

According to [50] the voltages and currents of the ports Section 4.4.1 can be considered as tangential electric and magnetic fields on the different sides of the sheet, and the impedance parameter expression (4.30) for the thin sheet reads as:

$$\begin{pmatrix} \vec{n}_0 \times \vec{n}_0 \times \vec{E}_0 \\ \vec{n}_d \times \vec{n}_d \times \vec{E}_d \end{pmatrix} = \begin{pmatrix} z_{11} & -z_{12} \\ z_{12} & -z_{11} \end{pmatrix} \begin{pmatrix} \vec{n}_0 \times \vec{H}_0 \\ \vec{n}_d \times \vec{H}_d \end{pmatrix}, \quad (4.35)$$

with the impedance parameters equal to (4.31) and (4.32). According to [95], the impedance parameter can be written as

---

<sup>2</sup> Displacement current is time derivative of the displacement field.

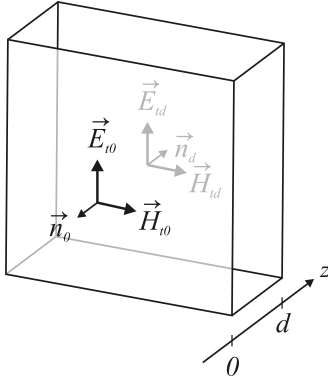


Figure 4.6: A schematic figure of a thin sheet and the tangential electromagnetic field on the surfaces of it. The thickness of the sheet is  $d$  and  $\vec{E}_{t0}$  is a shorthand notation for  $\vec{n}_0 \times \vec{n}_0 \times \vec{E}_0$  and  $\vec{H}_{t0}$  for  $\vec{n}_0 \times \vec{H}_0$ . Respectively for the tangential fields at the interface  $z = d$ .

$$z_{11} = -\frac{j\omega\mu}{k} \frac{1}{\tan(kd)} \quad (4.36)$$

$$z_{12} = -\frac{j\omega\mu}{k} \frac{1}{\sin(kd)}, \quad (4.37)$$

where  $d$  is the thickness of the sheet, and  $k$  and  $\mu$  the wave number and permeability within the sheet, respectively.

---

#### 4.5 Dispersive Boundary Conditions for DG-FEM

---

Modeling conductive medium in a computational domain requires significantly denser mesh than modeling of dielectrics. According to [11], to obtain a good accuracy when modeling dielectrics, the mesh element size  $l_e$  should be

$$l_e = \lambda/10, \quad (4.38)$$

where  $\lambda$  is the wavelength in the dielectric. At the same time, to model accurately the damping of the wave in a conductor, the suitable mesh element size in a conductor is

$$l_e = \delta/10, \quad (4.39)$$

where  $\delta$  is the skin depth (4.8) of the conductor. As an example, if we have a copper body in a vacuum, and the given frequency is 10MHz, a suitable mesh

---

element size in the vacuum is 3.3mm, whereas in copper, the suitable size is only  $2\mu\text{m}$ . In words, the mesh within the conductor should be more than thousand times denser than in the vacuum. This leads clearly into two problems: The system matrix becomes ill-conditioned, and the Central Processing Unit (CPU)-time required for solving the problem increases significantly.

Therefore, it is highly desirable to exclude the conductive bodies from the computational domain. This can be done by means of impedance boundary conditions. The conductor itself is removed from the computational domain, and only the surface of it is modeled. In the previous sections, three different kind of surface impedance boundary conditions were introduced, which can be used for this purpose:

- (1) Standard Impedance Boundary Condition (SIBC) in Section 4.2.1 to model conductors with smooth surfaces and thicknesses much greater than the skin depth
- (2) Corrugated Surface Boundary Condition (CSBC) in Section 4.3 to model conductors with rough surfaces and thicknesses much greater than the skin depth
- (3) Impedance Transmission Boundary Condition (ITBC) in Section 4.4 to model conductors with thicknesses of order of the skin depth

In case of SIBC and CSBC the conductor is removed from the domain, and only the surface of the conductor is modeled by means of boundary condition. In case of ITBC, the conductor is removed from the domain as well, and the surfaces are modeled by means of ITBC. However, in case of ITBC, the fields on different sides of the excluded conductor are mutually dependent.

In this section, implementations of these three boundary conditions to frequency domain DG-FEM are presented. The implementation has been published by the author in [98]. Applying these frequency dependent, or dispersive, boundary conditions to frequency domain DG-FEM leads to a complex, nonlinear EVP. However, in Section 4.6, a scheme to solve the complex nonlinear EVP as a linear EVP is presented. The presented scheme takes into account the dispersive nature of the impedance boundary conditions in a wide frequency band.

---

#### 4.5.1 SIBC

---

Let us begin with the simplest of previously introduced boundary conditions, Standard Impedance Boundary Condition (SIBC), see Section 4.2.1. Let us assume a three dimensional computational domain  $\Omega$ , which includes a conducting

body, see Figure 4.7 (a). The conductor fulfills the requirements for SIBC approximation, see section 4.2.1. To apply SIBC, we remove the conductor, and replace it with a domain boundary  $\Gamma_C$ , see Figure 4.7 (b).

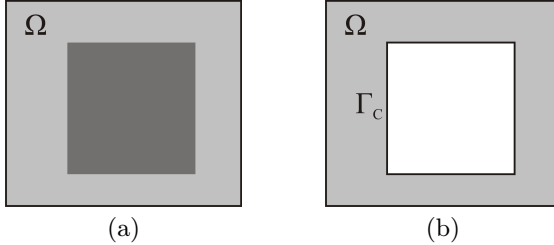


Figure 4.7.: On the left (a) is shown the computational domain  $\Omega$  (denoted with light grey color) with a conducting body (dark grey). On the right (b) the conductor is removed from the domain, and replaced with a surface  $\Gamma_C$ .

Let us recall the DG-FEM applied to the Maxwell's equations in Section 3.3. Let us rewrite Equation (3.13) in a time-harmonic form, i.e. replacing the time derivatives with the variable  $j\omega$ :

$$\begin{cases} \mathbf{C}_B \mathbf{e} + j\omega \mathbf{M}_\mu \mathbf{h} = 0 \\ \mathbf{C}_D \mathbf{h} - j\omega \mathbf{M}_\varepsilon \mathbf{e} = 0, \end{cases} \quad (4.40)$$

where the curl-matrices  $\mathbf{C}_D$  and  $\mathbf{C}_B$  are defined elementwise as

$$C_B^{jq \ ip} = \delta_{ij} \int_{V_j} (\nabla \times \varphi_H^{jq}) \cdot \varphi_E^{ip} dV_j + \frac{1}{2} \int_{\partial V_j} (\vec{n} \times \varphi_E^{ip}) \cdot \varphi_H^{jq} \vec{dA}_j \quad (4.41)$$

$$C_D^{jq \ ip} = \delta_{ij} \int_{V_j} (\nabla \times \varphi_E^{jq}) \cdot \varphi_H^{ip} dV_j + \frac{1}{2} \int_{\partial V_j} (\vec{n} \times \varphi_H^{ip}) \cdot \varphi_E^{jq} \vec{dA}_j, \quad (4.42)$$

and matrices  $\mathbf{M}_\mu$  and  $\mathbf{M}_\varepsilon$  elementwise as:



$$M_{\mu}^{jq\ ip} = \delta_{ij} \int_{\Omega_j} \mu_j \varphi_H^{jq} \cdot \varphi_H^{ip} \, dV_j, \quad (4.43)$$

$$M_{\epsilon}^{jq\ ip} = \delta_{ij} \int_{\Omega_j} \epsilon_j \varphi_E^{jq} \cdot \varphi_E^{ip} \, dV_j. \quad (4.44)$$

As explained in Section 3.3, the second terms in curl-matrices (4.41) and (4.42) originate from the numerical fluxes, defined in Equations (3.11) and (3.12):

$$\vec{n} \times \vec{E}^* = \frac{1}{2} \vec{n} \times (\vec{E}^- + \vec{E}^+) \quad (4.45)$$

$$\vec{n} \times \vec{H}^* = \frac{1}{2} \vec{n} \times (\vec{H}^- + \vec{H}^+). \quad (4.46)$$

The numerical fluxes enforce the continuity of tangential electric and magnetic fields on the element interfaces, which is otherwise not ensured in DG-FEM. However, we can also utilize the numerical fluxes on the boundary of the domain to apply boundary conditions. In the case of SIBC, the numerical fluxes read as:

$$\vec{n} \times \vec{E}^* = Z(\omega) \vec{n} \times \vec{n} \times \vec{H}^- \quad (4.47)$$

$$\vec{n} \times \vec{H}^* = 0. \quad (4.48)$$

This leads to a modification to the curl-matrices on the element interfaces which lay on the domain boundary  $\Gamma_C$ :

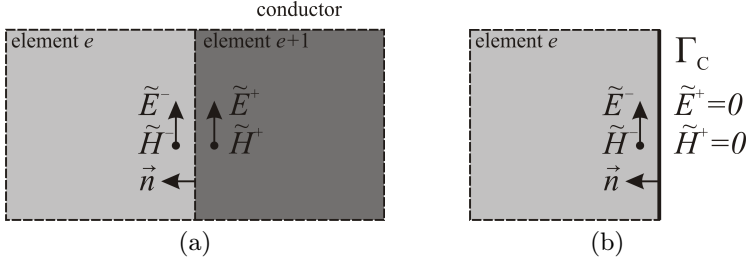


Figure 4.8.: A schematic illustration of an interface of a conductor in DG-FEM. On the left (a) are presented DoFs on the interface of elements  $e$  and  $e + 1$ . The element  $e + 1$  is inside the conductor, and no boundary conditions are applied on the interface. The numerical flux enforces the continuity of the tangential fields on the interface:  $\vec{n} \times \vec{E}^* = \frac{1}{2} \vec{n} \times (\vec{E}^- + \vec{E}^+)$ ,  $\vec{n} \times \vec{H}^* = \frac{1}{2} \vec{n} \times (\vec{H}^- + \vec{H}^+)$ . On the right (b) the element interface is aligned with a domain boundary  $\Gamma_C$ , and the element  $e + 1$  does not exist, as well as the DoFs, as they are outside the domain. The numerical flux (4.47) couples the electric field to the magnetic field on the interface in the element  $e$ :  $\vec{n} \times \vec{E}^* = Z(\omega) \vec{n} \times \vec{n} \times \vec{H}^-$ .

$$C_B^{jq \ ip} = \delta_{ij} \int_{V_j} (\nabla \times \varphi_H^{jq}) \cdot \varphi_E^{ip} \, dV_j + \begin{cases} \int_{\partial V_j \in \Gamma_C} Z(\omega) (\vec{n} \times \vec{n} \times \varphi_H^{ip}) \cdot \varphi_H^{jq} \, d\vec{A}_j \\ \int_{\partial V_j \notin \Gamma_C} \frac{1}{2} (\vec{n} \times \varphi_E^{ip}) \cdot \varphi_H^{jq} \, d\vec{A}_j \end{cases} \quad (4.49)$$

$$C_D^{jq \ ip} = \delta_{ij} \int_{V_j} (\nabla \times \varphi_E^{jq}) \cdot \varphi_H^{ip} \, dV_j + \int_{\partial V_j} \frac{1}{2} (\vec{n} \times \varphi_H^{ip}) \cdot \varphi_E^{jq} \, d\vec{A}_j \quad (4.50)$$

Next we split curl matrix  $\mathbf{C}_B$  into two matrices,  $\mathbf{C}_B$  and  $\mathbf{C}_Z$ , defined elementwise as:

$$\mathbf{C}_B^{jq\ ip} = \delta_{ij} \int_{V_j} (\nabla \times \varphi_H^{jq}) \cdot \varphi_E^{ip} \, dV_j + \int_{\partial V_j \notin \Gamma_C} \frac{1}{2} (\vec{n} \times \varphi_E^{ip}) \cdot \varphi_H^{jq} \vec{dA}_j \quad (4.51)$$

$$\mathbf{C}_Z^{jq\ ip} = \int_{\partial V_j \in \Gamma_C} Z(\omega) (\vec{n} \times \vec{n} \times \varphi_H^{ip}) \cdot \varphi_H^{jq} \vec{dA}_j \quad (4.52)$$

In words, the matrix  $\mathbf{C}_B$  is defined as (4.51) everywhere else except on the boundary  $\Gamma_C$  where the flux term is zero. The missing flux is included in the matrix  $\mathbf{C}_Z$ , which is zero everywhere else except on the boundary  $\Gamma_C$ , where it is defined as in (4.52). The matrix  $\mathbf{C}_D$  (4.50) remains the same everywhere in the domain. Eventually we can write the Maxwell's equations in a matrix form with the new matrix  $\mathbf{C}_Z$ :

$$\begin{cases} \mathbf{C}_B \mathbf{e} + j\omega \mathbf{M}_\mu \mathbf{h} = \mathbf{C}_Z Z(\omega) \mathbf{h} \\ \mathbf{C}_D \mathbf{h} - j\omega \mathbf{M}_\epsilon \mathbf{e} = 0. \end{cases} \quad (4.53)$$

Equations 4.53 are now the form of the discrete Maxwell's equations, which was set as a goal of this section, see Equation (4.2). In the following section, similar scheme for modeling corrugated surface by means of CSBC is presented.

---

## 4.5.2 CSBC

---

The scheme for corrugated surfaces is similar to the scheme for SIBC. The difference is in the impedance function,  $Z(\omega)$  is replaced with  $Z_{\text{HCC}}(\omega)$ . Therefore the numerical fluxes (4.47) read as:

$$\vec{n} \times \tilde{\mathbf{E}}^* = Z_{\text{HCC}}(\omega) \vec{n} \times \vec{n} \times \tilde{\mathbf{H}}^- \quad (4.54)$$

$$\vec{n} \times \tilde{\mathbf{H}}^* = 0, \quad (4.55)$$

and the Maxwell's equations with CSBC read as:

$$\begin{cases} \mathbf{C}_B \mathbf{e} + j\omega \mathbf{M}_\mu \mathbf{h} = Z_{\text{HCC}}(\omega) \mathbf{C}_Z \mathbf{h} \\ \mathbf{C}_D \mathbf{h} - j\omega \mathbf{M}_\epsilon \mathbf{e} = 0. \end{cases} \quad (4.56)$$


---

In the following section, a scheme for modeling thin conductive sheets by means of ITBC is presented. This approach deviates from the SIBC and CSBC approaches.

---

### 4.5.3 ITBC

---

The scheme for ITBC is somewhat different compared to the SIBC. In case of ITBC, the thin conductive body, see Figure 4.9 (a), is replaced with colocated domain boundaries,  $\Gamma_S$  and  $\Gamma_T$ , and consequently with a single element interface, see Figure 4.9 (b). Consequently the impedance matrix (4.35) (see Section 4.4.2) changes. Now the thin sheet thickness  $d$  has been shrunk into a element interface, and consequently the normal vectors of the different sides of the thin sheet can be written as  $\vec{n}_0 = -\vec{n}_d = \vec{n}$ , see Figure 4.10.

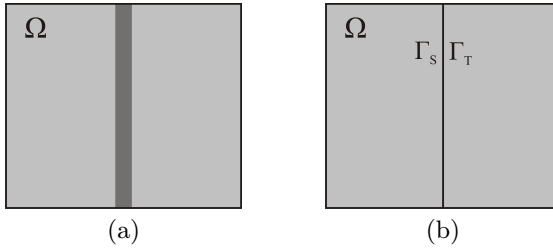


Figure 4.9.: On the left (a) is shown the computational domain  $\Omega$  with a conducting body (denoted with dark grey color). On the right (b) the conductor is shrunk into two colocated boundaries  $\Gamma_S$  and  $\Gamma_T$ .

The impedance matrix (4.35) matrix can be written as

$$\begin{pmatrix} \vec{n} \times \vec{n} \times \vec{E}_0 \\ \vec{n} \times \vec{n} \times \vec{E}_d \end{pmatrix} = \begin{pmatrix} z_{11} & -z_{12} \\ z_{12} & -z_{11} \end{pmatrix} \begin{pmatrix} \vec{n} \times \vec{H}_0 \\ \vec{n} \times \vec{H}_d \end{pmatrix}. \quad (4.57)$$

Due to attenuation within a thin conductive sheet, the tangential electromagnetic field is not equal on the different sides of the sheet. In other words, a thin sheet causes a discontinuity of the tangential electromagnetic field on the different sides of the sheet. Therefore, instead of enforcing the continuity within an element interface, as is the case on a normal element interface in DG-FEM method, we want to enforce a discontinuity on the interface. Therefore the numerical fluxes, Equations (3.11) and (3.12), read as (see also Figure 4.10):

$$\begin{aligned}\vec{n} \times \tilde{\mathbf{E}}^* &= \vec{n} \times \vec{n} \times (Z_{11}(\omega)\tilde{\mathbf{H}}^- + \times Z_{12}(\omega)\tilde{\mathbf{H}}^+) & (4.58) \\ \vec{n} \times \tilde{\mathbf{H}}^* &= 0. & (4.59)\end{aligned}$$

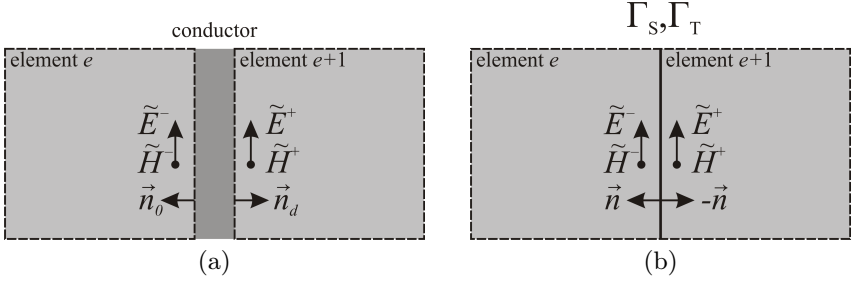


Figure 4.10.: A schematic illustration of an interface of a conductor in DG-FEM. On the left (a) are presented DoFs on the interfaces of elements  $e$  and  $e+1$ , with a conductor in between of them. On the right (b) the conductor has been removed and been replaced with two colocated domain interfaces  $\Gamma_S$  and  $\Gamma_T$ , which are aligned with the interfaces of the elements  $e$  and  $e+1$ . The DoFs on the different sides of the interface are discontinuous, and they are coupled by the numerical flux (4.58):  $\vec{n} \times \tilde{\mathbf{E}}^* = \vec{n} \times \vec{n} \times (Z_{11}(\omega)\tilde{\mathbf{H}}^- + \times Z_{12}(\omega)\tilde{\mathbf{H}}^+)$ .

Furthermore, as with the SIBC (4.49), the curl matrix  $\mathbf{C}_D$  is divided into three parts:

$$C_B^{jq \ ip} = \delta_{ij} \int_{V_j} (\nabla \times \varphi_H^{jq}) \cdot \varphi_E^{ip} \, dV_j + \int_{\partial V_j \notin (\Gamma_S \cup \Gamma_T)} \frac{1}{2} (\vec{n} \times \varphi_E^{ip}) \cdot \varphi_H^{jq} \, \vec{dA}_j \quad (4.60)$$

$$C_{Z1}^{jq \ ip} = \delta_{ij} \int_{\partial V_j \in \Gamma_S} Z_{11}(\omega) (\vec{n} \times \vec{n} \times \varphi_H^{ip}) \cdot \varphi_H^{jq} \, \vec{dA}_j \quad (4.61)$$

$$C_{Z2}^{jq \ ip} = (1 - \delta_{ij}) \int_{\partial V_j \in \Gamma_T} Z_{12}(\omega) (\vec{n} \times \vec{n} \times \varphi_H^{ip}) \cdot \varphi_H^{jq} \, \vec{dA}_j \quad (4.62)$$

where  $Z_{11}(\omega)$  and  $Z_{12}(\omega)$  are the impedance parameters  $z_{11}$  (4.31) and  $z_{12}$  (4.32), respectively. Impedances  $Z_{11}(\omega)$  and  $Z_{12}(\omega)$  can also be considered as surface impedance and transmission impedance of ITBC approximation. Finally, the Maxwell's equations for ITBC case can be written as:

$$\begin{cases} \mathbf{C}_B \mathbf{e} + j\omega \mathbf{M}_\mu \mathbf{h} = (Z_{11}(\omega) \mathbf{C}_{Z1} + Z_{12}(\omega) \mathbf{C}_{Z2}) \mathbf{h} \\ \mathbf{C}_D \mathbf{h} - j\omega \mathbf{M}_\epsilon \mathbf{e} = 0. \end{cases} \quad (4.63)$$

The procedure for solving the discretized Maxwell's equations, as well as equations (4.53) and (4.56), is presented in the following.

---

## 4.6 FD Solver Implementation

---

All of the previously presented boundary conditions, SIBC (4.19), CSBC (4.25) and ITBC (4.35), include a complex, frequency-dependent, impedance function. This leads to a nonlinear, complex Eigenvalue Problem (EVP). In this section, a scheme to solve for the nonlinear complex EVP iteratively, is presented. Additionally, although the frequency-dependency of the impedance functions is taken into account, the EVP is solved as a linear EVP. This approach has been published by the author in [98]. Let us first summarize the impedance boundary conditions and the resulting equations to be solved.

$$\begin{array}{l} \text{SIBC equations: } \begin{cases} \mathbf{C}_B \mathbf{e} + j\omega \mathbf{M}_\mu \mathbf{h} = Z(\omega) \mathbf{C}_Z \mathbf{h} \\ \mathbf{C}_D \mathbf{h} - j\omega \mathbf{M}_\epsilon \mathbf{e} = 0. \end{cases} \\ \text{Impedance function: } Z(\omega) = \sqrt{\frac{j\omega\epsilon}{\sigma + j\omega\mu}} \end{array} \quad (4.64)$$

$$\begin{array}{l} \text{CSBC equations: } \begin{cases} \mathbf{C}_B \mathbf{e} + j\omega \mathbf{M}_\mu \mathbf{h} = Z_{\text{HCC}}(\omega) \mathbf{C}_Z \mathbf{h} \\ \mathbf{C}_D \mathbf{h} - j\omega \mathbf{M}_\epsilon \mathbf{e} = 0. \end{cases} \\ \text{Impedance function:} \\ Z_{\text{HCC}}(\omega) = \left( 1 + \frac{2}{\pi} \arctan \left[ 1.4 \left( \frac{h_{\text{RMS}}}{\delta} \right)^2 \right] \right) Z(\omega) \end{array} \quad (4.65)$$

ITBC equations:  $\begin{cases} \mathbf{C}_B \mathbf{e} + j\omega \mathbf{M}_\mu \mathbf{h} = (Z_{11}(\omega) \mathbf{C}_{Z1} + Z_{12}(\omega) \mathbf{C}_{Z2}) \mathbf{h} \\ \mathbf{C}_D \mathbf{h} - j\omega \mathbf{M}_\varepsilon \mathbf{e} = 0. \end{cases}$

Impedance functions:  $Z_{11}(\omega) = \frac{j\omega\mu}{k} \frac{1}{\tan(kd)}$  (4.66)

$Z_{12}(\omega) = \frac{j\omega\mu}{k} \frac{1}{\sin(kd)}$

Let us derive the iterative scheme for solving the nonlinear complex EVP for SIBC. For CSBC and ITBC the procedure is almost equal. Let us solve for the  $\mathbf{e}$  of the second equation of Maxwell's equations in (4.64):

$$\mathbf{e} = \frac{1}{j\omega} \mathbf{M}_\varepsilon^{-1} \mathbf{C}_D \mathbf{h}, \quad (4.67)$$

and substitute it into the first equation:

$$\mathbf{C}_B \frac{1}{j\omega} \mathbf{M}_\varepsilon^{-1} \mathbf{C}_D \mathbf{h} + j\omega \mathbf{M}_\mu \mathbf{h} = Z(\omega) \mathbf{C}_Z \mathbf{h}. \quad (4.68)$$

After reorganizing the terms in Equation (4.68), the following nonlinear, complex EVP is obtained:

$$\left[ \mathbf{M}_\mu^{-1} \mathbf{C}_B \mathbf{M}_\varepsilon^{-1} \mathbf{C}_D - j\omega Z(\omega) \mathbf{M}_\mu^{-1} \mathbf{C}_Z \right] \mathbf{h} = \omega^2 \mathbf{h}. \quad (4.69)$$

Let us introduce the following shorthand notations:

$$\mathbf{A} = \mathbf{M}_\mu^{-1} \mathbf{C}_B \mathbf{M}_\varepsilon^{-1} \mathbf{C}_D \quad (4.70)$$

$$\mathbf{B} = \mathbf{M}_\mu^{-1} \mathbf{C}_Z \quad (4.71)$$

$$Z'(\omega) = j\omega Z(\omega), \quad (4.72)$$

to be able to wirete the EVP (4.69) in a compact form:

$$[\mathbf{A} - Z' \mathbf{B}] \mathbf{h} = \omega^2 \mathbf{h}. \quad (4.73)$$

Since solving a complex nonlinear EVP as (4.73) is challenging, a scheme to solve (4.73) as a linear EVP using fixed-point iteration is presented.

The scheme for solving for the EVP (4.73) is the following: The first step is to give an initial guess for impedance function  $Z'$  (4.72). In our numerical examples, the initial guess for impedance is PEC, i.e. the conductivity is infinite and consequently the impedance  $Z'$  is zero. However, the initial guess is ambiguous. The EVP obtained, after the initial guess of the impedance, is linear. In the second step the linear EVP is solved, to obtain a initial set of eigenfrequencies. In the third step, the impedance  $Z'$  is calculated at these eigenfrequencies, to obtain a set of new, linear EVP:s. Fourth, these EVPs are solved, to obtain more accurate eigenfrequencies and consequently more accurate impedance values. The steps three and four are repeated, until a requested tolerance for the eigenfrequency is obtained.

To be more structured and compact, the same scheme is presented as bullet points. For the  $i^{\text{th}}$  eigenfrequency  $\omega_i$ , the procedure is the following:

1. Initial guess for the impedance:  $Z'_i{}^{(0)} = Z_0$
2. Solve the linear EVP  $[\mathbf{A} - Z'_i{}^{(0)}\mathbf{B}]\mathbf{h} = (\omega_i^{(1)})^2\mathbf{h}$ , to obtain  $\omega_i^{(1)}$
3. Correction for the impedance:  $Z'_i{}^{(1)} = Z'_i(\omega_i^{(1)})$
4. Solve the linear EVP  $[\mathbf{A} - Z'_i{}^{(1)}\mathbf{B}]\mathbf{h} = (\omega_i^{(2)})^2\mathbf{h}$ , to obtain more accurate  $\omega_i^{(2)}$
- ⋮
- Repeat the step 3. and 4. until the eigenfrequency  $\omega_i$  reaches the requested tolerance.

This procedure can be repeated for as many eigenvalues as required, therefore the scheme can be considered as a wideband scheme. The scheme is also presented as a flowchart, see Figure 4.11.



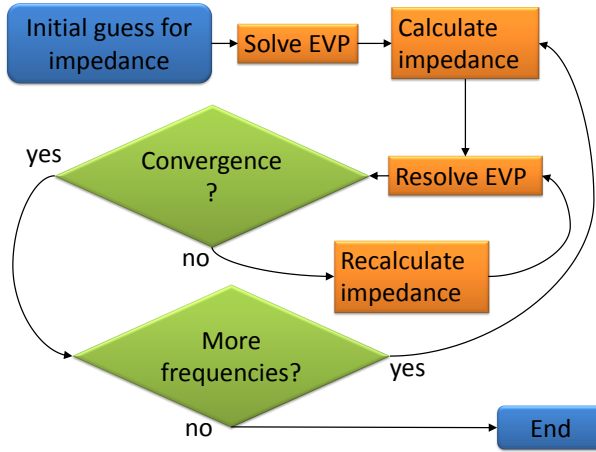


Figure 4.11.: Flow chart of solving the nonlinear Eigenvalue Problem (EVP) as fixed point iteration.

---

## 4.7 Numerical Examples

---

In this section, the schemes for solving the complex nonlinear EVP, arising from applying dispersive impedance boundary conditions, proposed in Sections 4.5.1, 4.5.2 and 4.5.3, are verified and validated by numerical examples and convergence studies.

To verify and validate the proposed schemes, cavity resonators including conductive media are studied. The presence of imperfectly conducting media in a resonator causes losses in energy, therefore a suitable parameter to verify the impedance boundary conditions is the  $Q$  factor, which is introduced in the next section. Another parameter to be studied, is the fundamental resonance frequency  $f_0$  of a cavity resonator.

Section 4.7.2 focuses on cavity resonators with conductive, lossy walls. As a numerical example in Section 4.7.2.1,  $Q$  factors of various cavity resonators with different geometries and wall conductivities are studied, and the results are compared with the results obtained by a commercial software, as well as the Power Loss method (Section 4.7.1 provides further details). After the numerical example, convergence studies for SIBC and CSBC schemes are performed in Sections 4.7.2.2 and 4.7.2.3, respectively.

The focus of Section 4.7.3 is on resonators including thin, conductive, sheets. In Section 4.7.3.1, the effect of the sheet thickness on the accuracy of the ITBC

model is studied, by investigating conductive sheets with different thicknesses and conductivities. The ITBC model is also compared with the SIBC model. In Section 4.7.3.2 the convergence study of ITBC model is performed for different sheet geometries and material parameters.

---

#### 4.7.1 Resonator Losses

---

The time dependency of the electromagnetic energy  $U$  in the resonator can be written as a differential equation

$$\frac{dU}{dt} = -\frac{\omega_0}{Q}U. \quad (4.74)$$

One solution for Equation (4.74) is

$$U = U_0 e^{-\omega_0 t/Q}, \quad (4.75)$$

where  $U_0$  is the initial energy of the resonator,  $\omega_0$  the resonance frequency, and  $Q$  quality factor, defined as

$$Q = \begin{cases} 2\pi \frac{\text{stored energy}}{\text{energy loss per oscillation}} \\ \omega_0 \frac{\text{stored energy}}{\text{average power loss}}. \end{cases} \quad (4.76)$$

In words, the energy stored initially in the resonator,  $U_0$ , attenuates exponentially inversely proportional to the quality factor  $Q$ . According to [52], the time dependency of energy in Equation (4.75) means that the fields in the resonator need to attenuate as well. The attenuating electric field does not include only one frequency, but a superposition of several frequencies, i.e.  $\omega = \omega_0 + \Delta\omega$ . The attenuating electric field can be written as:

$$\vec{E}(t) = \vec{E}_0 e^{-\omega_0 t/(2Q)} e^{-j(\omega_0 + \Delta\omega)t}, \quad (4.77)$$

where  $\vec{E}_0$  is the initial electric field in the resonator. Equation (4.77) can also be written equivalently as an integral:

$$\vec{E}(t) = \frac{1}{\sqrt{2\pi}} \int_{-\infty}^{\infty} \vec{E}(\omega) e^{-j\omega t} d\omega, \quad (4.78)$$

with

$$\vec{E}(\omega) = \frac{1}{\sqrt{2\pi}} \int_0^\infty \vec{E}_0 e^{-\omega_0 t / (2Q)} e^{-j(\omega_0 + \Delta\omega)t} dt. \quad (4.79)$$

From Equation (4.79) we can deduce the following energy distribution of the resonator:

$$|\vec{E}(\omega)|^2 \sim \frac{1}{(\omega - \omega_0 - \Delta\omega)^2 + \left(\frac{\omega_0}{2Q}\right)^2}. \quad (4.80)$$

The energy distribution is shown schematically in Figure 4.12.

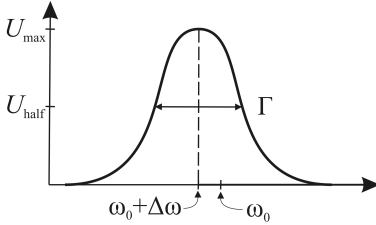


Figure 4.12: A schematic figure of the energy distribution with respect to the angular frequency in a lossy resonator.  $\Gamma$  is the half-width of the resonance peak. According to [52], page 430.

The quality factor  $Q$  can be defined using the half-power-width  $\Gamma$  of the resonance curve in Figure 4.12:

$$Q = \frac{\omega_0}{\Gamma}. \quad (4.81)$$

According to [52], the  $Q$  factor can also be written as

$$Q = \frac{\omega_0}{2\text{Im}\{\omega\}}. \quad (4.82)$$

Equation (4.82) is used to calculate the  $Q$  factors in the numerical examples in the following sections, since the output of the eigenmode solver is the complex eigenfrequency. As the reference value for the  $Q$  factor, a result calculated by a Power Loss method [40] is used. According to [78], the  $Q$  factor for a vacuum-filled rectangular cavity resonator is given as

$$Q = \frac{\pi\eta_0}{4R_S} \frac{2l_y(l_x^2 + l_z^2)^{2/3}}{l_x l_z(l_x^2 + l_z^2) + 2l_y(l_x^3 + l_z^3)}, \quad (4.83)$$

---

where  $l_x$ ,  $l_y$ , and  $l_z$  are the dimensions of the rectangular resonator,  $\eta_0$  free-space wave impedance, and  $R_S$  surface resistance. As the Q factor is sensitive for the losses in a resonator, it is a useful parameter to validate and verify the developed SIBC schemes. Numerical examples and convergence studies are carried out in the following sections.

---

### 4.7.2 Resonator with Lossy Walls

---

In this section, the SIBC and CSBC schemes are validated and verified. Validation and verification are done by investigating a cavity resonator with conductive, lossy walls. First, as a numerical example, Q factors of various cubical cavity resonators are investigated. After the numerical example, the convergence studies of SIBC and CSBC schemes are presented, respectively.

In Section 4.7.2.1, the Q factor of a cubical cavity resonator is investigated, and the comparison with a commercial software, as well as Power Loss method (see Section 4.7.1), is carried out. In Sections 4.7.2.2 and 4.7.2.3, the convergence studies for SIBC and CSBC are presented, by investigating Q factors of cavity resonators with different sizes, conductivities, and wall roughnesses.

---

#### 4.7.2.1 Q Factor of Cavity Resonator

---

In this numerical example, the fundamental resonance frequencies  $f_0$ , and the Q factors of rectangular cavity resonators are studied. In addition to the iterative eigenmode solver introduced in Section 4.6 (later referred to as EMDG), the results are obtained by the Power Loss method, and CST Microwave Studio <sup>®</sup> (CST) Eigenmode solver.

The fundamental frequencies and the Q factors are calculated for resonators with edge lengths of 1m and 10, and wall conductivities of  $5.8 \cdot 10^5 \text{S/m}$ ,  $5.8 \cdot 10^7 \text{S/m}$ , and  $5.8 \cdot 10^9 \text{S/m}$ . EMDG and CST Eigenmode solver results are calculated with a mesh resolution of 10 mesh lines/resonator edge, which corresponds to 14.1 mesh lines/wavelength, independent of the size of the resonator. The basis function order for EMDG simulations are zero.

The Q factors of the different resonators, calculated by Power Loss method, CST Eigenmode solver, and iterative EMDG method are given in Tables 4.1-4.5.

Table 4.1.: Fundamental resonance frequencies  $f_0$  and Q factors of a cavity resonator with edge length 10m and wall conductivity of  $5.8 \cdot 10^5 \text{S/m}$  obtained by Power Loss method, EMDG method, and CST Eigenmode solver.

	$f_0$	Q factor
Power Loss method	$2.1199 \cdot 10^7 \text{Hz}$	$2.32 \cdot 10^4$
EMDG	$2.1285 \cdot 10^7 \text{Hz}$	$2.31 \cdot 10^4$
CST EM solver	$2.1111 \cdot 10^7 \text{Hz}$	$2.37 \cdot 10^4$

Table 4.2.: Fundamental resonance frequencies  $f_0$  and Q factors of a cavity resonator with edge length 1m and wall conductivity of  $5.8 \cdot 10^7 \text{S/m}$  obtained by Power Loss method, EMDG method, and CST Eigenmode solver.

	$f_0$	Q factor
Power Loss method	$2.1199 \cdot 10^8 \text{Hz}$	$7.34 \cdot 10^4$
EMDG	$2.1283 \cdot 10^8 \text{Hz}$	$7.32 \cdot 10^4$
CST EM solver	$2.1111 \cdot 10^8 \text{Hz}$	$7.50 \cdot 10^4$

Table 4.3.: Fundamental resonance frequencies  $f_0$  and Q factors of a cavity resonator with edge length 1m and wall conductivity of  $5.8 \cdot 10^9 \text{S/m}$  obtained by Power Loss method, EMDG method, and CST Eigenmode solver.

	$f_0$	Q factor
Power Loss method	$2.1199 \cdot 10^8 \text{Hz}$	$7.34 \cdot 10^5$
EMDG	$2.1284 \cdot 10^8 \text{Hz}$	$7.32 \cdot 10^5$
CST EM solver	$2.1111 \cdot 10^8 \text{Hz}$	$7.50 \cdot 10^5$

Table 4.4.: Fundamental resonance frequencies  $f_0$  and Q factors of a cavity resonator with edge length 10m and wall conductivity of  $5.8 \cdot 10^9 \text{S/m}$  obtained by Power Loss method, EMDG method, and CST Eigenmode solver.

	$f_0$	Q factor
Power Loss method	$2.1199 \cdot 10^7 \text{Hz}$	$2.32 \cdot 10^6$
EMDG	$2.1286 \cdot 10^7 \text{Hz}$	$2.31 \cdot 10^6$
CST EM solver	$2.1111 \cdot 10^7 \text{Hz}$	$2.37 \cdot 10^6$

Table 4.5.: Fundamental resonance frequencies  $f_0$  and Q factors of a cavity resonator with edge length 1m and wall conductivity of  $5.8 \cdot 10^5 \text{S/m}$  obtained by Power Loss method, EMDG method, and CST Eigenmode solver.

	$f_0$	Q factor
Power Loss method	$2.1199 \cdot 10^8 \text{Hz}$	$7.34 \cdot 10^3$
EMDG	$2.1282 \cdot 10^8 \text{Hz}$	$7.32 \cdot 10^3$
CST EM solver	$2.1111 \cdot 10^8 \text{Hz}$	$7.50 \cdot 10^3$

As can be seen in Tables 4.1-4.5, the agreement of EMDG results with the results obtained by the Power Loss method is very good, on a wide range of conductivities and resonator sizes. In the following section, the resonators are further investigated to obtain a convergence study.

---

#### 4.7.2.2 SIBC Convergence Study

---

In order to verify SIBC (see implementation in Section 4.5.1), a convergence study is performed, by investigating cubical cavity resonators with different wall conductivities and cavity edge lengths. The details of the resonators to be studied are equivalent with the resonators investigated in the previous section, and the summary is given in Table 4.6. The Q factors given in the table are calculated by the Power Loss method, and are used as reference results within the convergence study. The mesh for SIBC simulations is a simple hexahedral mesh with a mesh resolution  $h$  of 4.2-14.1 mesh element edges/wavelength, see Figure 4.13. The basis function polynomial orders ( $\mathcal{P}$  in Equations (3.7) and (3.8) in Section 3.3) for the simulations are 0, 1, 2, and 3.

Table 4.6.: Specifications and the reference values for the Q factor of the cavity resonators used as a numerical examples to verify SIBC in frequency domain DG-FEM.

resonator no.	conductivity $\sigma$	edge length $l$	Q factor
1.	$5.8 \cdot 10^5 \text{S/m}$	10m	$2.32 \cdot 10^4$
2.	$5.8 \cdot 10^7 \text{S/m}$	1m	$7.34 \cdot 10^4$
3.	$5.8 \cdot 10^9 \text{S/m}$	1m	$7.34 \cdot 10^5$
4.	$5.8 \cdot 10^9 \text{S/m}$	10m	$2.32 \cdot 10^6$
5.	$5.8 \cdot 10^5 \text{S/m}$	1m	$7.34 \cdot 10^3$

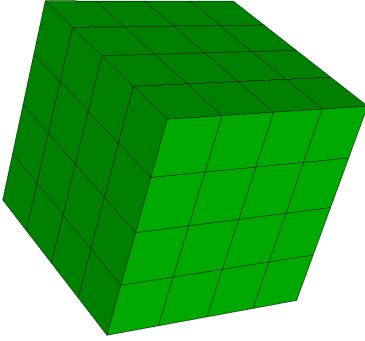


Figure 4.13: A simple hexahedral mesh used for the simulations. This mesh includes four elements/resonator edge. For the cubical cavity resonator this equals to 5.7 elements/wavelength regardless of the size of the edge length of the cubical cavity resonator.

The results obtained using the procedure described in Section 4.6 are presented in Figures 4.14 - 4.18. The figures are obtained by calculating the relative error of the  $Q$  factor with respect to the  $Q$  factor obtained by Power Loss method (4.83), see Table 4.6. The relative error  $\Delta_{\text{rel}}$  of the  $Q$  factor is defined as

$$\Delta_{\text{rel}} = \frac{|Q - Q_{\text{ref}}|}{Q_{\text{ref}}}, \quad (4.84)$$

with the reference values given in Table 4.6. The abbreviation Eigenmode DG-FEM (EMDG) in the figure titles refers to DG-FEM discretized EVP, introduced previously in Equation (4.69) in Section 4.5. Additionally, the results are compared with the results obtained by CST Eigenmode solver. The CST simulations are run with a resonator with PEC walls, and the  $Q$  factor is calculated in the post-processing phase.

The accuracy obtained is very high, with the basis function polynomial order 0 is reached relative errors of order 1%, and the smallest reached relative error for all the examples is of order  $10^{-3}\%$ . The convergence rates shown in Table 4.7 follow the  $hp$ -convergence rate [7]. Additionally, the tolerance of  $10^{-3}$  is reached after only one iteration round in all the simulations.

---

#### 4.7.2.3 CSBC Convergence Study

---

In this section, the convergence study for CSBC (Section 4.5.2) is performed. CSBC is very similar to SIBC, only the impedance function (4.25) is different to SIBC impedance function (4.19). As a test structure, a resonator with wall conductivity  $\sigma = 5.8 \cdot 10^7 \text{S/m}$  and edge length  $l = 1 \text{m}$  is used. Furthermore, the surface roughnesses  $h_{\text{RMS}} = 0.5\delta$ ,  $h_{\text{RMS}} = 1\delta$ ,  $h_{\text{RMS}} = 2\delta$  are used. The

Table 4.7.: Convergence rates for the  $Q$  factor of frequency domain DG-FEM with SIBC with respect to basis function polynomial order  $p$ .

resonator no.	$p = 0$	$p = 1$	$p = 2$	$p = 3$
1.	$h^{-2}$	$h^{-2}$	$h^{-4}$	$h^{-4}$
2.	$h^{-2}$	$h^{-2}$	$h^{-4}$	$h^{-4}$
3.	$h^{-2}$	$h^{-2}$	$h^{-4}$	$h^{-4}$
4.	$h^{-2}$	$h^{-2}$	$h^{-4}$	$h^{-4}$
5.	$h^{-2}$	$h^{-2}$	$h^{-4}$	$h^{-4}$

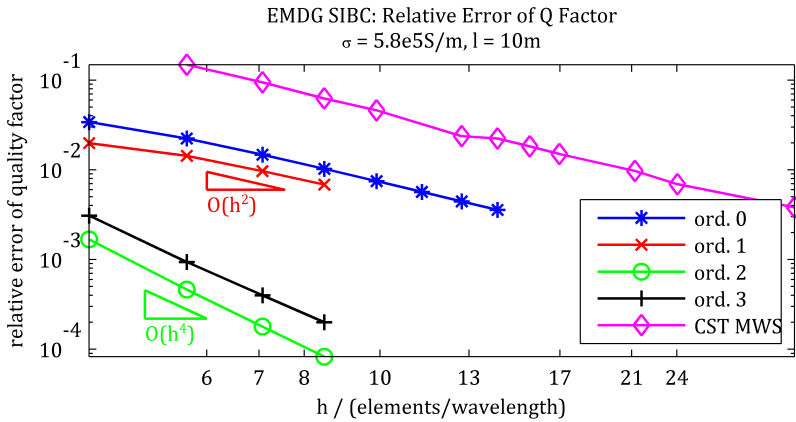


Figure 4.14.: Relative error of the  $Q$  factor of the resonator no. 1 (see Table 4.6). Orders 0-3 refer to basis function polynomial order, and the triangles indicate the convergence rate. The mesh resolution  $h$  is 4.2-14.1 elements/wavelength. The smallest reached relative error is  $8.2775 \cdot 10^{-5}$ .

skin depth  $\delta$  is calculated at the corresponding conductivity and the fundamental resonance frequency. The meshes used for the simulations are equal to the meshes used in SIBC numerical example and convergence study, see Section 4.7.2.2. The relative error  $\Delta_{\text{rel}}$  of the  $Q$  factor is defined as

$$\Delta_{\text{rel}} = \frac{|Q - Q_{\text{ref}}|}{Q_{\text{ref}}}, \quad (4.85)$$

while the reference values for the  $Q$ -factors are given in Table 4.8.



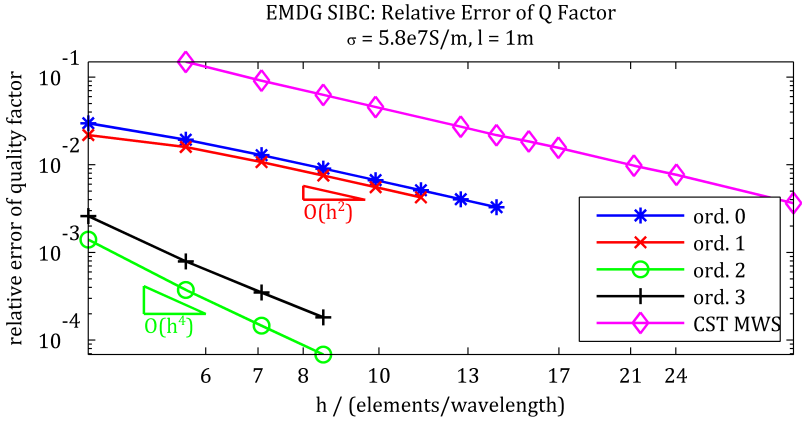


Figure 4.15.: Relative error of the Q factor of the resonator no. 2 (see Table 4.6). Orders 0-3 refer to basis function polynomial order, and the triangles indicate the convergence rate. The mesh resolution  $h$  is 4.2-14.1 elements/wavelength. The smallest reached relative error is  $6.8681 \cdot 10^{-5}$ .

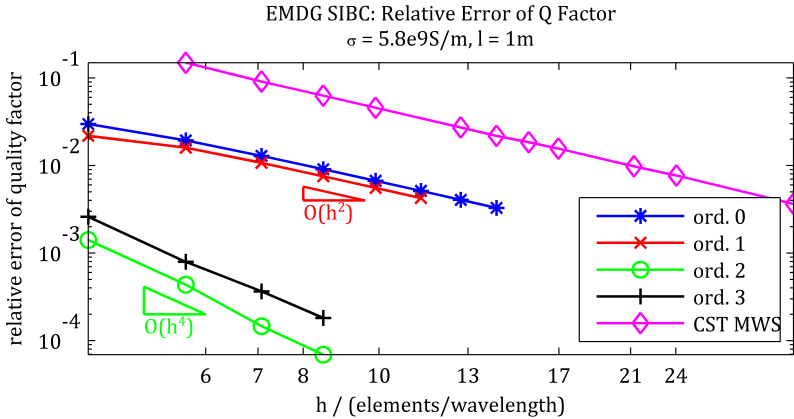


Figure 4.16.: Relative error of the Q factor of the resonator no. 3 (see Table 4.6). Orders 0-3 refer to basis function polynomial order, and the triangles indicate the convergence rate. The mesh resolution  $h$  is 4.2-14.1 elements/wavelength. The smallest reached relative error is  $6.9341 \cdot 10^{-5}$ .

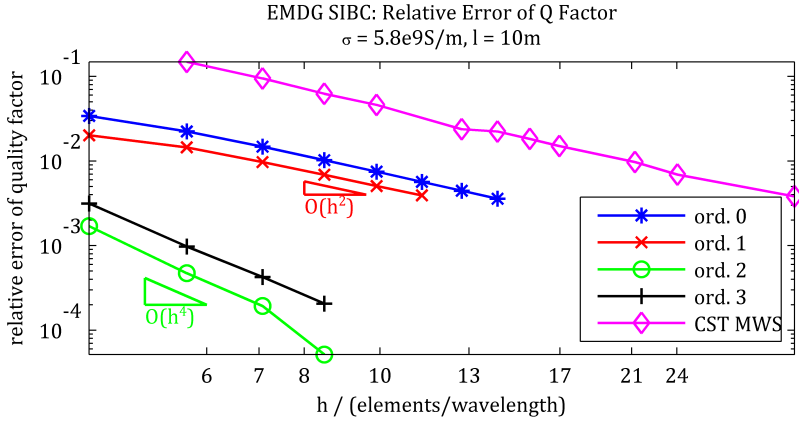


Figure 4.17.: Relative error of the Q factor of the resonator no. 4 (see Table 4.6). Orders 0-3 refer to basis function polynomial order, and the triangles indicate the convergence rate. The mesh resolution  $h$  is 4.2-14.1 elements/wavelength. The smallest reached relative error is  $5.1693 \cdot 10^{-5}$ .

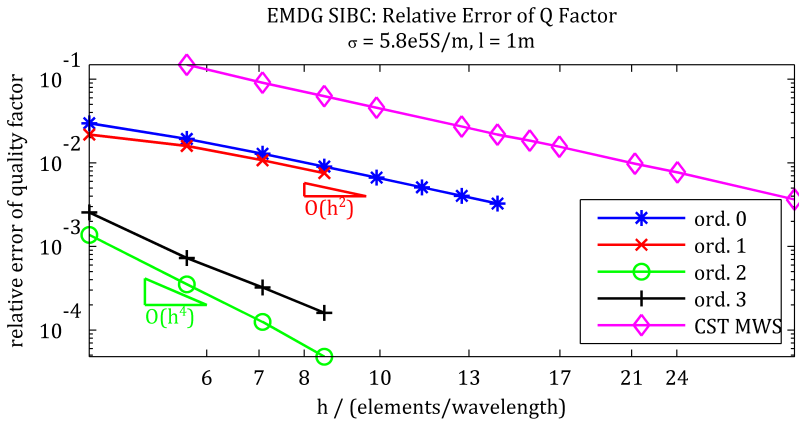


Figure 4.18.: Relative error of the Q factor of the resonator no. 5 (see Table 4.6). Orders 0-3 refer to basis function polynomial order, and the triangles indicate the convergence rate. The mesh resolution  $h$  is 4.2-14.1 elements/wavelength. The smallest reached relative error is  $4.8170 \cdot 10^{-5}$ .

Table 4.8.: CSBC cavity resonator wall roughnesses  $h_{\text{RMS}}$  with respect to the skin depth  $\delta$ , and the reference values for the  $Q$  factors.

resonator no.	$h_{\text{RMS}}/\delta$	$Q$ factor
1.	0.5	$6.05 \cdot 10^4$
2.	1	$4.58 \cdot 10^4$
3.	2	$3.89 \cdot 10^4$

The  $Q$  factors are obtained by Power Loss method (4.83) with correction in Equation (4.23) for corrugated surfaces. The results obtained using the procedure described in Section 4.6 are presented in Figures 4.19-4.21. The abbreviation EMDG in the figure titles refers to DG-FEM discretized EVP, introduced previously in Section 4.5.

The accuracy obtained is very high, with the basis function polynomial order 0 is reached accuracy of order 1%, and the smallest reached relative error for all the examples is of order  $10^{-3}\%$ . The convergence rates shown in Table 4.9 follow the  $hp$ -convergence rate [7]. Additionally, the tolerance of  $10^{-3}$  is reached after only one iteration round in all the simulations.

Table 4.9.: Convergence rates of the  $Q$  factors of frequency domain DG-FEM with CSBC, with respect to basis function polynomial order  $p$ .

resonator no.	$p = 0$	$p = 1$	$p = 2$	$p = 3$
1.	$h^{-2}$	$h^{-2}$	$h^{-4}$	$h^{-4}$
2.	$h^{-2}$	$h^{-2}$	$h^{-4}$	$h^{-4}$
3.	$h^{-2}$	$h^{-2}$	$h^{-4}$	$h^{-4}$

---

### 4.7.3 Resonator Partitioned by Thin Conductive Sheet

---

In this section, a cavity resonator partitioned by a thin conductive sheet is investigated. First, the effect of the sheet thickness on the applicability of ITBC is investigated, and a comparison with SIBC is carried out. Secondly, a convergence study of the ITBC scheme is carried out.

In Section 4.7.3.1, the validity of ITBC is investigated by increasing the thickness of the sheet, and comparing the results with SIBC. According to the theory (section 4.4), the ITBC should approach SIBC, when the thickness of the sheet increases. This is proved in the following section. In Section 4.7.3.2, the conver-

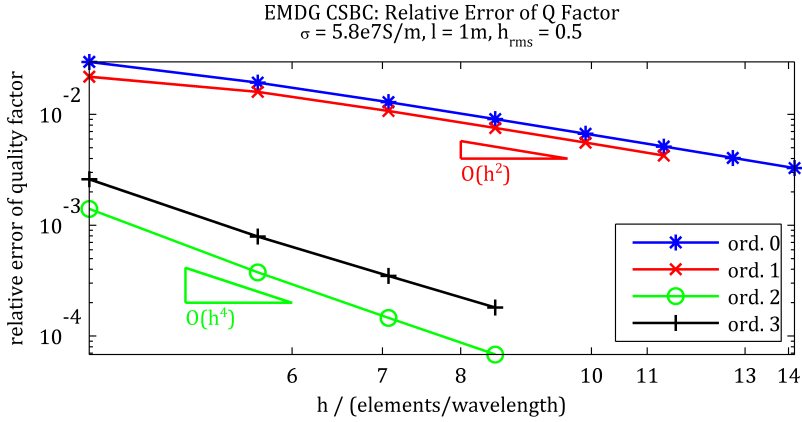


Figure 4.19.: Relative error of the Q factor of the resonator no.1 (see Table 4.8). Orders 0-3 refer to basis function polynomial order, and the triangles indicate the convergence rate. The mesh resolution  $h$  is 4.2-14.1 edges/wavelength. The smallest reached relative error is  $6.8295 \cdot 10^{-5}$ .

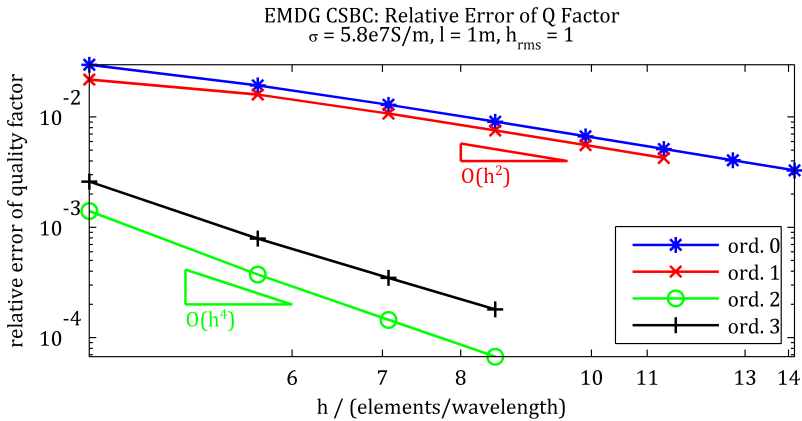


Figure 4.20.: Relative error of the Q factor of the resonator no.2 (see Table 4.8). Orders 0-3 refer to basis function polynomial order, and the triangles indicate the convergence rate. The mesh resolution  $h$  is 4.2-14.1 edges/wavelength. The smallest reached relative error is  $6.7338 \cdot 10^{-5}$ .

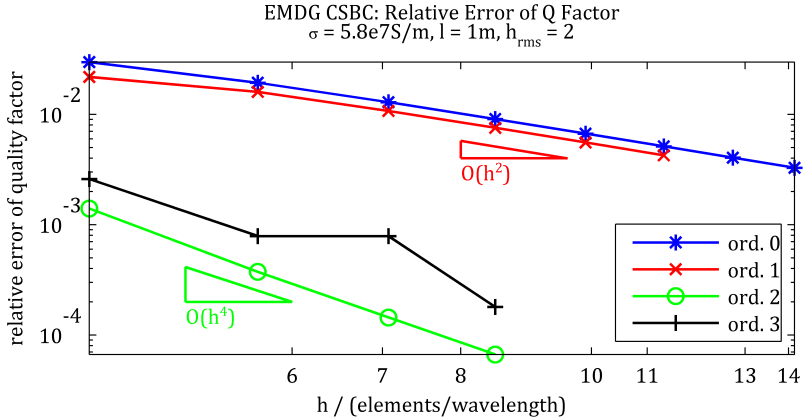


Figure 4.21.: Relative error of the Q factor of the resonator no.3 (see Table 4.8). Orders 0-3 refer to basis function polynomial order, and the triangles indicate the convergence rate. The mesh resolution  $h$  is 4.2 to 14.1 edges/wavelength. The smallest reached relative error is  $6.6674 \cdot 10^{-5}$ .

gence study of the ITBC is carried out by investigating the Q factor of resonator equipped with conductive sheets with different geometries and conductivities.

---

#### 4.7.3.1 Effect of Sheet Thickness

---

As shown in Figure 4.4 in Section 4.4, the electromagnetic field attenuates rapidly inside the conductor. The attenuation provides the limit when SIBC becomes insufficient tool to model a conductor, and one need to apply ITBC instead of SIBC. If the conductor is thinner than three skin depths, the conductor is considered transparent, and the electromagnetic field on different sides of the conductor are dependent on each other. In this case, ITBC is a suitable boundary condition. When the conductor is thicker that three skin depths, the electromagnetic field can be considered completely attenuated before it reaches the other side of the conductor. In this case, SIBC is a suitable choice as a boundary condition. The aim of this section is to verify, that when the thickness of the conductor modeled by ITBC increases, the ITBC can be replaced with SIBC. Therefore a resonator partitioned with a thin sheet with conductivity of  $1 \cdot 10^7\text{S/m}$  and with different thicknesses has been chosen as a numerical example. The thicknesses of the chosen sheets can be found in Table 4.13. The thicknesses are also calculated with respect to the skin depths of the sheets at the fundamental frequencies

of the resonators. Additionally, the attenuation of the tangential electric field component of the electromagnetic wave traveled across the corresponding sheet, according to Equation (4.26), is given in the table.

Table 4.10.: Sheet specifications, including thickness  $d$ , thickness with respect to the skin depth  $\delta$ , and the field attenuation with respect to the skin depth  $|\vec{E}(z)_t|/|\vec{E}_t(\delta)|$ , for demonstrating the effect of the sheet thickness on the suitable choice of the impedance boundary condition.

sheet no.	thickness $d$	$d/\delta$	$ \vec{E}(z)_t / \vec{E}_t(\delta) $
1.	$10\mu\text{m}$	0.9	40%
2.	$30\mu\text{m}$	2.7	6.4%
3.	$60\mu\text{m}$	5.5	0.41%
4.	$90\mu\text{m}$	8.2	0.027%
5.	$120\mu\text{m}$	11.0	0.0017%

Let us recall the impedance matrix of the ITBC model (4.57):

$$\begin{pmatrix} \vec{n} \times \vec{n} \times \vec{E}_0 \\ \vec{n} \times \vec{n} \times \vec{E}_d \end{pmatrix} = \begin{pmatrix} z_{11} & -z_{12} \\ z_{12} & -z_{11} \end{pmatrix} \begin{pmatrix} \vec{n} \times \vec{H}_0 \\ \vec{n} \times \vec{H}_d \end{pmatrix}, \quad (4.86)$$

where  $z_{11}$  and  $z_{12}$  are the impedance parameters (Equations (4.31) and (4.32)), and the subscript 0 and  $d$  indicate the different sides of the sheet. To compare the ITBC and SIBC, when the thickness of the sheet increases, the simulations are run also with a modified matrix:

$$\begin{pmatrix} \vec{n} \times \vec{n} \times \vec{E}_0 \\ \vec{n} \times \vec{n} \times \vec{E}_d \end{pmatrix} = \begin{pmatrix} Z & 0 \\ 0 & -Z \end{pmatrix} \begin{pmatrix} \vec{n} \times \vec{H}_0 \\ \vec{n} \times \vec{H}_d \end{pmatrix}, \quad (4.87)$$

where  $Z$  is the standard SIBC function (4.19). According to the theory [90], the SIBC approximation is valid, when the thickness of the sheet is three times the skin depth. In Table 4.11 and Figures 4.22 and 4.23 are presented the relative deviations of the  $Q$  factor obtained with the ITBC model, with respect to the  $Q$  factor obtained with the modified ITBC matrix given in Equation (4.87). This reference  $Q$  factor is denoted as  $Q_{\text{SIBC}}$ . The relative deviation is defined as

$$\Delta_{\text{rel.}} = \frac{|Q - Q_{\text{SIBC}}|}{Q_{\text{SIBC}}}. \quad (4.88)$$

The reference value  $Q_{\text{SIBC}}$  is calculated with mesh density 11.3 elements/wavelength and the basis function order 3.

Table 4.11.: The deviation between the ITBC and the SIBC approximations when the thickness of the sheet increases for the basis function order 0 and for the mesh resolution  $h$  17 elements/wavelength. In the table is shown the relative error of  $Q$  factor ( $\Delta_{\text{rel.}}$ ) with respect to the sheet thickness. As the theory predicts, the deviation between ITBC and SIBC gets insignificant when the sheet thickness  $d$  is greater than three skin depths.

sheet no.	$d/\delta$	$\Delta_{\text{rel.}}$
1.	0.9	700%
2.	2.7	6.3%
3.	5.5	0.14%
4.	8.2	0.16%
5.	11.0	0.13%

As can be seen, the relative deviation is significant, when the sheet thickness is greater than skin depth. However, the deviation decreases rapidly, and remains at approximately 0.1% at the thicknesses higher than 5.5 skin depths.

---

#### 4.7.3.2 ITBC Convergence Study

---

In order to verify ITBC scheme (see Section 4.4), a convergence study is performed. The test structure is a cavity resonator with edge length  $l = 1\text{m}$ , and with perfectly conducting (PEC) walls. Additionally, the resonator is partitioned into two with a thin, conductive sheet, on which the ITBC is applied. Three different thin sheets are chosen, with the specifications given in Table 4.12.

Table 4.12.: Conductivities and thicknesses of the thin sheets used in ITBC simulations. Thicknesses are given in terms of absolute thickness  $\delta$ , as well as with respect to the skin depth  $d$ .

sheet no.	conductivity $\sigma$	thickness $d$	$d/\delta$
1.	$10^7\text{S/m}$	$10\mu\text{m}$	0.9
2.	$10^7\text{S/m}$	$30\mu\text{m}$	2.7
3.	$10^7\text{S/m}$	$60\mu\text{m}$	5.5

---

Deviation between ITBC and SIBC: Basis Function Order 0  
 Relative Deviation of Q factor w.r.t. Sheet Thickness

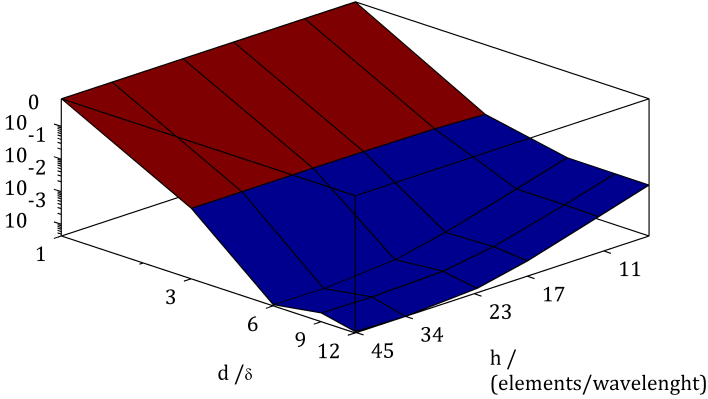


Figure 4.22.: The deviation between the ITBC and the SIBC approximations when the thickness of the sheet increases. The basis function order for the ITBC simulations is 0. The relative error of Q factor ( $\Delta_{\text{rel.}}$ , z-axis) is plotted with respect to the mesh resolution  $h$  (in elements/wavelength, x-axis) and the sheet thickness  $d$  (in skin depths  $\delta$ , y-axis). As the theory predicts, the deviation between ITBC and SIBC gets insignificant when the sheet thickness  $d$  is greater than three skin depths. The quantitative analysis of the deviation is given in Table 4.11.

The conductivity of all the sheets is the same  $\sigma = 1 \cdot 10^7 \text{S/m}$ , while the thicknesses vary from  $10 \mu\text{m}$  to  $60 \mu\text{m}$ , which correspond to 0.9 to 5.5 skin depths at the fundamental frequency  $f_0$  of the resonator (see Table 4.13). The mesh for the ITBC simulations is a simple hexahedral mesh, but unlike with SIBC and CSBC meshes (Figure 4.13), the mesh elements are not cubical. Due to the presence of the sheet, the field variation in the direction of normal to the sheet is much greater than in other two directions, and therefore the mesh density is twice as fine in normal direction. See an exemplary mesh in Figure 4.24. The basis function polynomial orders are chosen to be 0, 1, and 2.

The results obtained using the procedure described earlier are presented in Figures 4.25-4.30. The abbreviation EMDG in the figure titles refers to DG-FEM discretized EVP, introduced previously in Section 4.5. In this numerical example also the fundamental resonance frequency  $f_0$  is investigated. The figures are obtained by calculating the relative errors of the fundamental frequency  $f_0$  and the corresponding Q factor with respect to the results obtained by simu-



Deviation between ITBC and SIBC: Basis Function Order 1  
Relative Deviation of Q factor w.r.t. Sheet Thickness

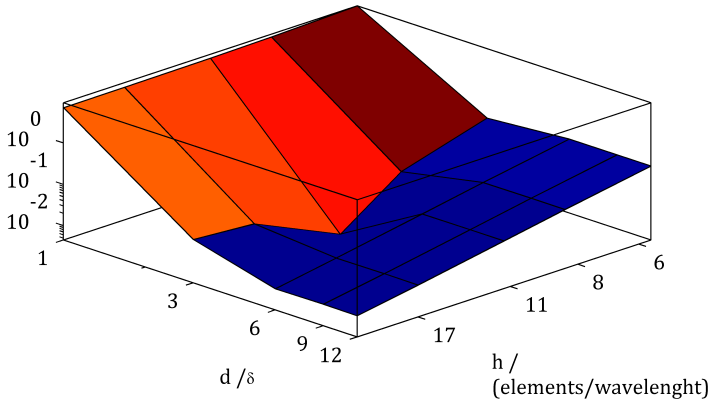


Figure 4.23.: The deviation between the ITBC and the SIBC approximations when the thickness of the sheet increases. The basis function order for the ITBC simulations is 1. The relative error of  $Q$  factor ( $z$ -axis) is plotted with respect to the mesh resolution  $h$  (in elements/wavelength,  $x$ -axis) and the sheet thickness  $d$  (in skin depths  $\delta$ ,  $y$ -axis). As the theory predicts, the deviation between ITBC and SIBC gets insignificant when the sheet thickness  $d$  is greater than three skin depths.

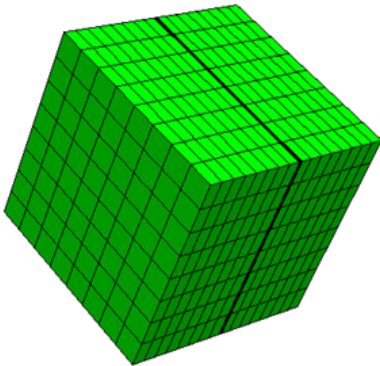


Figure 4.24.: A simple hexahedral mesh used for the ITBC simulations. This mesh includes eight elements/resonator edge in two directions, and 16 elements in the direction normal to the sheet. To emphasize the location of the sheet, it is denoted with a thick solid line. Nevertheless, the sheet is replaced only with a normal element interface, as described in section 4.4.

lations with basis function polynomial order 3 and the mesh resolution  $h$  11.3

elements/wavelength. The reference values are given in Table 4.13. The relative errors  $\Delta_{Q, \text{rel.}}$  and  $\Delta_{f, \text{rel.}}$  are defined as

$$\Delta_{Q, \text{rel.}} = \frac{|Q - Q_{\text{ref.}}|}{Q_{\text{ref.}}}, \text{ and } \Delta_{f, \text{rel.}} = \frac{|f_0 - f_{\text{ref.}}|}{f_{\text{ref.}}}. \quad (4.89)$$

Table 4.13.: Reference values of resonance frequencies  $f_0$  and  $Q$  factors used in ITBC convergence study.

resonator no.	$f_0$	$Q$ factor
1.	0.21198GHz	$3.68 \cdot 10^4$
2.	0.21198GHz	$4.28 \cdot 10^4$
3.	0.21198GHz	$4.57 \cdot 10^4$

The accuracy obtained is very high, with the basis function polynomial order 0 is reached accuracy of order  $1 \cdot 10^{-2}\%$  for the  $Q$  factor and  $1 \cdot 10^{-5}\%$  for the resonance frequency. The convergence rates shown in Table 4.14 follow the  $hp$ -convergence rate [7]. Additionally, the tolerance of  $10^{-3}$  is reached after only one iteration round in all the simulations.

Table 4.14.: Convergence rates of the  $Q$  factors and the resonance frequencies  $f_0$  of frequency domain DG-FEM with ITBC with respect to the basis function polynomial order  $p$ .

resonator no.	p = 0		p = 1		p = 2	
	$f_0$	$Q$	$f_0$	$Q$	$f_0$	$Q$
1.	$h^{-2}$	$h^{-2}$	$h^{-3}$	$h^{-2}$	$h^{-7}$	$h^{-3}$
2.	$h^{-2}$	$h^{-5}$	$h^{-3}$	$h^{-2}$	$h^{-7}$	$h^{-3}$
3.	$h^{-2}$	$h^{-3}$	$h^{-3}$	$h^{-2}$	$h^{-7}$	$h^{-3}$

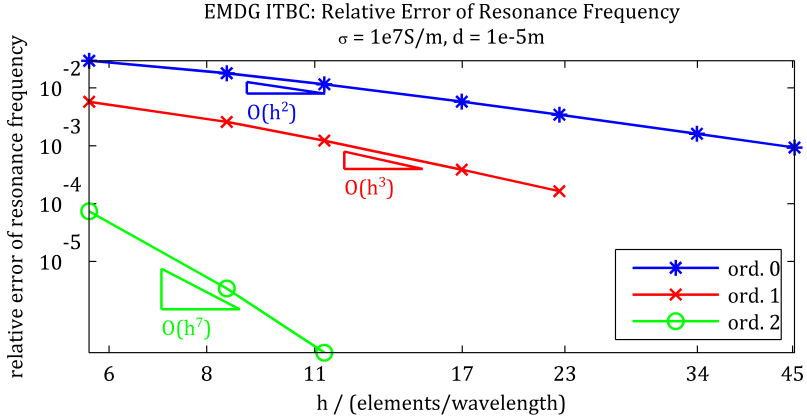


Figure 4.25.: Relative error of the fundamental frequency of a resonator partitioned by a sheet no. 1 (Table 4.12). Orders 0-2 refer to basis function polynomial order, and the triangles indicate the convergence rate. The mesh resolution  $h$  is 5.6-45.2 edges/wavelength in direction of normal to the sheet (see Figure 4.24). The smallest reached relative error is  $2.3 \cdot 10^{-5}$ .

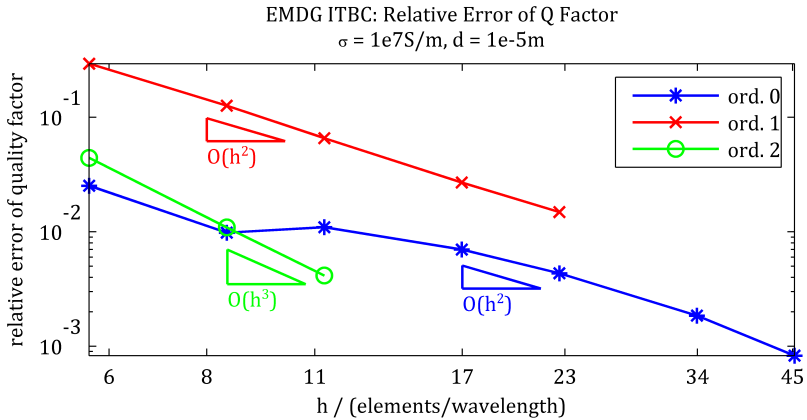


Figure 4.26.: Relative error of the Q factor of a resonator partitioned by a sheet no. 1 (Table 4.12). Orders 0-2 refer to basis function polynomial order, and the triangles indicate the convergence rate. The mesh resolution  $h$  is 5.6-45.2 edges/wavelength in direction of normal to the sheet (see Figure 4.24). The smallest reached relative error is  $8.3 \cdot 10^{-4}$ .

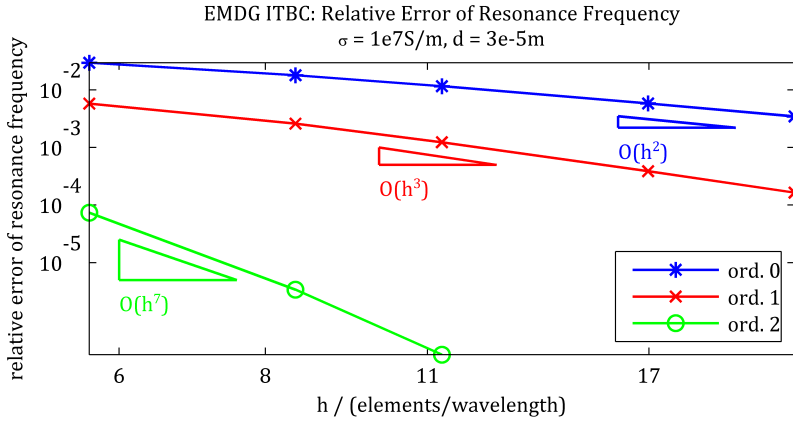


Figure 4.27.: Relative error of the fundamental frequency of a resonator partitioned by a sheet no. 2 (Table 4.12). Orders 0-2 refer to basis function polynomial order, and the triangles indicate the convergence rate. The mesh resolution  $h$  is 5.6-45.2 edges/wavelength in direction of normal to the sheet (see Figure 4.24). The smallest reached relative error is  $2.4 \cdot 10^{-5}$ .

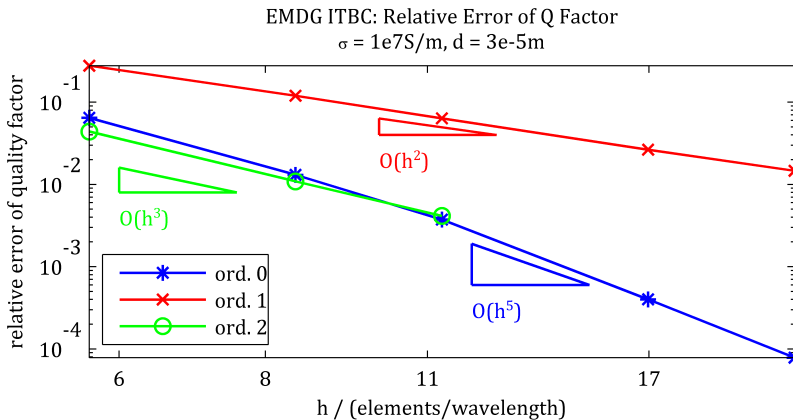


Figure 4.28.: Relative error of the Q factor of a resonator partitioned by a sheet no. 2 (Table 4.12). Orders 0-2 refer to basis function polynomial order, and the triangles indicate the convergence rate. The mesh resolution  $h$  is 5.6-45.2 edges/wavelength in direction of normal to the sheet (see Figure 4.24). The smallest reached relative error is  $7.9 \cdot 10^{-5}$ .

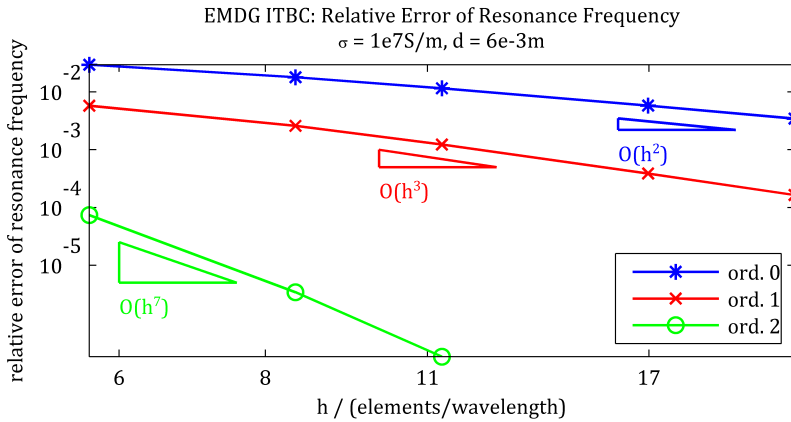


Figure 4.29.: Relative error of the fundamental frequency of a resonator partitioned by a sheet no. 3 (Table 4.12). Orders 0-2 refer to basis function polynomial order, and the triangles indicate the convergence rate. The mesh resolution  $h$  is 5.6-45.2 edges/wavelength in direction of normal to the sheet (see Figure 4.24). The smallest reached relative error is  $2.4 \cdot 10^{-7}$ .

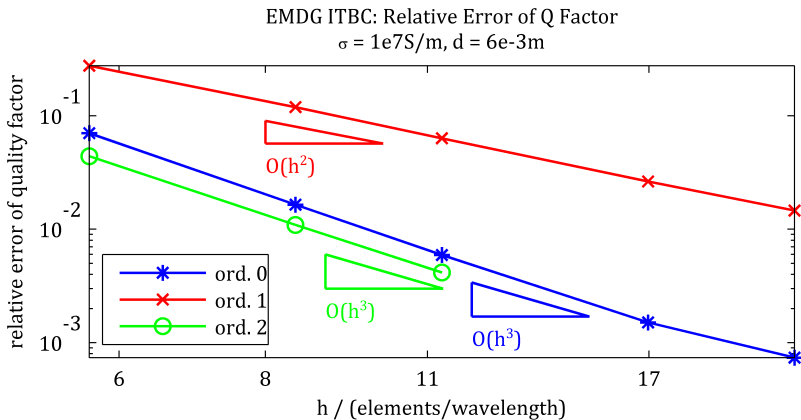


Figure 4.30.: Relative error of the Q factor of a resonator partitioned by a sheet no. 3 (see Table 4.12). Orders 0-2 refer to basis function polynomial order, and the triangles indicate the convergence rate. The mesh resolution  $h$  is 5.6-45.2 edges/wavelength in direction of normal to the sheet (see Figure 4.24). The smallest reached relative error is  $5.3 \cdot 10^{-4}$ .

---

## 5 Dispersive Boundary Conditions in Time Domain

In the previous chapter, the dispersive impedance boundary conditions were introduced, and the implementation for frequency domain DG-FEM was proposed. Additionally, a scheme to take the dispersivity of the impedance boundary conditions on a wide frequency band into account in frequency domain simulations, was proposed.

In this chapter, the dispersive impedance boundary conditions are considered in time domain simulations. The dispersive impedance functions are approximated in the frequency domain, and then transformed into the time domain. The transformation is discretized in time, exploiting two known methods, RC and ADE methods. Finally, an implementation for time domain DG-FEM is proposed, and the proposed schemes are verified by numerical examples and convergence studies. Additionally, the RC and ADE approaches are compared in terms of accuracy and simulation times.

---

### 5.1 Introduction

---

Modeling dispersive phenomena, like surface impedance boundary conditions, in the frequency domain is often straightforward, and the simulation times are typically short. However, the major disadvantage of frequency domain simulations is that they are, in general, only capable to solve for a single frequency at one simulation.

In contrast, in the Time Domain (TD), it is possible to solve for several frequencies at a single simulation run. Additionally, modeling of transient signals is only possible in the time domain, as the transient signal consists of several frequencies. However, modeling of dispersive phenomena requires special treatment in the time domain, while being trivial in the frequency domain. Time domain modeling can also be time-consuming compared to frequency domain modeling. The boundary conditions presented previously in Chapter 4, are all frequency dependent, i.e. dispersive. In this chapter, two different approaches to model these dispersive boundary conditions in the time domain are described, namely

---

RC and ADE methods. Additionally, an implementation of these methods to DG-FEM is presented. The ADE scheme for modeling surface impedance boundary conditions is partly published by the author in [98].

As in Chapter 4, the plot of this chapter is to find a numerical solution for the source-free Maxwell's equations in a computational domain  $\Omega$ , now in the time domain:

$$\left\{ \begin{array}{ll} \nabla \times \vec{E} = -\frac{\partial \vec{B}}{\partial t} & \text{in } \Omega \\ \nabla \times \vec{H} = \frac{\partial \vec{D}}{\partial t} & \text{in } \Omega \\ \vec{n} \times \vec{n} \times \vec{E} = f(\omega)(\vec{n} \times \vec{H}) & \text{on } \partial\Omega. \end{array} \right. \quad (5.1)$$

The boundary condition  $\vec{n} \times \vec{n} \times \vec{E} = f(\omega)(\vec{n} \times \vec{H})$  connects the tangential electric field with the tangential magnetic field, on the boundary surrounding the conductor excluded from the computational domain.

The procedure for modeling dispersive boundary conditions, and consequently also the coarse outline of this chapter, is the following:

- Approximate the dispersive boundary condition function in the frequency domain (Section 5.2)
- Transform the approximation into the time domain (Section 5.3)
- Discretize the transformed approximation in time (Sections 5.3.3, 5.3.4)
- Integrate the transformation to the Maxwell's equations (Section 5.4)

After these steps, numerical examples and convergence studies are presented in Section 5.5, in order to verify and validate the obtained schemes.

---

### 5.1.1 Significance of Dispersivity in TD Simulations

---

As an introduction to modeling dispersive impedance boundary conditions, the importance of considering the dispersivity of the impedance functions in time domain modeling, is pointed out in this section. Figure 5.1(a) shows a time signal of a lossless cubical cavity resonator. The signal is a sum of the five lowest resonance frequencies of a resonator, as can be seen in Figure 5.1(b), which shows the spectrum of the signal.

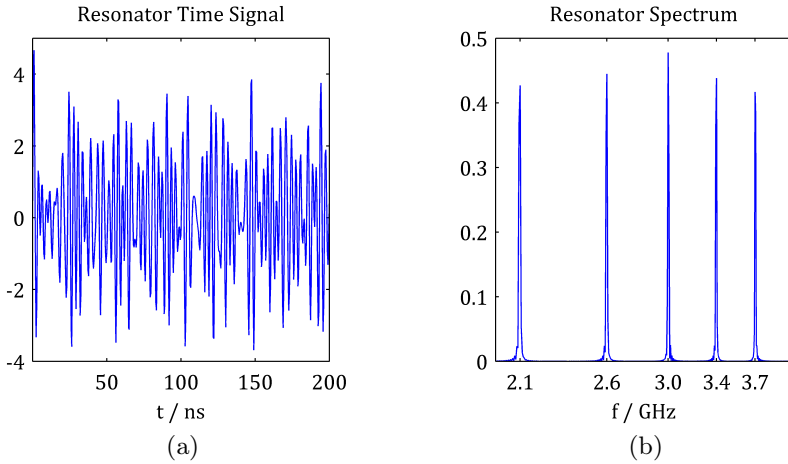


Figure 5.1.: The time signal (a) of a lossless cubical cavity resonator, and the spectrum of the signal (b).

The impedance function (4.19) gets significantly different values at the different resonance frequencies. The resonance frequencies, the real parts of the impedance function values at the resonance frequencies, as well as the relative deviations of the impedances with respect to the impedance at the fundamental frequency are summarized in Table 5.1.

Table 5.1.: Resonance frequencies, respective real parts of the impedance function values and their relative differences with respect to the impedance value at the fundamental frequency  $f_0$ .

$i$	resonance frequency $f_i$	impedance $Z(f_i)$	$ Z(f_i) - Z(f_0) /Z(f_0)$
0	0.21199GHz	100m $\Omega$	—
1	0.25963GHz	112m $\Omega$	10.7%
2	0.29979GHz	119m $\Omega$	18.9%
3	0.33518GHz	127m $\Omega$	25.7%
4	0.36717GHz	133m $\Omega$	31.6%

The difference of the impedance values at the fundamental and the fifth resonance frequencies is as high as 31.6%. A constant approximation of the impedance



function would lead to inaccurate results, and it is therefore highly important to take the frequency dependency into account in the time domain simulations.

---

## 5.2 Rational Approximation of Impedance Functions in FD

---

The first step to model the dispersive impedance functions in the time domain, is to approximate the functions in the frequency domain. In this thesis, this is done by the vector fitting procedure [39], [38], [22]. The vector fitting package is available for downloading at the VECTFIT website [37]. The idea is to fit a complex function as a sum of rational functions, and the details of the fitting procedure can be found in the aforementioned references. In this section, the fitting procedure is applied to the impedance boundary condition function. Let the impedance function to be fitted be  $Z(\omega)$  and the approximation obtained by vector fitting  $Z_{\text{VF}}(\omega)$ . The approximation can be written as:

$$Z(\omega) \approx Z_{\text{VF}}(\omega) = \sum_{i=1}^P \frac{c_i}{j\omega - a_i}, \quad (5.2)$$

where  $P$  is the number of interpolants, and  $a_i$ ,  $c_i$  real fitting parameters. The first order rational functions in (5.2) correspond to the Drude model [24] of dispersive medium.

The approximation  $Z_{\text{VF}}(\omega)$  is a compromise between accuracy, computational cost of the time domain simulation, and the width of the frequency band. In this section a rationale for the choices made to obtain the optimal approximation is given. A high number  $P$  of interpolants leads to a high accuracy over a wide frequency band. However, the cost of the accuracy is a higher computational cost in time domain simulations. To give an idea of the compromise, the SIBC impedance function (4.19) is fitted:

$$Z(\omega) = \sqrt{\frac{j\omega\varepsilon}{\sigma + j\omega\mu}} \quad (5.3)$$

with the following material parameters: Conductivity  $\sigma = 5.8 \cdot 10^5 \text{S/m}$ , permittivity  $\varepsilon = \varepsilon_0$  and permeability  $\mu = \mu_0$ . The fitting with two different numbers of interpolants is performed:  $P = 5$  and  $P = 10$ , as well as with two different frequency bands,  $\Delta\omega = 10^7 \dots 10^{10} 1/\text{s}$  and  $\Delta\omega = 10^6 \dots 10^{11} 1/\text{s}$ . This means, a low and high number of interpolants, and wide and narrow frequency band, as well as combinations of these. Consequently, four different impedance approximations are obtained for the impedance function (4.19):

$$Z_{VF1}(\omega) = \sum_{i=1}^5 \frac{c_{i1}}{j\omega - a_{i1}}, \quad 10^7 1/s < \omega < 10^{10} 1/s, \quad (5.4)$$

$$Z_{VF2}(\omega) = \sum_{i=1}^{10} \frac{c_{i2}}{j\omega - a_{i2}}, \quad 10^7 1/s < \omega < 10^{10} 1/s \quad (5.5)$$

$$Z_{VF3}(\omega) = \sum_{i=1}^5 \frac{c_{i3}}{j\omega - a_{i3}}, \quad 10^6 1/s < \omega < 10^{11} 1/s, \quad (5.6)$$

$$Z_{VF4}(\omega) = \sum_{i=1}^{10} \frac{c_{i4}}{j\omega - a_{i4}}, \quad 10^6 1/s < \omega < 10^{11} 1/s, \quad (5.7)$$

with the fitting parameters  $a_{1i}$ ,  $a_{2i}$ ,  $a_{3i}$ ,  $a_{4i}$  and  $c_{1i}$ ,  $c_{2i}$ ,  $c_{3i}$ ,  $c_{4i}$  given in Tables A.1, A.2, A.3, and A.4 in Appendix A. These fittings are used in convergence studies in Section 5.5. The relative deviation  $\Delta_{\text{rel.}}$ , the maximum value of the deviation  $\Delta_{\text{max}}$ , and Coefficient of Variation (CV) for the real parts of the approximations are defined as follows:

$$\Delta_{\text{rel.},i} = \frac{|\text{Re}\{Z_i(\omega)\} - \text{Re}\{Z_{VF,i}(\omega)\}|}{\text{Re}\{Z_i(\omega)\}} \quad (5.8)$$

$$\Delta_{\text{max}} = \max(\Delta_{\text{rel.}}) \quad (5.9)$$

$$\Delta_{\text{CV}} = \frac{\Delta_{\text{RMS}}}{\text{Re}\{Z(\omega)\}}, \quad (5.10)$$

with RMS deviation

$$\Delta_{\text{RMS}} = \sqrt{\frac{\sum_{i=1}^N [\text{Re}\{Z_i(\omega)\} - \text{Re}\{Z_{VF,i}(\omega)\}]^2}{N}}, \quad (5.11)$$

where  $Z_i$  and  $Z_{VF,i}$  are the impedance function values evaluated at frequency point  $i$ , and  $N$  is the number of frequency points of the approximation (in this case  $N = 1000$ ). The mean value of the impedance function  $Z(\omega)$  is denoted as  $\overline{Z(\omega)}$ . The deviations of imaginary parts are defined respectively.

The real parts of the impedance approximations  $Z_{VF1}(\omega) - Z_{VF4}(\omega)$ , as well as their relative deviations with respect to analytic impedance function (4.19)

are shown in Figure 5.2. The imaginary parts and the deviations are presented respectively in Figure 5.3.

The maximum relative deviations (5.9) and the CV deviations (5.10) of the impedance approximation  $Z_{VF1}(\omega) - Z_{VF4}(\omega)$  are presented in Tables 5.2 and 5.3.

Table 5.2.: Maximum relative deviations  $\Delta_{\max}$  and CV deviations  $\Delta_{CV}$  of the real parts of the impedance approximations  $Z_{VF1}(\omega) - Z_{VF4}(\omega)$ .

	$\Delta_{\max}$	$\omega(\Delta_{\max})$	$\Delta_{CV}$
$Z_{VF1}$	2600%	$1 \cdot 10^{10}1/s$	16%
$Z_{VF2}$	140%	$1 \cdot 10^{10}1/s$	0.7%
$Z_{VF3}$	30000%	$1 \cdot 10^{11}1/s$	240%
$Z_{VF4}$	25000%	$1 \cdot 10^{11}1/s$	220%

Table 5.3.: Maximum relative deviations  $\Delta_{\max}$  and CV deviations  $\Delta_{CV}$  of the imaginary parts of the impedance approximations  $Z_{VF1}(\omega) - Z_{VF4}(\omega)$ .

	$\Delta_{\max}$	$\omega(\Delta_{\max})$	$\Delta_{CV}$
$Z_{VF1}$	3500%	$1 \cdot 10^71/s$	9.8%
$Z_{VF2}$	240%	$1 \cdot 10^71/s$	1.2%
$Z_{VF3}$	16000%	$6 \cdot 10^{10}1/s$	170%
$Z_{VF4}$	18000%	$1 \cdot 10^{11}1/s$	180%

As can be seen in Figures 5.2, 5.3, and Tables 5.2, 5.3, the approximation gets more accurate when the number of interpolants  $P$  increases, and when the frequency band  $\Delta\omega$  gets narrower. However, the maximum values of the relative deviation  $\Delta_{\text{rel}}$  are at maximum in the extremities of the frequency band, as can be seen in Tables 5.2 and 5.3. In contrast, in the middle of the frequency band, the relative deviation is very small, see Figures 5.2 and 5.3. When the lack of accuracy of the approximations in the extremities of the frequency band is considered, the obtained accuracy of the approximation is very high.

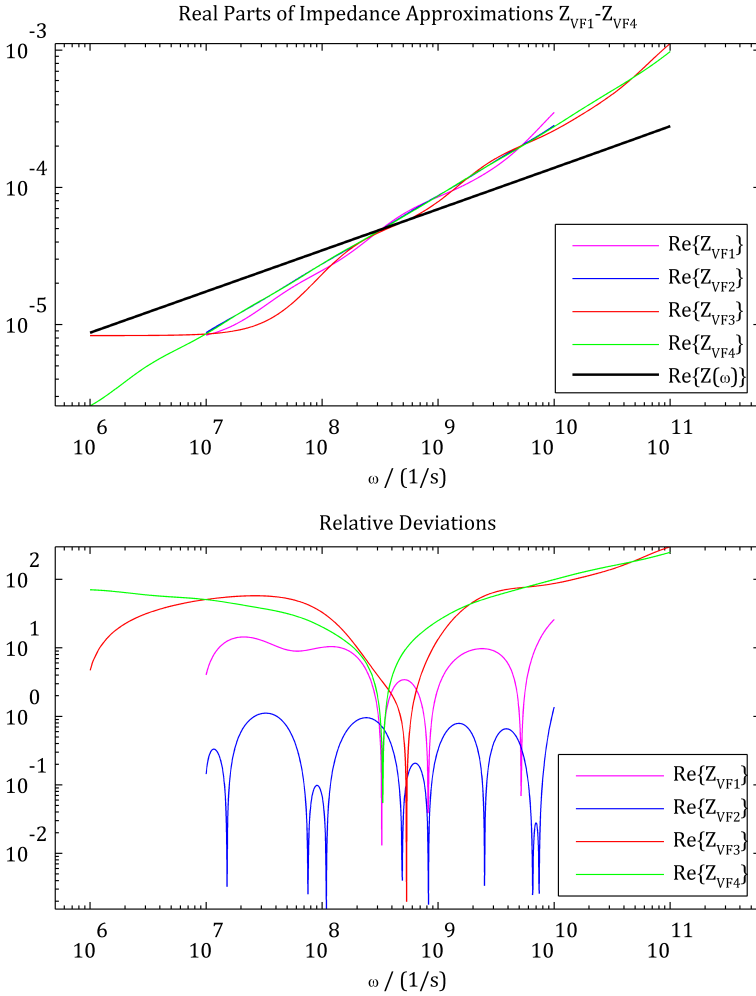


Figure 5.2.: The real parts of the analytic impedance function  $Z(\omega)$  and vector fitting approximations  $Z_{VF1}(\omega)-Z_{VF4}(\omega)$  are shown in the upper figure. The lower figure shows the relative deviations of the approximations with respect to the analytic impedance function  $\text{Re}\{Z(\omega)\}$ .

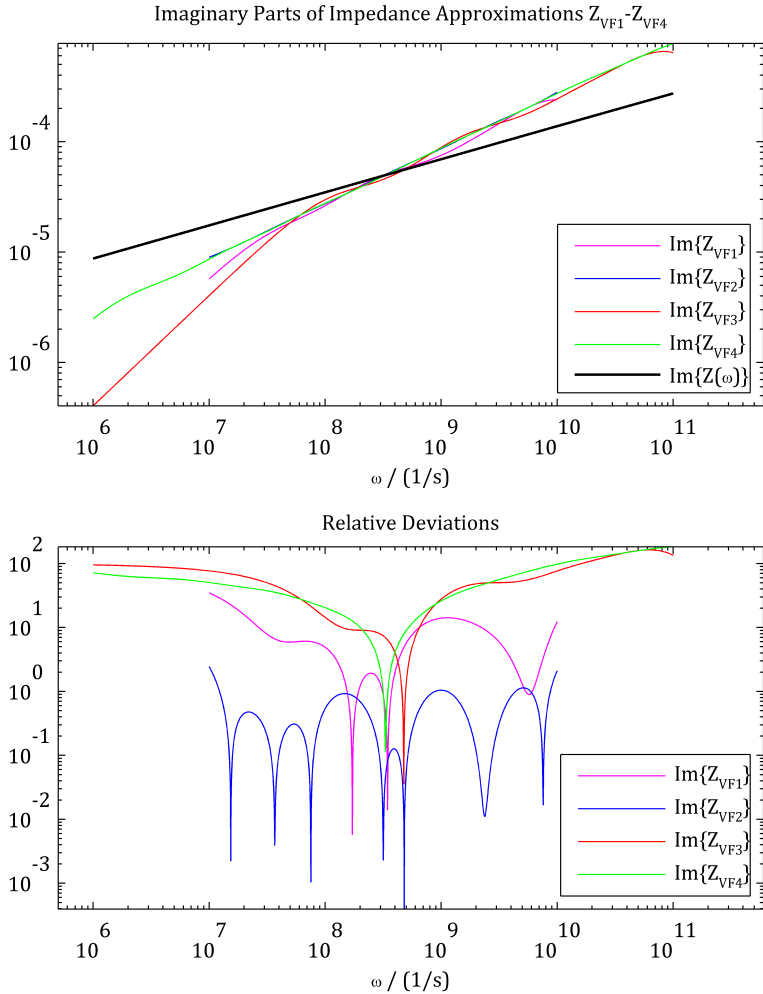


Figure 5.3.: The imaginary parts of the analytic impedance function  $Z(\omega)$  and vector fitting approximations  $Z_{VF1}(\omega)-Z_{VF4}(\omega)$  are shown in the upper figure. The lower figure shows the relative deviations of the approximations with respect to the analytic impedance function  $\text{Im}\{Z(\omega)\}$ .

---

## 5.3 Transform from FD into TD

---

In this section is explained how the dispersive impedance boundary conditions are approximated and transformed into the frequency domain. At first, some prerequisites and properties of the transform are introduced.

---

### 5.3.1 Linearity and Causality of a Physical System

---

Let us assume a deterministic system described by an input function  $I$ , output function  $O$ , and the response function  $R$ , which are connected via the following equation [80]:

$$O = R\{I\}. \quad (5.12)$$

Let us define some prerequisites for a physical system, which we require to be fulfilled within this thesis.

- (1) A system described by equation (5.12) is linear, if for two inputs,  $I_1$  and  $I_2$  and two outputs,  $O_1$  and  $O_2$ , the following equation applies [80]:

$$R\{\alpha I_1 + \beta I_2\} = \alpha O_1 + \beta O_2. \quad (5.13)$$

- (2) A system is required to be causal, i.e. an input at time instance  $t$  should not produce an output earlier than  $t$ , and that two equal inputs can only produce equal outputs [80], [72], i.e.:

$$R(t) = 0 \text{ for } t < 0. \quad (5.14)$$

and

$$I_1 = I_2 \Rightarrow O_1 = O_2. \quad (5.15)$$

- (3) A physical system requires that a real input have to produce a real output. Consequently the response function must be real for all real values of  $t$ . However, input and output do not have to be real themselves [80].
- (4) A finite output for a physical system has to cause a finite output which decreases monotonically over time [80].

---

### 5.3.2 Laplace Transform

---

Laplace transform is an integral transform of a function  $f(t)$  with a real argument  $t$ , that transforms  $f(t)$  into a function  $F(s)$  with a complex argument  $s = j\omega$ . The Laplace transform is defined as [19]:

$$F(s) = \mathcal{L}\{f(t)\} = \int_{-\infty}^{\infty} f(t)e^{-st} dt, \quad \text{Re}\{s\} > \alpha, \quad (5.16)$$

and it's inverse as [19]:

$$f(t) = \mathcal{L}^{-1}\{F(s)\} = \frac{1}{2\pi j} \int_{c-j\infty}^{c+j\infty} F(s)e^{st} ds, \quad c > \alpha, \quad (5.17)$$

where  $\alpha$  is the abscissa of the convergence<sup>1</sup>. There are two important properties of Laplace transform [19], which are very useful in this work. First, the Laplace transform is a linear operator (5.13), i.e. for two functions,  $f(t)$  and  $g(t)$ , with their Laplace transforms  $F(s)$  and  $G(s)$  holds

$$\mathcal{L}\{af(t) + bg(t)\} = aF(s) + bG(s), \quad (5.18)$$

where  $a$  and  $b$  are arbitrary constants. Second important property of the Laplace transform is, that the Laplace transform of the convolution of two functions  $f(t)$  and  $g(t)$  with real arguments, is a multiplication:

$$\mathcal{L}\{f(t) * g(t)\} = F(s)G(s), \quad (5.19)$$

where  $*$  is the convolution operation, defined as

$$f(t) * g(t) = \int_0^{\infty} f(t)g(t - \tau)d\tau. \quad (5.20)$$

---

<sup>1</sup> The function  $F(s)$  is analytic in the half-plane  $\text{Re}\{s\} > \alpha$ .

---

### 5.3.3 Recursive Convolution (RC)

---

In this section, Oh's [71] approach to model the dispersive boundary conditions in the time domain, using recursive convolution, is introduced. Let us begin with the standard SIBC approach, introduced in Section 4.2.1. Denoting the tangential magnetic field on the surface  $\vec{n} \times \vec{H}$  as  $\vec{H}_t$ , and the tangential electric field  $\vec{n} \times \vec{n} \times \vec{E}$  as  $\vec{E}_t$ , the relation between them (4.20) can be written in the frequency domain as

$$\vec{E}_t(\omega) = Z(\omega)\vec{H}_t(\omega). \quad (5.21)$$

According to Equation (5.19), Equation (5.21) can be written as a convolution integral in the time domain:

$$\vec{E}_t(t) = Z(t) * \vec{H}_t(t) = \int_{-\infty}^{\infty} Z(t - \tau)\vec{H}_t(\tau)d\tau. \quad (5.22)$$

Let us recall the impedance function rational approximation in the frequency domain obtained by vector fitting procedure (5.2):

$$Z(\omega) \approx \sum_{i=1}^P \frac{c_i}{j\omega - a_i}, \quad (5.23)$$

where  $P$  is the number of rational interpolants, and  $a_i$ ,  $c_i$  are real fitting parameters. Taking the inverse Laplace transform (5.17) of  $i^{\text{th}}$  rational interpolant (5.23) leads into:

$$\mathcal{L}^{-1} \left\{ \frac{c_i}{j\omega - a_i} \right\} = c_i e^{a_i t} u(t), \quad (5.24)$$

with the Heaviside step function  $u(t)$ :

$$u(t) = \begin{cases} 0, & t < 0 \\ 1, & t \geq 0. \end{cases} \quad (5.25)$$

The Heaviside step function can be dropped out, as we are only interested in the region  $t \geq 0$ . Taking into account all the interpolants, the impedance function in the time domain can be written as:



$$Z(t) = \sum_{i=1}^P c_i e^{a_i t}, \quad t \geq 0. \quad (5.26)$$

Inserting the impedance function in the time domain (5.26) into the convolution integral (5.19) leads to

$$\vec{E}_t(t) = Z(t) * \vec{H}_t(t) = \sum_{i=1}^P \int_0^{\infty} c_i e^{a_i(t-\tau)} \vec{H}_t(\tau) d\tau. \quad (5.27)$$

In the discrete time domain, assuming piecewise linear magnetic field  $\vec{H}_t$ , the electric field at the time step  $\Delta t$ , i.e.  $\vec{E}_t(n\Delta t) = \vec{E}_t^n$ , is given as

$$\vec{E}_t^n = \sum_{i=1}^P \sum_{m=0}^n \int_{(m-1)\Delta t}^{m\Delta t} e^{-\omega_i(n\Delta t - \tau)} \left[ \vec{H}_t^{m-1} + (\tau - (m-1)\Delta t) \frac{\vec{H}_t^m - \vec{H}_t^{m-1}}{\Delta t} \right] d\tau. \quad (5.28)$$

Next, the integration is carried out over  $\tau$ . Then, the  $n^{\text{th}}$  term is taken out of the sum, and the remainings are written in terms of  $\vec{E}_t^{n-1}$  and  $\vec{H}_t^{n-1}$ . Eventually the following equation can be written for the electric field  $\vec{E}_t^n$  in terms of an auxiliary variable  $\mathcal{R}^i$ :

$$\vec{E}_t^n = \sum_{i=1}^P \left( \zeta_{1i}^R \vec{H}_t^n + \zeta_{2i}^R \vec{H}_t^{n-1} + \zeta_{3i}^R \mathcal{R}_i^{n-1} \right), \quad (5.29)$$

with coefficients

$$\zeta_{1i}^R = \frac{c_i}{a_i} \left[ 1 + \frac{1}{\Delta t a_i} (e^{-a_i \Delta t} - 1) \right] \quad (5.30)$$

$$\zeta_{2i}^R = \frac{c_i}{a_i} \left[ \frac{1}{\Delta t a_i} - e^{-a_i \Delta t} \left( 1 + \frac{1}{\Delta t a_i} \right) \right] \quad (5.31)$$

$$\zeta_{3i}^R = \frac{c_i}{a_i} e^{-a_i \Delta t}. \quad (5.32)$$

The details of the derivation can be found in [71]. The impedance boundary condition in Equation (5.21) can now be approximated in the discrete time domain as:

$$\begin{cases} \vec{E}_t^n = \sum_{i=1}^P \vec{\mathcal{R}}_i^n \\ \vec{\mathcal{R}}_i^n = \zeta_{1i}^R \vec{H}_t^n + \zeta_{2i}^R \vec{H}_t^{n-1} + \zeta_{3i}^R \vec{\mathcal{R}}_i^{n-1}. \end{cases} \quad (5.33)$$

Equations (5.33) are defined using spatially continuous variables, i.e. continuous tangential electric and magnetic fields. The spatially discrete counterpart of Equation (5.33) for the time domain simulations is introduced later in Section 5.4.1. However, first the ADE method is introduced, also first for spatially continuous variables.

---

### 5.3.4 Auxiliary Differential Equation (ADE)

---

In this chapter an overview of ADE method to model the dispersive surface impedance function in the time domain is given. ADE method has been utilized in e.g. [31] for modeling dispersive media. As with RC in the previous section 5.3.3, let us begin with the standard SIBC approach presented in Section 4.2.1. Denoting the tangential magnetic field on the surface  $\vec{n} \times \vec{H}$  as  $\vec{H}_t$ , and the tangential electric field  $\vec{n} \times \vec{n} \times \vec{E}$  as  $\vec{E}_t$ , the relation between them (4.20) can be written in the frequency domain as

$$\vec{E}_t(\omega) = Z(\omega) \vec{H}_t(\omega). \quad (5.34)$$

Again, let us recall the vector fitting approximation (5.2) for the impedance function:

$$Z(\omega) \approx \sum_{i=1}^P \frac{c_i}{j\omega - a_i}, \quad (5.35)$$

where  $P$  is the number of rational interpolants, and  $a_i$ ,  $c_i$  are real fitting parameters. Let us insert the impedance approximation (5.35) into the frequency domain expression for SIBC (5.34), to obtain an approximative relation between tangential electric and magnetic fields on the surface:

$$\vec{E}_t(\omega) \approx \sum_{i=1}^P c_i \frac{\vec{H}_t(\omega)}{j\omega - a_i}. \quad (5.36)$$

Let us call the  $i^{\text{th}}$  term of the sum in Equation (5.36) as an auxiliary variable, denoted as  $\vec{\mathcal{A}}_i$  and defined as:

$$\vec{\mathcal{A}}_i = \frac{c_i \vec{H}_t(\omega)}{j\omega - a_i}, \quad (5.37)$$

and furthermore:

$$\vec{E}_t(\omega) \approx \sum_{i=1}^P \vec{\mathcal{A}}_i. \quad (5.38)$$

Multiplying both sides of Equation (5.37) by the denominator of the right-hand side ( $j\omega - a_i$ ) leads to:

$$(j\omega - a_i) \vec{\mathcal{A}}_i(\omega) = c_i \vec{H}_t(\omega), \quad (5.39)$$

and furthermore to

$$j\omega \vec{\mathcal{A}}_i(\omega) - a_i \vec{\mathcal{A}}_i(\omega) = c_i \vec{H}_t(\omega). \quad (5.40)$$

Taking the inverse Laplace transform (5.17) of both sides of Equation (5.40)

$$\mathcal{L}^{-1} \{j\omega \vec{\mathcal{A}}_i(\omega) - a_i \vec{\mathcal{A}}_i(\omega)\} = \mathcal{L}^{-1} \{c_i \vec{H}_t(\omega)\} \quad (5.41)$$

leads to:

$$\frac{d}{dt} \vec{\mathcal{A}}_i(t) - a_i \vec{\mathcal{A}}_i(t) = c_i \vec{H}_t(t). \quad (5.42)$$

Let us next apply the implicit backward Euler method [8] to Equation (5.42) in order to obtain a discrete time domain scheme. The tangential magnetic field  $\vec{H}_t$  and the auxiliary variable  $\vec{\mathcal{A}}_i$  at the time step  $n\Delta t$  are denoted as  $\vec{H}_t^n$ , and  $\vec{\mathcal{A}}_i^n$ , respectively. The discrete time domain scheme can therefore be written as:

$$\frac{1}{\Delta t} (\vec{\mathcal{A}}_i^{n+1} - \vec{\mathcal{A}}_i^n) - a_i \vec{\mathcal{A}}_i^{n+1} = c_i \vec{H}_t^{n+1}. \quad (5.43)$$

The auxiliary variable  $\vec{\mathcal{A}}_i$  at the time step  $(n+1)\Delta t$  can consequently be written as

$$\vec{\mathcal{A}}_i^{n+1} = \zeta_{i1}^A \vec{\mathcal{A}}_i^n + \zeta_{i2}^A \vec{H}_t^{n+1}, \quad (5.44)$$

or accordingly at time step  $n\Delta t$  as

$$\vec{\mathcal{A}}_i^n = \zeta_{i1}^A \vec{\mathcal{A}}_i^{n-1} + \zeta_{i2}^A \vec{H}_t^n, \quad (5.45)$$

with coefficients

$$\zeta_{i1}^A = \frac{1}{1 - a_i \Delta t} \quad (5.46)$$

$$\zeta_{i2}^A = \frac{c_i \Delta t}{1 - a_i \Delta t}. \quad (5.47)$$

The impedance boundary condition in Equation (5.34) can now be written in the discrete time domain as

$$\begin{cases} \vec{E}_t^n = \sum_{i=1}^P \vec{\mathcal{A}}_i^n \\ \vec{\mathcal{A}}_i^n = \zeta_{i1}^A \vec{\mathcal{A}}_i^{n-1} + \zeta_{i2}^A \vec{H}_t^n. \end{cases} \quad (5.48)$$

The Equations (5.48) are defined using spatially continuous variables, i.e. continuous tangential electric and magnetic fields. The spatially discrete counterpart of Equation (5.48) for the time domain simulations is introduced later in Section 5.4.2.

---

## 5.4 TD Solver Implementation

---

In the previous sections, two methods to approximate the surface impedance boundary conditions in discrete time domain, namely RC and ADE methods, were introduced. In this section the implementation of these methods to DG-FEM is presented. This means, in addition to temporally discrete scheme presented in the previous sections, spatially discrete schemes are obtained. Let us recall the boundary value problem (5.1) given in the introduction of this chapter (Section 5.1):

$$\begin{cases} \nabla \times \vec{E} = -\frac{\partial \vec{B}}{\partial t} & \text{in } \Omega \\ \nabla \times \vec{H} = \frac{\partial \vec{D}}{\partial t} & \text{in } \Omega \\ \vec{n} \times \vec{n} \times \vec{E} = f(\omega)(\vec{n} \times \vec{H}) & \text{on } \partial\Omega. \end{cases} \quad (5.49)$$

Accordingly to the DG-FEM frequency domain formulation (4.2) in Section 4, we can write the equations in the following, spatially discrete, form:

$$\begin{cases} \mathbf{C}_B \mathbf{e}_t(t) + \frac{d}{dt} \mathbf{M}_\mu \mathbf{h}(t) = \mathbf{C}_Z \mathbf{e}_t(t) \\ \mathbf{C}_D \mathbf{h}(t) - \frac{d}{dt} \mathbf{M}_\varepsilon \mathbf{e}_t(t) = 0, \end{cases} \quad (5.50)$$

where  $\mathbf{e}_t(t)$  is the DG-FEM discretized counterpart for the tangential electric field  $\vec{E}_t(t) = \vec{n} \times \vec{n} \times \vec{E}(t)$ , matrices  $\mathbf{C}_B$ ,  $\mathbf{C}_D$ ,  $\mathbf{M}_\mu$ , and  $\mathbf{M}_\varepsilon$  as defined in Equations (3.14)-(3.17), and the matrix  $\mathbf{C}_Z$  is equal to the frequency domain definition in Equation (4.52) in Section 4.5. Let us next apply RC and ADE methods, and Verlet intergration presented in Section 3.4.2, to obtain a DG-FEM time-stepping scheme.

---

#### 5.4.1 DG-FEM in Time Domain with RC

---

The approximation of the tangential electric field  $\vec{E}_t$  in the discrete time domain in terms of RC method reads as in Equation (5.33):

$$\begin{cases} \vec{E}_t^n = \sum_{i=1}^P \vec{\mathcal{R}}_i^n \\ \vec{\mathcal{R}}_i^n = \zeta_{1i}^R \vec{H}_t^n + \zeta_{2i}^R \vec{H}_t^{n-1} + \zeta_{3i}^R \vec{\mathcal{R}}_i^{n-1}. \end{cases} \quad (5.51)$$

The DG-FEM discretized counterpart for the aforementioned equations are:

$$\begin{cases} \mathbf{e}_t^n = \sum_{i=1}^P \mathcal{R}_i^n \\ \mathcal{R}_i^n = \zeta_{1i}^R \mathbf{h}_t^n + \zeta_{2i}^R \mathbf{h}_t^{n-1} + \zeta_{3i}^R \mathcal{R}_i^{n-1}. \end{cases} \quad (5.52)$$


---

The definition of the auxiliary variable  $\mathcal{R}_i$  differs from the definition of  $\vec{\mathcal{R}}_i$  in Equation (5.33) slightly. The auxiliary variable  $\mathcal{R}_i$  is now a column vector with the same dimension as  $\mathbf{h}$ , i.e.  $N_H$ , see Equation (3.8) in Section 3.3. Substituting  $\mathbf{e}_t^n$  in Equation (5.50) with Equations (5.52) and applying Verlet integrator (3.21) leads to:

$$\left\{ \begin{array}{l} \mathbf{C}_B \mathbf{e}^n + \mathbf{M}_\mu \frac{1}{\Delta t/2} (\mathbf{h}^{n+\frac{1}{2}} - \mathbf{h}^{n-\frac{1}{2}}) = \mathbf{C}_Z \sum_{i=1}^P \mathcal{R}_i^{n-\frac{1}{2}} \\ \mathcal{R}_i^{n+\frac{1}{2}} = \zeta_{1i}^R \mathbf{h}_t^{n+\frac{1}{2}} + \zeta_{2i}^R \mathbf{h}_t^{n-\frac{1}{2}} + \zeta_{3i}^R \mathcal{R}_i^{n-\frac{1}{2}} \\ \mathbf{C}_D \mathbf{h}^{n+\frac{1}{2}} - \mathbf{M}_\varepsilon \frac{1}{\Delta t} (\mathbf{e}^{n+1} - \mathbf{e}^n) = 0 \\ \mathbf{C}_B \mathbf{e}^{n+1} + \mathbf{M}_\mu \frac{1}{\Delta t/2} (\mathbf{h}^{n+\frac{3}{2}} - \mathbf{h}^{n+\frac{1}{2}}) = \mathbf{C}_Z \sum_{i=1}^P \mathcal{R}_i^{n+\frac{1}{2}}. \\ \mathcal{R}_i^{n+\frac{3}{2}} = \zeta_{1i}^R \mathbf{h}_t^{n+\frac{3}{2}} + \zeta_{2i}^R \mathbf{h}_t^{n+\frac{1}{2}} + \zeta_{3i}^R \mathcal{R}_i^{n+\frac{1}{2}}. \end{array} \right. \quad (5.53)$$

Solving for the electric and magnetic degrees of freedom at time steps  $(n + \frac{1}{2})\Delta t$ ,  $(n + 1)\Delta t$ , and  $(n + \frac{3}{2})\Delta t$  according to Verlet method (3.22) leads to:

$$\left\{ \begin{array}{l} \mathbf{h}^{n+\frac{1}{2}} = \mathbf{h}^{n-\frac{1}{2}} - \mathbf{C}'_B \mathbf{e}^n + \mathbf{C}'_Z \sum_{i=1}^P \mathcal{R}_i^{n-\frac{1}{2}} \\ \mathcal{R}_i^{n+\frac{1}{2}} = \zeta_{1i}^R \mathbf{h}_t^{n+\frac{1}{2}} + \zeta_{2i}^R \mathbf{h}_t^{n-\frac{1}{2}} + \zeta_{3i}^R \mathcal{R}_i^{n-\frac{1}{2}} \\ \mathbf{e}^{n+1} = \mathbf{e}^n + \mathbf{C}'_D \mathbf{h}^{n+\frac{1}{2}} \\ \mathbf{h}^{n+\frac{3}{2}} = \mathbf{h}^{n+\frac{1}{2}} - \mathbf{C}'_B \mathbf{e}^{n+1} + \mathbf{C}'_Z \sum_{i=1}^P \mathcal{R}_i^{n+\frac{1}{2}} \\ \mathcal{R}_i^{n+\frac{3}{2}} = \zeta_{1i}^R \mathbf{h}_t^{n+\frac{3}{2}} + \zeta_{2i}^R \mathbf{h}_t^{n+\frac{1}{2}} + \zeta_{3i}^R \mathcal{R}_i^{n+\frac{1}{2}} \end{array} \right. \quad (5.54)$$

with matrices:

$$\mathbf{C}'_B = 2\Delta t \mathbf{M}_\mu^{-1} \mathbf{C}_B, \quad \mathbf{C}'_Z = 2\Delta t \mathbf{M}_\mu^{-1} \mathbf{C}_Z \text{ and } \mathbf{C}'_D = \Delta t \mathbf{M}_\varepsilon^{-1} \mathbf{C}_D. \quad (5.55)$$

Equations (5.54) are the time-stepping scheme for time-domain DG-FEM with RC method. The equations are used to obtain the results for convergence studies

later in Section 5.5. In the next section, the corresponding time-stepping scheme for ADE method is introduced.

---

#### 5.4.2 DG-FEM in Time Domain with ADE

---

The approximation of the tangential electric field  $\vec{E}_t$  in the discrete time domain in terms of ADE method reads as in Equation (5.48):

$$\begin{cases} \vec{E}_t^n = \sum_{i=1}^P \mathcal{A}_i^n \\ \mathcal{A}_i^n = \zeta_{1i}^A \mathcal{A}_i^{n-1} + \zeta_{2i}^A \vec{H}_t^n. \end{cases} \quad (5.56)$$

The DG-FEM discretized counterpart for the aforementioned equations are:

$$\begin{cases} \mathbf{e}_t^n = \sum_{i=1}^P \mathcal{A}_i^n \\ \mathcal{A}_i^n = \zeta_{1i}^A \mathbf{h}_t^n + \zeta_{2i}^A \mathcal{A}_i^{n-1}. \end{cases} \quad (5.57)$$

The definition of the auxiliary variable  $\mathcal{R}_i$  differs from the definition of  $\vec{\mathcal{A}}_i$  in Equation (5.48) slightly. The auxiliary variable  $\mathcal{A}_i$  is now a column vector with the same dimension as  $\mathbf{h}$ , i.e.  $N_H$ , see Equation (3.8) in Section 3.3. Substituting  $\mathbf{e}_t^n$  in Equation (5.50) with Equations (5.57) and applying Verlet integrator (3.21) leads to:

$$\begin{cases} \mathbf{C}_B \mathbf{e}^n + \mathbf{M}_\mu \frac{1}{\Delta t/2} (\mathbf{h}^{n+\frac{1}{2}} - \mathbf{h}^{n-\frac{1}{2}}) = \mathbf{C}_Z \sum_{i=1}^P \mathcal{A}_i^{n-\frac{1}{2}} \\ \mathcal{A}_i^{n+\frac{1}{2}} = \zeta_{1i}^A \mathbf{h}_t^{n+\frac{1}{2}} + \zeta_{2i}^A \mathcal{A}_i^{n-\frac{1}{2}} \\ \mathbf{C}_D \mathbf{h}^{n+\frac{1}{2}} - \mathbf{M}_e \frac{1}{\Delta t} (\mathbf{e}^{n+1} - \mathbf{e}^n) = 0 \\ \mathbf{C}_B \mathbf{e}^{n+1} + \mathbf{M}_\mu \frac{1}{\Delta t/2} (\mathbf{h}^{n+\frac{3}{2}} - \mathbf{h}^{n+\frac{1}{2}}) = \mathbf{C}_Z \sum_{i=1}^P \mathcal{A}_i^{n+\frac{1}{2}} \\ \mathcal{A}_i^{n+\frac{3}{2}} = \zeta_{1i}^A \mathbf{h}_t^{n+\frac{3}{2}} + \zeta_{2i}^A \mathcal{A}_i^{n+\frac{1}{2}}. \end{cases} \quad (5.58)$$

Solving for the electric and magnetic degrees of freedom at the time steps  $(n + \frac{1}{2})\Delta t$ ,  $(n+1)\Delta t$ , and  $(n + \frac{3}{2})\Delta t$  according to Verlet method (3.22):

$$\left\{ \begin{array}{l} \mathbf{h}^{n+\frac{1}{2}} = \mathbf{h}^{n-\frac{1}{2}} - \mathbf{C}'_{\text{B}} \mathbf{e}^n + \mathbf{C}'_{\text{Z}} \sum_{i=1}^P \mathcal{A}_i^{n-\frac{1}{2}} \\ \mathcal{A}_i^{n+\frac{1}{2}} = \zeta_{1i}^{\text{A}} \mathbf{h}_t^{n+\frac{1}{2}} + \zeta_{2i}^{\text{A}} \mathcal{A}_i^{n-\frac{1}{2}} \\ \mathbf{e}^{n+1} = \mathbf{e}^n + \mathbf{C}'_{\text{D}} \mathbf{h}^{n+\frac{1}{2}} \\ \mathbf{h}^{n+\frac{3}{2}} = \mathbf{h}^{n+\frac{1}{2}} - \mathbf{C}'_{\text{B}} \mathbf{e}^{n+1} + \mathbf{C}'_{\text{Z}} \sum_{i=1}^P \mathcal{A}_i^{n+\frac{1}{2}} \\ \mathcal{A}_i^{n+\frac{3}{2}} = \zeta_{1i}^{\text{A}} \mathbf{h}_t^{n+\frac{3}{2}} + \zeta_{2i}^{\text{A}} \mathcal{A}_i^{n+\frac{1}{2}}, \end{array} \right. \quad (5.59)$$

with matrices

$$\mathbf{C}'_{\text{B}} = 2\Delta t \mathbf{M}_{\mu}^{-1} \mathbf{C}_{\text{B}}, \quad \mathbf{C}'_{\text{Z}} = 2\Delta t \mathbf{M}_{\mu}^{-1} \mathbf{C}_{\text{Z}} \text{ and } \mathbf{C}'_{\text{D}} = \Delta t \mathbf{M}_{\varepsilon}^{-1} \mathbf{C}_{\text{D}}. \quad (5.60)$$

Equations (5.59) are the time-stepping scheme for time-domain DG-FEM with ADE method. The equations are used to obtain the results for numerical examples and convergence studies later in Section 5.5. In the next section, ADE and RC methods are compared in terms of accuracy and computational cost.

---

### 5.4.3 Comparison of ADE and RC Methods

---

The SIBC with DG-FEM discretized electric and magnetic fields reads as

$$\mathbf{e}_t(\omega) = Z(\omega) \mathbf{h}_t(\omega), \quad (5.61)$$

and the DG-FEM discretized Maxwell's equations (4.53) in the time domain as:

$$\left\{ \begin{array}{l} \mathbf{C}_{\text{B}} \mathbf{e}(t) + \frac{d}{dt} \mathbf{M}_{\mu} \mathbf{h}(t) = \mathbf{C}_{\text{Z}} \mathbf{e}_t(t) \\ \mathbf{C}_{\text{D}} \mathbf{h}(t) - \frac{d}{dt} \mathbf{M}_{\varepsilon} \mathbf{e}(t) = 0, \end{array} \right. \quad (5.62)$$

The SIBC in terms of RC method reads in discrete time domain as:



$$\left\{ \begin{array}{l} \mathbf{h}^{n+\frac{1}{2}} = \mathbf{h}^{n-\frac{1}{2}} - \mathbf{C}'_B \mathbf{e}^n + \mathbf{C}'_Z \sum_{i=1}^P \mathcal{R}_i^{n-\frac{1}{2}} \\ \mathcal{R}_i^{n+\frac{1}{2}} = \zeta_{1i}^R \mathbf{h}_t^{n+\frac{1}{2}} + \zeta_{2i}^R \mathbf{h}_t^{n-\frac{1}{2}} + \zeta_{3i}^R \mathcal{R}_i^{n-\frac{1}{2}} \\ \mathbf{e}^{n+1} = \mathbf{e}^n + \mathbf{C}'_D \mathbf{h}^{n+\frac{1}{2}} \\ \mathbf{h}^{n+\frac{3}{2}} = \mathbf{h}^{n+\frac{1}{2}} - \mathbf{C}'_B \mathbf{e}^{n+1} + \mathbf{C}'_Z \sum_{i=1}^P \mathcal{R}_i^{n+\frac{1}{2}} \\ \mathcal{R}_i^{n+\frac{3}{2}} = \zeta_{1i}^R \mathbf{h}_t^{n+\frac{3}{2}} + \zeta_{2i}^R \mathbf{h}_t^{n+\frac{1}{2}} + \zeta_{3i}^R \mathcal{R}_i^{n+\frac{1}{2}} \end{array} \right. \quad (5.63)$$

with matrices  $\mathbf{C}'_B$ ,  $\mathbf{C}'_Z$ , and  $\mathbf{C}'_D$  defined in Equation (5.55), and with coefficients

$$\zeta_{1i}^R = \frac{c_i}{a_i} \left[ 1 + \frac{1}{\Delta a_i} (e^{-a_i \Delta t} - 1) \right] \quad (5.64)$$

$$\zeta_{2i}^R = \frac{c_i}{a_i} \left[ \frac{1}{\Delta a_i} - e^{-a_i \Delta t} \left( 1 + \frac{1}{\Delta a_i} \right) \right] \quad (5.65)$$

$$\zeta_{3i}^R = \frac{c_i}{a_i} e^{-a_i \Delta t}. \quad (5.66)$$

Respectively, the ADE method reads as

$$\left\{ \begin{array}{l} \mathbf{h}^{n+\frac{1}{2}} = \mathbf{h}^{n-\frac{1}{2}} - \mathbf{C}'_B \mathbf{e}^n + \mathbf{C}'_Z \sum_{i=1}^P \mathcal{A}_i^{n-\frac{1}{2}} \\ \mathcal{A}_i^{n+\frac{1}{2}} = \zeta_{1i}^A \mathbf{h}_t^{n+\frac{1}{2}} + \zeta_{2i}^A \mathcal{A}_i^{n-\frac{1}{2}} \\ \mathbf{e}^{n+1} = \mathbf{e}^n + \mathbf{C}'_D \mathbf{h}^{n+\frac{1}{2}} \\ \mathbf{h}^{n+\frac{3}{2}} = \mathbf{h}^{n+\frac{1}{2}} - \mathbf{C}'_B \mathbf{e}^{n+1} + \mathbf{C}'_Z \sum_{i=1}^P \mathcal{A}_i^{n+\frac{1}{2}} \\ \mathcal{A}_i^{n+\frac{3}{2}} = \zeta_{1i}^A \mathbf{h}_t^{n+\frac{3}{2}} + \zeta_{2i}^A \mathcal{A}_i^{n+\frac{1}{2}}, \end{array} \right. \quad (5.67)$$

with matrices  $\mathbf{C}'_B$ ,  $\mathbf{C}'_Z$ , and  $\mathbf{C}'_D$  defined in Equation (5.55), and with coefficients

$$\zeta_{i1}^A = \frac{1}{1 - a_i \Delta t} \quad (5.68)$$

$$\zeta_{i2}^A = \frac{c_i \Delta t}{1 - a_i \Delta t}. \quad (5.69)$$

As can be seen in Equation (5.63), computing the auxiliary RC variable  $\mathcal{R}_i^{n+\frac{1}{2}}$  requires a sum of three vectors:  $\mathbf{h}^{n+\frac{1}{2}}$ ,  $\mathbf{h}^{n-\frac{1}{2}}$ , and  $\mathcal{R}_i^{n-\frac{1}{2}}$ , i.e. the current magnetic field, the magnetic field at the previous time step, and the auxiliary variable at the previous time step, respectively. The sum needs to be computed  $P$  times, for each of the in total  $P$  auxiliary variables. Additionally, the sum of the auxiliary variables need to be multiplied with the matrix  $\mathbf{C}'_Z$  and summed up when computing the magnetic field  $\mathbf{h}^{n+\frac{1}{2}}$ . Therefore the number of additional operations at every half time step is five. Not only the number of additional operations per time step affects on computational cost, but also the additional memory needed to store the additional vectors. The additional vectors to be stored in RC method at every half time step, are  $\mathcal{R}_i^{n-\frac{1}{2}}$  ( $\forall i = 1..P$ ),  $\sum_{i=1}^P \mathcal{R}_i^{n+\frac{1}{2}}$ , and  $\mathbf{h}^{n-\frac{1}{2}}$ , i.e. in total  $P + 2$  vectors. The current magnetic field  $\mathbf{h}^{n+\frac{1}{2}}$  is needed also for computing the current electric field  $\mathbf{e}^{n+1}$ , and therefore does not count in additional vectors due to RC method.

Computing the ADE auxiliary variable  $\mathcal{A}_i$  (5.67) requires a sum of two vectors:  $\mathbf{h}^{n+\frac{1}{2}}$ , and  $\mathcal{A}_i^{n-\frac{1}{2}}$ , i.e. the current magnetic field, and the auxiliary variable at the previous half time step. The sum needs to be computed  $P$  times, for each of the in total  $P$  auxiliary variables. Additionally, the sum of the auxiliary variables need to be multiplied with the matrix  $\mathbf{C}'_Z$  and summed up when computing the magnetic field  $\mathbf{h}^{n+\frac{1}{2}}$ . Therefore the number of additional operations at every half time step is four. The additional vectors to be stored in ADE method at every time step, are  $\mathcal{A}_i^{n-\frac{1}{2}}$  ( $\forall i = 1..P$ ), and  $\sum_{i=1}^P \mathcal{A}_i^{n+\frac{1}{2}}$ , i.e. in total  $P + 1$  vectors. The current magnetic field  $\mathbf{h}^{n+\frac{1}{2}}$  is needed also for computing the current electric field  $\mathbf{e}^{n+1}$ , and therefore does not count in additional vectors due to ADE method.

Although RC method requires more operations, as well as storing one additional vector at each time step, the approximation in the discrete time domain is more accurate in RC method: The approximation of the magnetic field in RC method is linear with respect to time, see Equation (5.28). In contrast, in ADE method,

the approximation of the magnetic field is constant with respect to time, see Equation (5.43).

Additionally, RC method requires  $3P$  coefficients ( $\zeta_{1i}^R$ ,  $\zeta_{2i}^R$ , and  $\zeta_{3i}^R$ ,  $\forall i = 1 \dots P$ ) to be computed, while ADE method only  $2P$  ( $\zeta_{1i}^A$ , and  $\zeta_{2i}^A$ ,  $\forall i = 1 \dots P$ ). However, the coefficients are computed in the pre-processing phase (see Section 1), and therefore this does not have a significant effect on total CPU time. The differences between RC and ADE methods are summarized in Table 5.4 and the desired features of the methods are qualified with "+" sign.

Table 5.4.: Comparison of ADE and RC methods in terms of accuracy and efficiency.

	ADE	RC
type of magnetic field approximation	constant	linear (+)
additional operations per half time step	4 (+)	5
additional vectors to be stored	$P + 1$ (+)	$P + 2$
coefficients to be computed	$2P$ (+)	$3P$

As a conclusion, the RC method is more accurate due to the linear field approximations, but the computational cost of ADE method is lower, in terms of number of additional operations per time step and the number of vectors to be stored per time step.

---

## 5.5 Numerical Examples

---

In this section, previously introduced schemes for modeling of SIBC with DG-FEM in the discrete time domain, are validated and verified by numerical examples and convergence studies. The SIBC functions are approximated in the frequency domain using the vector fitting procedure, as introduced in Section 5.2. The time domain results are obtained by approximating SIBC by RC and ADE methods, as proposed in Sections 5.3.3 and 5.3.4, respectively. RC and ADE schemes are also compared in terms of accuracy and solver times.

Test structures for the numerical examples and convergence studies are cavity resonators with lossy walls, with different geometries and material parameters. The verification of the numerical schemes is performed by comparing the fundamental resonance frequencies  $f_0$  and the  $Q$  factors of the resonators with the results obtained by the Power Loss method [40]. The resonance frequencies  $f_0$  as well as the  $Q$  factors are obtained by running the simulations with the time stepping schemes (5.54) and (5.54), and extracting them from the time domain

---

signal by applying Prony's method [75]. In the following section, Prony's method is introduced.

---

### 5.5.1 Prony's Method

---

The Q factor is an useful parameter to verify the losses of a resonator, as already seen in Section 4.7.1. Therefore, in addition to verifying the frequency domain scheme, it is exploited in the time domain as well. In the time domain simulations, the time signal of a resonator is recorded at every time step, and the Q factor is extracted by means of Prony's method. The method was first proposed by Gaspard de Prony as early as in in year 1795 [75], and it was first applied in electromagnetic simulations 200 years later by Hauer [45]. The method is capable to estimate the frequency components of a signal, and the corresponding damping coefficients [45]. According to Hauer [45], Prony's method estimates the time domain signal  $x(t)$  as a sum of complex damped sinusoidal signals:

$$x(t) \approx \sum_{i=1}^L A_i e^{\sigma_i t} \cos(\omega_i t + \varphi_i), \quad (5.70)$$

where  $L$  is the number of frequency components of the approximation,  $A_i$  is the amplitude,  $\sigma_i$  the damping coefficient,  $\omega_i$  the angular frequency, and  $\varphi_i$  the phase of the frequency component  $i$ . The Q factor of the frequency component  $i$  can be calculated as

$$Q_i = \frac{\omega_i}{\sigma_i}. \quad (5.71)$$

Prony's method performs poorly in the presence of noise [45]. To overcome this problem in our simulations, we filter the obtained time domain signal with a low-pass filter in case of the fundamental frequency of a resonator. Figures 5.4(a) and 5.4(c) show the original and the filtered damped signals of a resonator, whereas Figures 5.4(b) and 5.4(d) show the filtered signal and the signal fitted by Prony's method. Figures 5.4(a) and (b) present a signal of a high-loss resonator, and the attenuation of the signal is clearly visible. The signals in Figures 5.4(c) and (d) represent low-loss resonator.

---

## 5.5.2 Cavity Resonator with Lossy Walls

---

In this section, fundamental frequencies  $f_0$  and Q factors of cavity resonators are investigated in the discrete time domain, in order to verify and validate the developed schemes for modeling surface impedance boundary conditions. In Section 5.5.2.1, a numerical example is given, where the Q factors of lossy resonators are investigated on a wide frequency band. The results obtained by the ADE method, are compared with the Power Loss method, as well as CST Transient solver results.

In Section 5.5.2.2, the convergence studies of ADE and RC methods are performed. The convergence is studied by investigating the fundamental frequencies and Q factors of different cavity resonators. The performance and accuracy of ADE and RC methods are compared, and the accuracy is also compared with CST Transient solver.

---

### 5.5.2.1 Q factor of Cavity Resonator

---

As a numerical example, Q factors of cavity resonators are investigated. The Q factors are obtained by two time domain methods, namely the ADE method proposed in this thesis (in Section 5.4.2), and CST Transient solver, as well the Power Loss method (Equation (4.83) in Section 4.7.1).

Cavity resonators with three different edge lengths  $l$ , namely  $l = 10\text{cm}$ ,  $l = 1\text{m}$ , and  $l = 10\text{m}$ , are investigated. The corresponding fundamental frequencies are 2.12GHz, 0.212GHz, and 0.0212GHz, respectively. The conductivity of the resonator walls is  $5.8 \cdot 10^9\text{S/m}$ . A wide range of resonator sizes, and consequently a wide range of frequencies, is chosen as numerical examples to demonstrate the applicability of the wideband impedance approximation (see Section 5.2).

The number of interpolants of the impedance approximation is 10, and the frequency range is from 1MHz to 100GHz. The impedance approximation coefficients  $a_i$  and  $c_i$  are given in Table A.5 in Appendix A. The analytical impedances  $Z$  (4.19), the impedance approximations  $Z_{\text{appr.}}$ , and the relative deviations of the absolute values of the impedances at the resonance frequencies of different resonators are given in Table 5.5. As can be seen, the agreement between the analytical impedances and impedance approximations is very good on a wide frequency range.

Table 5.5.: Analytical impedances  $Z$ , and impedance approximations  $Z_{\text{appr.}}$  at the fundamental resonance frequencies  $f_0$  of resonators with different edge lengths.

$l$	$f_0$	$Z(f_0)$	$Z_{\text{appr.}}(f_0)$	$\Delta$
10cm	2.12GHz	$(1.201 + j1.201)\text{m}\Omega$	$(1.183 + j1.173)\text{m}\Omega$	1.9 %
1m	0.212GHz	$(379.9 + j379.9)\mu\Omega$	$(377.7 + j377.7)\mu\Omega$	0.58 %
10m	0.0212GHz	$(120.1 + j120.1)\mu\Omega$	$(119.5 + j120.1)\mu\Omega$	0.26 %

CST Transient solver is run with PEC boundary condition, and field monitors are set to monitor the electric and magnetic field at the fundamental frequency of the resonator. The Q factors are calculated in the post-processing phase. In ADE method, the simulations are run until 10ms (50ms for the resonator with edge length 10m), and the time signal is recorded at every time step. The Prony's method (Section 5.5.1) is applied to the time signals, in order to obtain the Q factors. In CST Transient solver and ADE simulations, the mesh resolution  $h$  is 6 mesh lines/resonator edge length, which corresponds to 7.1 mesh lines/wavelength, independent on the resonator size. In ADE method, the basis function order is set to zero.

The results are given in Tables 5.6, 5.7, and 5.8. The conductivity is  $5.8 \cdot 10^9 \text{S/m}$ , which is very high (see condition for a good conductor in Section 4.2.1), and therefore the Q factors calculated by the Power Loss method are very accurate, as the accuracy of the method is proportional to conductivity. As can be seen, the Q factors obtained by the ADE method, are in a very good agreement with the Q factors calculated by the Power Loss method. The results of ADE method are given also graphically in Figures 5.5, 5.6, and 5.7, where the time series (a), as well as the signal spectrum (b) are shown.

Table 5.6.: Q factors of a cavity resonator with edge length 10cm obtained by Power Loss method, ADE method, and CST Transient solver.

	Q factor
Power Loss method	$2.32 \cdot 10^5$
ADE	$2.34 \cdot 10^5$
CST Transient solver	$2.56 \cdot 10^5$

Table 5.7.: Q factors of a cavity resonator with edge length 1m obtained by Power Loss method, ADE method, and CST Transient solver.

	Q factor
Power Loss method	$7.34 \cdot 10^5$
ADE	$7.61 \cdot 10^5$
CST Transient solver	$8.13 \cdot 10^5$

Table 5.8.: Q factors of a cavity resonator with edge length 10m obtained by Power Loss method, ADE method, and CST Transient solver.

	Q factor
Power Loss method	$2.32 \cdot 10^6$
ADE	$2.47 \cdot 10^6$
CST Transient solver	$2.56 \cdot 10^6$

As can be seen in Figures 5.5-5.7, the losses of the resonator with edge length of 10cm are significantly higher than the losses of the bigger resonators. The explanation can be found in Table 5.5. The impedance at the resonance frequency of the smallest resonator is 1000 times higher than for the bigger resonators, and therefore also the losses are significantly higher. In the next section, the convergence study of the ADE and RC methods for modeling SIBC is performed.

---

### 5.5.2.2 SIBC Convergence Study

---

The test structure for the convergence study is a cubical cavity resonator with lossy walls. The edge length of the cavity is 1m, and the material parameters of the lossy walls are the following: Conductivity  $\sigma = 5.8 \cdot 10^5 \text{S/m}$ , permittivity  $\epsilon = \epsilon_0$ , and permeability  $\mu = \mu_0$ . The cavity is filled with a air, i.e. the permittivity and permeability are  $\epsilon_0$  and  $\mu_0$ , respectively, and the conductivity is zero.

The test structure is spatially discretized by a hexahedral mesh with the mesh resolutions 4.2, 5.7, 7.1, 8.5, 9.9, 11.3, 12.7, and 14.1 mesh lines/wavelength. These resolutions correspond to 3, 4, 5, 6, 7, 8, 9, and 10 mesh lines/resonator edge. An exemplary mesh with a resolution of 5.7 mesh lines/wavelength is given in Figure 4.13 in Section 4.7.2.2. The basis function polynomial orders for the simulations are 0 and 1.

The resolution of the spectrum calculated from the time series is proportional to the total time of the simulation [19]. Therefore, all the simulations are run until

10ms in order to get accurate results for the resonance frequency and the  $Q$  factor. The time step depends on the mesh resolution and the basis function polynomial order, and therefore the number of time steps is different for different simulation setups as well: The smallest amount of time steps is  $3.5 \cdot 10^5$  with the mesh resolution 5.7 mesh lines/wavelength and polynomial order 0, and the highest number of time steps is  $3.9 \cdot 10^6$  with mesh resolution 7.1 mesh lines/wavelength and polynomial order 1.

To overcome the problem with spurious modes in DG-FEM method, the penalization method proposed by Gjonaj and Weiland [33] is utilized. The penalization method shifts the spurious modes to higher frequencies, but the drawback is, that it consequently reduces the stable time step [33]. The penalization factor  $\gamma$  is chosen to be 5, as it seems to be a good compromise between shifting the spurious modes and time step reduction.

The results are obtained with ADE and RC methods, and the methods are also compared in terms of accuracy and solver times. With both of the methods, the impedance approximations  $Z_{VF1}(\omega)$  (5.4) and  $Z_{VF2}(\omega)$  (5.5) are used. Additionally, CST Transient solver is used to obtain the  $Q$  factors of the cavity resonator. These results are presented in Section 5.5.2.3.

#### 5.5.2.2.1 ADE Convergence Study

This section shows the results obtained by the ADE method as introduced in Section 5.3.4. As a reference results to verify the scheme the following values are used: The fundamental frequency  $f_{0,\text{ref.}} = 0.211985\text{GHz}$ , and quality factor  $Q_{\text{ref.}} = 7343.878$ . The fundamental frequency is trivially known for a cubical cavity resonator, and the  $Q$  factor is calculated by the Power Loss method as introduced in Equation (4.83) in Section 4.7.1.

The simulations are run as described above in Section 5.5.2.2, and the relative deviations with respect to the reference results are calculated. The relative deviations are defined as

$$\Delta_{\text{rel.}} = \frac{|Q - Q_{\text{ref.}}|}{Q_{\text{ref.}}} \quad (5.72)$$

for the  $Q$  factor, and

$$\Delta_{\text{rel.}} = \frac{|f_0 - f_{0,\text{ref.}}|}{f_{0,\text{ref.}}} \quad (5.73)$$

for the fundamental resonance frequency. The relative deviations with respect to mesh resolution  $h$  and basis function polynomial order are shown in Figures



5.8 and 5.9 for the impedance approximation  $Z_{\text{VF1}}(\omega)$  (5.4), and in Figures 5.10 and 5.11 for the impedance approximation  $Z_{\text{VF2}}(\omega)$  (5.5). The abbreviation for Time Domain DG-FEM (TDDG) in the figure titles refers to DG-FEM in the discrete time domain, introduced previously in Section 5.4.2. The convergence rates for the relative deviations are given in Table 5.9

The accuracy obtained is very high, especially when taking into account very coarse meshes used for the simulations. The smallest relative deviation of the resonance frequency is  $3.2 \cdot 10^{-3}\%$  and  $5.2 \cdot 10^{-1}$  for the  $Q$  factor. The convergence rates shown in Table 5.9 follow the  $hp$ -convergence rate [7].

Table 5.9.: Convergence rates for the resonance frequency  $f_0$  and the  $Q$  factor of time domain DG-FEM with SIBC ADE method with respect to basis function polynomial order  $p$  and number of impedance interpolants  $P$ .

$p$	$P$	$f_0$	$Q$ factor
0	5	$h^{-2}$	$h^{-2.5}$
1	5	$h^{-3.6}$	$h^{-3.1}$
0	10	$h^{-2}$	$h^{-2.5}$
1	10	$h^{-3.5}$	$h^{-3.1}$

#### 5.5.2.2.2 RC Convergence Study

This section shows the results obtained by the RC method as introduced in Section 5.3.3. As a reference results to verify the scheme the following values are used: The fundamental frequency  $f_{0,\text{ref.}} = 0.211985\text{GHz}$ , and quality factor  $Q_{\text{ref.}} = 7343.878$ . The fundamental frequency is trivially known for the cubical cavity resonator, and the  $Q$  factor is calculated by the Power Loss method as introduced in Equation (4.83) in Section 4.7.1.

The simulations are run as described above in Section 5.5.2.2, and the relative deviations with respect to the reference results are calculated. The relative deviations are defined as

$$\Delta_{\text{rel.}} = \frac{|Q - Q_{\text{ref.}}|}{Q_{\text{ref.}}} \quad (5.74)$$

for the  $Q$  factor, and

$$\Delta_{\text{rel.}} = \frac{|f_0 - f_{0,\text{ref.}}|}{f_{0,\text{ref.}}} \quad (5.75)$$

for the fundamental resonance frequency. The relative deviations with respect to mesh resolution  $h$  and basis function polynomial order are shown in Figures 5.12 and 5.13 for the impedance approximation  $Z_{VF1}(\omega)$  (5.4), and in Figures 5.14 and 5.15 for the impedance approximation  $Z_{VF2}(\omega)$  (5.5). The abbreviation TDDG in the figure titles refers to DG-FEM in the discrete time domain, introduced previously in Section 5.4.1. The convergence rates for the relative deviations are given in Table 5.10.

The accuracy obtained is very high, especially when taking into account very coarse meshes used for the simulations. The smallest relative deviation of the resonance frequency is  $3.2 \cdot 10^{-3}\%$  and  $7.4 \cdot 10^{-1}$  for the  $Q$  factor. The convergence rates shown in Table 5.10 follow the  $hp$ -convergence rate [7].

Table 5.10.: Convergence rates for the resonance frequency  $f_0$  and the  $Q$  factor of time domain DG-FEM with SIBC RC method with respect to basis function polynomial order  $p$  and number of impedance interpolants  $P$ .

$p$	$P$	$f_0$	$Q$ factor
0	5	$h^{-2}$	$h^{-2.5}$
1	5	$h^{-3.6}$	$h^{-3.1}$
0	10	$h^{-2}$	$h^{-2.5}$
1	10	$h^{-3.5}$	$h^{-3.1}$

---

### 5.5.2.3 Accuracy and Performance of ADE and RC

---

In Section 5.4.3, the theoretical differences of ADE and RC methods were pointed out. In this section is shown, how the theoretical differences reflect to simulations. To obtain the results, we have chosen a resonator with edge length of  $l = 1\text{m}$  and wall conductivity  $\sigma = 5.8 \cdot 10^5\text{S/m}$ . We have run the simulations with ADE and RC methods with number of interpolants  $P = 5$  and  $P = 10$  (impedance approximations  $Z_{VF1}(\omega)$  (5.4) and  $Z_{VF2}(\omega)$  (5.5) in Section 5.2) and with mesh resolutions  $h$  5.6, 8.5, and 11.3 lines/wavelength. Table 5.11 shows the solver times for the simulations with ADE method with  $P = 5$  and  $P = 10$ , and Table 5.12 for RC method, respectively. Table 5.13 shows the difference in solver times between the ADE and RC methods with  $P = 10$ .

In addition to solver times, the accuracy of the corresponding simulations is investigated. The accuracy is defined by calculating the relative error of the  $Q$  factor, as given in Equation (5.72). The accuracies of the simulations are given for ADE method in Table 5.14 and for RC method in Table 5.15, respectively.

Table 5.11.: Comparison of solver times of ADE method with respect to  $P$  and mesh resolution  $h$  in terms of elements/wavelength at the fundamental resonance frequency  $f_0$ .

	$h = 5.6$	$h = 8.5$	$h = 11.3$
$P = 5$	6min	35min	2h
$P = 10$	7min	39min	4h
$\Delta_{\text{rel.}}$	9.9%	11.6%	46.8%

Table 5.12.: Comparison of solver times of RC method with respect to  $P$  and mesh resolution  $h$  in terms of elements/wavelength at the fundamental resonance frequency  $f_0$ .

	$h = 5.6$	$h = 8.5$	$h = 11.3$
$P = 5$	7min	37min	2h
$P = 10$	8min	44min	3h
$\Delta_{\text{rel.}}$	14.7%	26.0 %	29.3%

Table 5.13.: Comparison of solver times between ADE and RC methods with respect to mesh resolution  $h$  in terms of elements/wavelength at the fundamental resonance frequency  $f_0$ .

	$h = 5.6$	$h = 8.5$	$h = 11.3$
ADE $P = 5$	6min	35min	2h
RC $P = 5$	7min	37min	2h
$\Delta_{\text{rel.}}$	9.9%	6.9%	5.9%

Table 5.14.: Comparison of accuracy of ADE method with respect to  $P$  and mesh resolution  $h$  in terms of elements/wavelength at the fundamental resonance frequency  $f_0$ .

	$h = 5.6$	$h = 8.5$	$h = 11.3$
$P = 5$	10%	3.7%	1.5%
$P = 10$	10%	4.0%	1.8%

The accuracies of all the simulations, with ADE and RC, with  $P = 5$  and  $P = 10$  are also shown in Figure 5.16. As a conclusion, the differences in accuracies of the both methods, with both number of interpolants, are almost insignifi-

Table 5.15.: Comparison of accuracy of RC method with respect to  $P$  and mesh resolution  $h$  in terms of elements/wavelength at the fundamental resonance frequency  $f_0$ .

	$h = 5.6$	$h = 8.5$	$h = 11.3$
P = 5	11%	4.0%	1.7%
P = 10	11%	4.3%	2.1%

cant. However, the relatively small difference (see Tables 5.2 and 5.3) in the impedance approximations  $Z_{VF1}(\omega)$  and  $Z_{VF2}(\omega)$  can be partly hidden by the method used extracting the time domain results (Prony’s method, see Section 5.5.1). In contrast, the solver times are significantly smaller with smaller number of interpolants, and in general with ADE method. This result is in agreement with the remarks in Section 5.4.3.

Additionally, the results are obtained by CST Transient solver. The mesh resolution for the CST simulations is from 7 to 34 mesh lines/wavelength. The cavity is excited by a Gaussian modulated sine pulse via a discrete port. The simulations are run, until the steady state energy criterion  $-80\text{dB}$  is reached. The simulations are run with the PEC boundary condition, while the electric and magnetic fields are monitored at the fundamental resonance frequency of the resonator (0.211985GHz), and the Q factor is calculated in the post-processing phase. The accuracy of CST results is lower, but the time step used is also smaller, as well as the number of time steps. As an example, with mesh resolution 14 mesh lines/wavelength (10 mesh lines/cavity edge), the time step for CST simulation is  $1.87 \cdot 10^{-10}\text{s}$ , whereas for ADE/RC simulations it is  $1.58 \cdot 10^{-11}\text{s}$ . The numbers of simulated time steps are 154760, and 632008, respectively. However, the number of time steps in ADE/RC methods is intentionally very high, because the accuracy of Prony’s method (see Section 5.5.1), is proportional to the number of time steps. The results obtained with CST Transient solver are also shown in Figure 5.16.

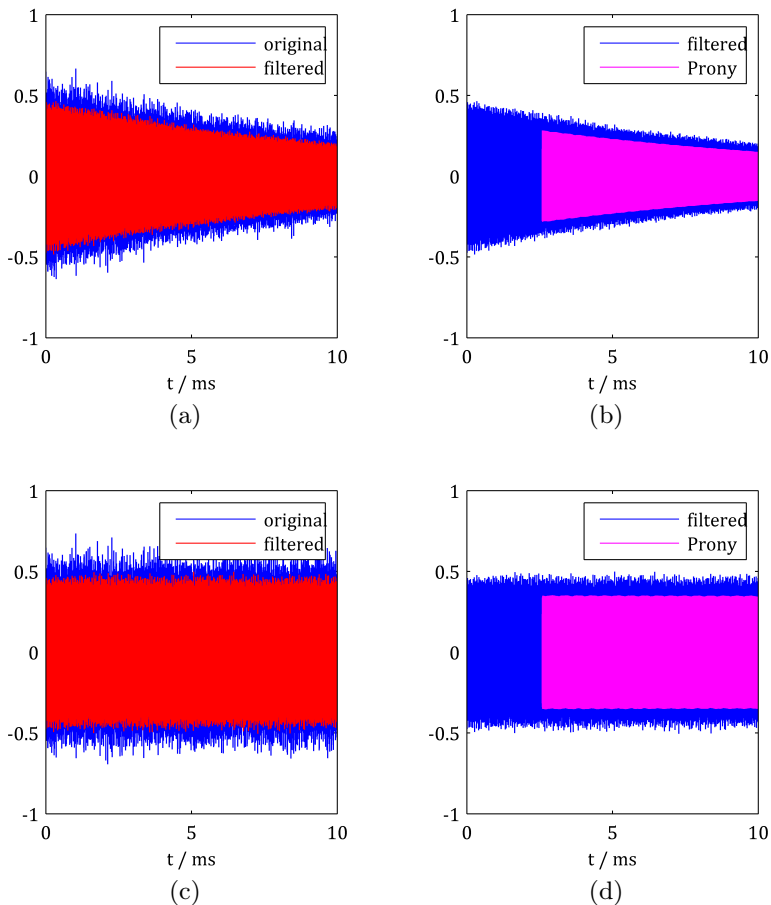
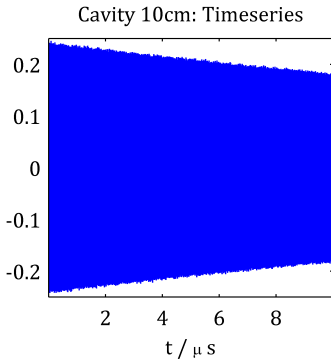
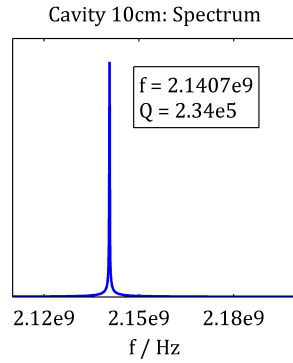


Figure 5.4.: Prony’s method for two resonator signals. Figure (a) shows the original and low-pass filtered time signal of the resonator, and figure (b) shows the filtered signal and the signal fitted by the Prony’s method. The attenuation of the signal is clearly visible due to a relatively low conductivity,  $\sigma = 5.8 \cdot 10^5 \text{S/m}$ . The  $Q$  factor of the signal, computed by the Prony’s method, is 8116. Figures (c) and (d) show the corresponding signals for a low-loss resonator. The attenuation of the signal is not clearly visible due to a high conductivity,  $\sigma = 5.8 \cdot 10^9 \text{S/m}$ . The  $Q$  factor of the signal is 813042.

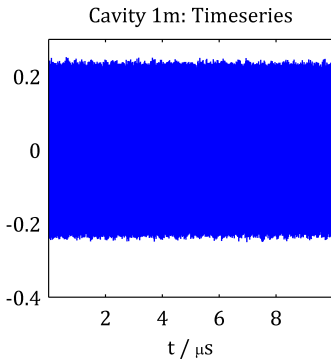


(a)

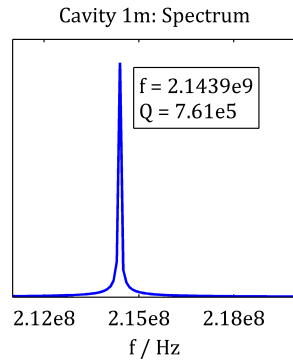


(b)

Figure 5.5.: The time signal (a) and the corresponding spectrum (b) of a cavity resonator with edge length 10cm.



(a)



(b)

Figure 5.6.: The time signal (a) and the corresponding spectrum (b) of a cavity resonator with edge length 1m.

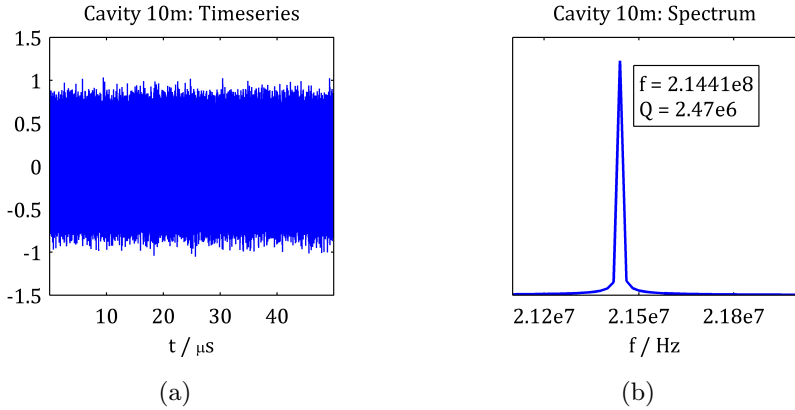


Figure 5.7.: The time signal (a) and the corresponding spectrum (b) of a cavity resonator with edge length 10m.

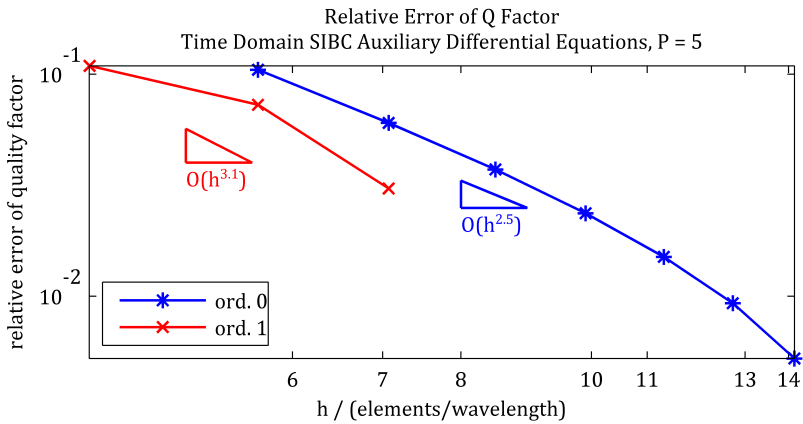


Figure 5.8.: Relative error of the  $Q$  factor of a resonator with  $\sigma = 5.8 \cdot 10^5 \text{S/m}$  and  $l = 1\text{m}$ . Orders 0-1 refer to basis function polynomial order, and the triangles indicate the convergence rates (see also Table 5.9). The mesh resolution  $h$  is 4.2-14.1 edges/wavelength, and smallest reached relative error is  $5.2 \cdot 10^{-3}$ .

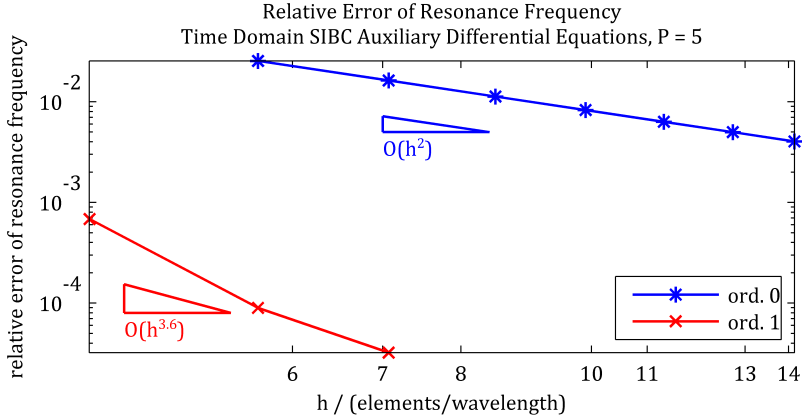


Figure 5.9.: Relative error of the  $f_0$  of a resonator with  $\sigma = 5.8 \cdot 10^5 \text{S/m}$  and  $l = 1\text{m}$ . Orders 0-1 refer to basis function polynomial order, and the triangles indicate the convergence rates (see also Table 5.9). The mesh resolution  $h$  is 4.2-14.1 edges/wavelength, and the smallest reached relative error is  $3.2 \cdot 10^{-5}$ .

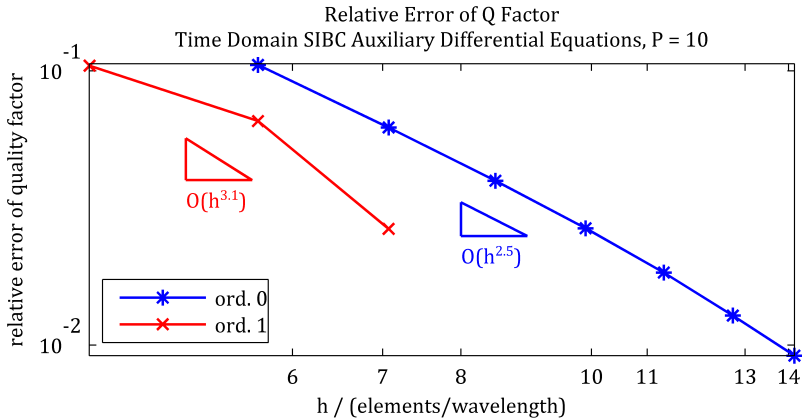


Figure 5.10.: Relative error of the  $Q$  factor of a resonator with  $\sigma = 5.8 \cdot 10^5 \text{S/m}$  and  $l = 1\text{m}$ . Orders 0-1 refer to basis function polynomial order, and the triangles indicate the convergence rates (see also Table 5.9). The mesh resolution  $h$  is 4.2-14.1 edges/wavelength, and the smallest reached relative error is  $9.1 \cdot 10^{-3}$ .



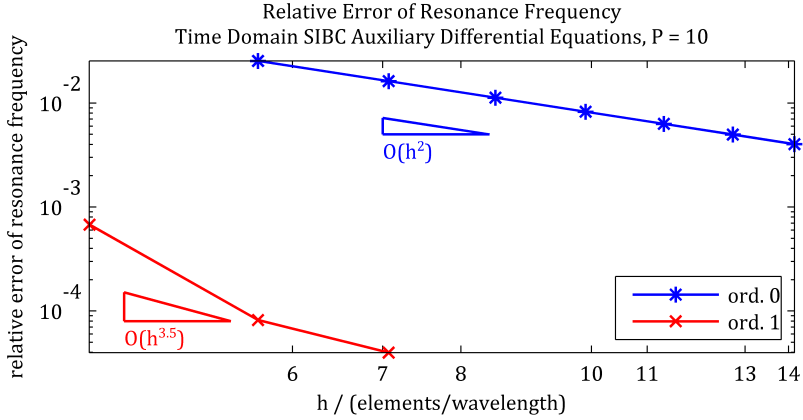


Figure 5.11.: Relative error of the  $f_0$  of a resonator with  $\sigma = 5.8 \cdot 10^5 \text{S/m}$  and  $l = 1\text{m}$ . Orders 0-1 refer to basis function polynomial order, and the triangles indicate the convergence rates (see also Table 5.9). The mesh resolution  $h$  is 4.2-14.1 edges/wavelength, and the smallest reached relative error is  $4.0 \cdot 10^{-5}$ .

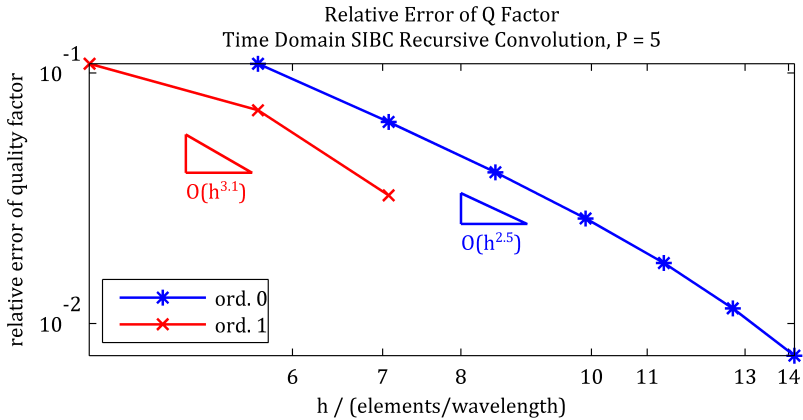


Figure 5.12.: Relative error of the  $Q$  factor of a resonator  $\sigma = 5.8 \cdot 10^5 \text{S/m}$  and  $l = 1\text{m}$ . Orders 0-1 refer to basis function polynomial order, and the triangles indicate the convergence rates (see also Table 5.10). The mesh resolution  $h$  is 4.2-14.1 edges/wavelength, and the smallest reached relative error is  $7.4 \cdot 10^{-3}$ .

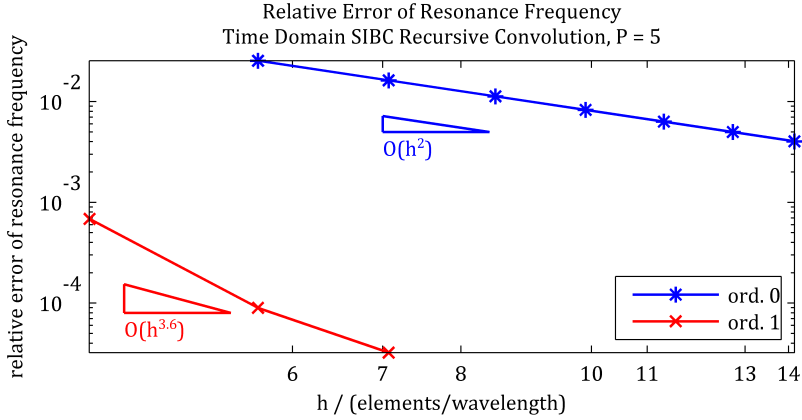


Figure 5.13.: Relative error of the  $f_0$  of a resonator with  $\sigma = 5.8 \cdot 10^5 \text{S/m}$  and  $l = 1\text{m}$ . Orders 0-1 refer to basis function polynomial order, and the triangles indicate the convergence rates (see also Table 5.10). The mesh resolution  $h$  is 4.2-14.1 edges/wavelength, and the smallest reached relative error is  $3.2 \cdot 10^{-5}$ .

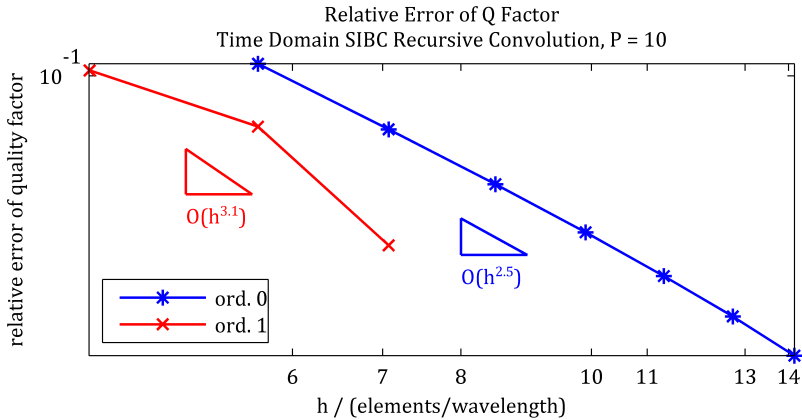


Figure 5.14.: Relative error of the  $Q$  factor of a resonator with  $\sigma = 5.8 \cdot 10^5 \text{S/m}$  and  $l = 1\text{m}$ . Orders 0-1 refer to basis function polynomial order, and the triangles indicate the convergence rates (see also Table 5.10). The mesh resolution  $h$  is 4.2-14.1 edges/wavelength, and the smallest reached relative error is  $1.1 \cdot 10^{-2}$ .

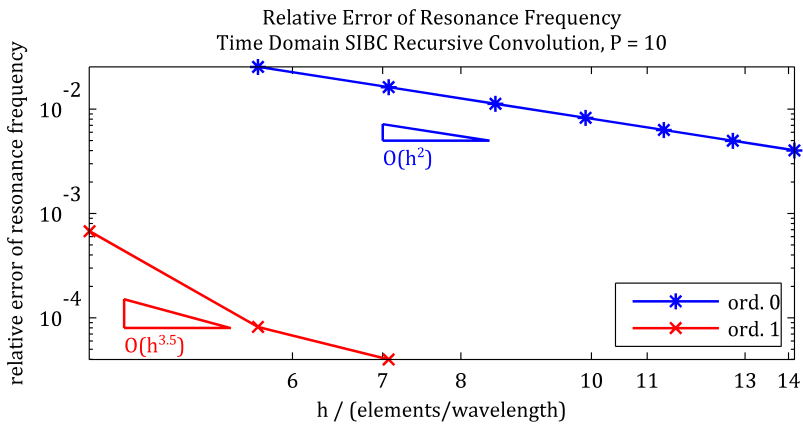


Figure 5.15.: Relative error of the  $f_0$  of a resonator with  $\sigma = 5.8 \cdot 10^5 \text{S/m}$  and  $l = 1\text{m}$ . Orders 0-1 refer to basis function polynomial order, and the triangles indicate the convergence rates (see also Table 5.10). The mesh resolution  $h$  is 4.2-14.1 edges/wavelength, and the smallest reached relative error is  $4.0 \cdot 10^{-5}$ .

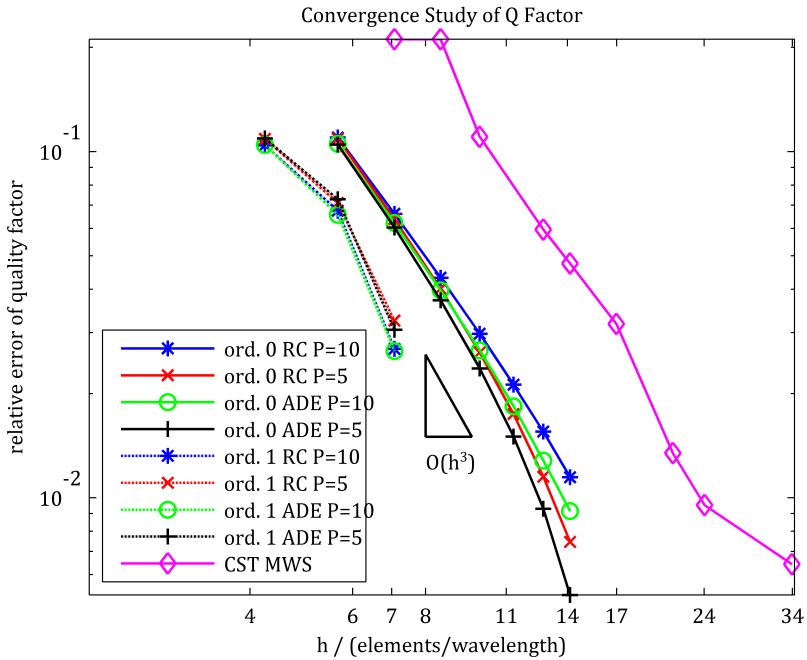


Figure 5.16.: Comparison of the relative errors of the Q factor between ADE and RC methods, as well as the Q factors calculated by CST Transient solver. The results are obtained by ADE and RC methods with  $P = 5$ , and  $P = 10$ , as well as basis function polynomial order 0 and 1. There is no significant difference in accuracy visible between the ADE and RC methods.

---

## 6 Summary

I would like to recall the research question placed in the introduction in Section 1: How to model dispersive surface impedance boundary conditions accurately and efficiently on a wide frequency band? The aim of the thesis is naturally to answer the question. To be more precise, the aim is to develop effective methods to model dispersive impedance boundary conditions on a wide frequency band at a single simulation run. Conventionally this is done in the time domain, which is also the case in this thesis. However, also a method to do this in the frequency domain is proposed in this thesis.

Additionally, the aim of this thesis is to model complex geometries accurately. Accurate modeling of problem geometry is considered by applying the developed schemes in DG-FEM method, which is by nature very efficient on modeling complex geometries. Another advantage of DG-FEM, especially from the point of view of this thesis, is that DG-FEM is very efficient tool for time domain simulations. The dispersive boundary conditions considered within this thesis include Standard Impedance Boundary Condition (SIBC) for modeling smooth conductor surfaces with high conductivity, Corrugated Surface Boundary Condition (CSBC) for modeling corrugated conducting surfaces, and Impedance Transmission Boundary Condition (ITBC) for modeling electrically thin conductive sheets.

---

### 6.1 Conclusion

---

As an answer to the research question, two schemes for modeling electromagnetic problems on a wide frequency band are proposed in this thesis, one in the frequency domain, another in the time domain. In the following, the proposed schemes are shortly summarized. The detailed descriptions of the methods, as well as validation and verification, are given in Chapter 4 for the frequency domain scheme, and in Chapter 5 for the time domain scheme. Additionally the frequency domain scheme is published by the author in [98], and both of the schemes are novel in computational electrical engineering, as far as the author is concerned.

#### 1. Wideband Iterative Eigenvalue Problem Solver

---

---

In Chapter 4, a novel method for solving electromagnetic EVP with dispersive boundary conditions on a wide frequency band in the frequency domain is proposed. The core of the proposed method is the following: At the initial iteration step, the linear and real EVP without dispersive boundary conditions is solved, to find out the frequency spectrum of the problem. After that, at every requested frequency, the value for the dispersive, complex impedance function is calculated, and a set of new, this time complex, EVPs are solved. However, as the impedance function is calculated separately at every requested frequency, and has a constant value at every eigenfrequency, the EVP is independent of frequency. Therefore, the EVP remains linear, i.e. although the dispersivity of the surface impedance function is considered, there is no need to solve for a nonlinear EVP.

The procedure is repeated iteratively for each requested resonance frequency, until a certain convergence tolerance is reached. This procedure enables solving for electromagnetic problems with taking into account the dispersivity of the impedance functions in the frequency domain. The proposed method is verified by several numerical examples and convergence studies for different impedance boundary conditions. The proposed scheme appears to be very accurate, as well as efficient, method for modeling impedance boundary conditions on a wide frequency band. Very small relative errors are achieved already with low mesh densities, and low-order basis functions. Additionally, only one iteration round is needed to reach the convergence.

## 2. Time Domain Scheme with Dispersive Impedance Boundary Conditions

The main contribution for this thesis is, as also the research question suggests, a scheme for solving electromagnetic problems on a wide frequency band in the time domain, with DG-FEM, and in the presence of dispersive impedance boundary conditions. The scheme is presented in Chapter 5 and the core of the method is the following: First, the dispersive impedance functions are approximated in the frequency domain as series of rational functions. The impedance boundary conditions are then transformed into the time domain by means of ADE and RC methods. Finally, a discrete time domain scheme is obtained by Verlet integration. The obtained time domain scheme is semi-implicit, i.e. the Maxwell's equations are solved

---

explicitly, and only the so called recursion terms, arising from dispersive boundary conditions, are solved semi-implicitly. Therefore, there is no need to invert matrices at every time step, and the obtained time stepping scheme is fast and efficient. The proposed schemes are verified by numerical examples convergence studies, and it appears to be efficient and accurate, already at very low mesh densities and basis function orders. Additionally, the RC and ADE methods are compared, and no significant difference in accuracy is found.

---

## 6.2 Outlook

---

In this section, further potential research topics related to this thesis are given. In this thesis, solely the surface impedance models, which exclude the tangential variation of the electromagnetic field within the conductor, are utilized. These first order models are suitable and accurate in most of the cases. However, when the lossy surfaces to be modeled have small radii of curvature, or the skin depths are large, first order surface impedance models may fail. Therefore, higher order surface impedance models, as e.g. [85] or [69], could be considered to model these cases. Also the time-stepping schemes utilized in this thesis, are of first order. The accuracy of surface impedance schemes in the time domain would increase by using higher order time stepping scheme.

In addition to modeling of surface impedance boundary conditions, the methods proposed in this thesis could be utilized also in other kind of boundary conditions. For example, modeling of open boundaries by means of ABC or PML. This would increase significantly also the applicability of the surface impedance boundary conditions presented in this thesis, as the open boundary conditions would consider the wide frequency band as well. This would also enable applying the modeling schemes proposed in this thesis to large-scale applications. In this thesis, the surface impedances are modeled by using RC and ADE methods, however, also e.g. Z-transform approach [5] could be utilized as well.

The approximations used for the impedance functions in the frequency domain in this thesis, are first order rational function, which correspond to the Drude model for dispersive medium. Also higher order rational functions could be considered, for example Debye [21] or Lorentz models [73], which would extend the frequency range. To improve the efficiency of the frequency domain scheme, the iterative EVP solver could be implemented in FEM, in addition to DG-FEM.

---

# A Appendix

Table A.1.: Fitting parameters for impedance approximation  $Z_{VF1}(\omega)$ .

$a_i$	$c_i$
$-7.0687 \cdot 10^{10}$	$6.0650 \cdot 10^7$
$-1.4025 \cdot 10^{10}$	$-1.0313 \cdot 10^7$
$-2.2052 \cdot 10^9$	$-9.0595 \cdot 10^4$
$-3.6552 \cdot 10^8$	$-2.1469 \cdot 10^4$
$-4.1419 \cdot 10^7$	$-636.3228$

Table A.2.: Fitting parameters for impedance approximation  $Z_{VF2}(\omega)$ .

$a_i$	$c_i$
$-2.3103 \cdot 10^{11}$	$3.2857 \cdot 10^9$
$-3.8421 \cdot 10^{10}$	$-4.5674 \cdot 10^7$
$-8.7509 \cdot 10^9$	$-2.4640 \cdot 10^5$
$-3.3219 \cdot 10^9$	$-3.4949 \cdot 10^5$
$-1.3361 \cdot 10^9$	$-2.9664 \cdot 10^4$
$-5.2621 \cdot 10^8$	$-1.9433 \cdot 10^4$
$-1.9898 \cdot 10^8$	$-2.4560 \cdot 10^3$
$-7.1435 \cdot 10^7$	$-979.8506$
$-2.3608 \cdot 10^7$	$-132.3637$
$-5.6763 \cdot 10^6$	$-39.2745$



Table A.3.: Fitting parameters for impedance approximation  $Z_{VF_3}(\omega)$ .

$a_i$	$c_i$
$-9.2882 \cdot 10^{11}$	$1.8990 \cdot 10^9$
$-1.0914 \cdot 10^{11}$	$-1.8060 \cdot 10^8$
$-1.6093 \cdot 10^{10}$	$-3.0600 \cdot 10^6$
$-2.0773 \cdot 10^9$	$-3.0930 \cdot 10^5$
$-1.3749 \cdot 10^8$	$-5.8229 \cdot 10^3$

Table A.4.: Fitting parameters for impedance approximation  $Z_{VF_4}(\omega)$ .

$a_i$	$c_i$
$-3.7963 \cdot 10^{12}$	$9.3930 \cdot 10^9$
$-2.0747 \cdot 10^{11}$	$-3.6732 \cdot 10^8$
$-5.2602 \cdot 10^{10}$	$-1.3078 \cdot 10^7$
$-1.7093 \cdot 10^{10}$	$-3.8621 \cdot 10^6$
$-5.4116 \cdot 10^9$	$-4.9225 \cdot 10^5$
$-1.5807 \cdot 10^9$	$-1.1154 \cdot 10^5$
$-4.1469 \cdot 10^8$	$-1.3410 \cdot 10^4$
$-9.4565 \cdot 10^7$	$-1.8841 \cdot 10^3$
$-1.7790 \cdot 10^7$	$-159.6650$
$-2.4306 \cdot 10^6$	$-11.0919$

Table A.5.: Fitting parameters for impedance approximation in numerical example in Section 5.5.2.1.

$a_i$	$c_i$
$-6.1469 \cdot 10^{12}$	$1.9762 \cdot 10^{11}$
$-1.2654 \cdot 10^{12}$	$-3.4602 \cdot 10^{10}$
$-2.4365 \cdot 10^{11}$	$-2.7490 \cdot 10^8$
$-6.5410 \cdot 10^{10}$	$-1.3911 \cdot 10^8$
$-1.7243 \cdot 10^{10}$	$-1.1318 \cdot 10^7$
$-4.3163 \cdot 10^9$	$-2.0913 \cdot 10^6$
$-1.0185 \cdot 10^9$	$-2.0910 \cdot 10^5$
$-2.2532 \cdot 10^8$	$-2.5310 \cdot 10^4$
$-4.6291 \cdot 10^7$	$-2.3488 \cdot 10^3$
$-7.9307 \cdot 10^6$	$-220.0986$

---

# B Register

---

# List of Figures

2.1.	Illustration of boundary condition for $\vec{B}$ and $\vec{D}$ . . . . .	18
2.2.	Illustration of boundary condition for $\vec{H}$ and $\vec{E}$ . . . . .	19
2.3.	Reflection and refraction of an electromagnetic wave on an inter- face of two media. . . . .	24
2.4.	The effect of conductivity on the refraction angle. . . . .	28
2.5.	Wave refraction in a conductive medium. . . . .	29
3.1.	Finite element mesh element. . . . .	34
3.2.	Edge and face basis functions. . . . .	35
3.3.	FEM and DG-FEM basis functions. . . . .	36
4.1.	Skin effect approximation. . . . .	43
4.2.	Corrugated surface model of HCC approximation. . . . .	47
4.3.	Effect of surface roughness on impedance function. . . . .	48
4.4.	Attenuation of an electromagnetic wave in a conductive medium. . . . .	49
4.5.	A two-port transmission line. . . . .	50
4.6.	A thin conductive sheet. . . . .	52
4.7.	Domain $\Omega$ including a conductive region. . . . .	54
4.8.	A DG-FEM element interface on the boundary of conductive region. . . . .	56
4.9.	Domain $\Omega$ with a thin conductive sheet. . . . .	58
4.10.	Two DG-FEM elements separated with a thin conductive region. . . . .	59
4.11.	Flow chart of solving the nonlinear Eigenvalue Problem (EVP) as fixed point iteration. . . . .	63
4.12.	Energy distribution of a lossy resonator. . . . .	65
4.13.	A hexahedral mesh for SIBC simulations. . . . .	69
4.14.	Relative error of the Q factor of SIBC resonator in the frequency domain: $\sigma = 10^5\text{S/m}$ , $l = 10\text{m}$ . . . . .	70
4.15.	Relative error of the Q factor of SIBC resonator in the frequency domain: $\sigma = 10^7\text{S/m}$ , $l = 1\text{m}$ . . . . .	71
4.16.	Relative error of the Q factor of SIBC resonator in the frequency domain: $\sigma = 10^9\text{S/m}$ , $l = 1\text{m}$ . . . . .	71
4.17.	Relative error of the Q factor of SIBC resonator in the frequency domain: $\sigma = 10^9\text{S/m}$ , $l = 10\text{m}$ . . . . .	72

4.18. Relative error of the Q factor of SIBC resonator in the frequency domain: $\sigma = 10^5\text{S/m}$ , $l = 1\text{m}$ . . . . .	72
4.19. Relative error of the Q factor of CSBC resonator: $h_{\text{RMS}} = 0.5\delta$ . . .	74
4.20. Relative error of the Q factor of CSBC resonator: $h_{\text{RMS}} = \delta$ . . .	74
4.21. Relative error of the Q factor of CSBC resonator: $h_{\text{RMS}} = 2\delta$ . . .	75
4.22. The deviation between the ITBC and the SIBC approximations, basis function order 0. . . . .	78
4.23. The deviation between the ITBC and the SIBC approximations, basis function order 1. . . . .	79
4.24. A hexahedral mesh for ITBC simulations. . . . .	79
4.25. Relative error of $f_0$ of a ITBC resonator: $\sigma = 10^7\text{S/m}$ , $d = 1 \cdot 10^{-5}\text{m}$ . . . . .	81
4.26. Relative error of the Q factor of a ITBC resonator: $\sigma = 10^7\text{S/m}$ , $d = 1 \cdot 10^{-5}\text{m}$ . . . . .	81
4.27. Relative error of $f_0$ of a ITBC resonator: $\sigma = 10^7\text{S/m}$ , $d = 3 \cdot 10^{-5}\text{m}$ . . . . .	82
4.28. Relative error of the Q factor of a ITBC resonator: $\sigma = 10^7\text{S/m}$ , $d = 3 \cdot 10^{-5}\text{m}$ . . . . .	82
4.29. Relative error of $f_0$ of a ITBC resonator: $\sigma = 10^7\text{S/m}$ , $d = 6 \cdot 10^{-5}\text{m}$ . . . . .	83
4.30. Relative error of the Q factor of a ITBC resonator: $\sigma = 10^7\text{S/m}$ , $d = 6 \cdot 10^{-5}\text{m}$ . . . . .	83
5.1. The time signal and the spectrum of a lossless cubical cavity resonator. . . . .	86
5.2. The real parts of the analytic impedance function $Z(\omega)$ and vector fitting approximations. . . . .	90
5.3. The imaginary parts of the analytic impedance function $Z(\omega)$ and vector fitting approximations. . . . .	91
5.4. Prony's method for a high-loss and low-loss signals. . . . .	115
5.5. Time signal and corresponding spectrum of a resonator with edge length of 10cm and wall conductivity $5.8 \cdot 10^9\text{S/m}$ . . . . .	116
5.6. Time signal and corresponding spectrum of a resonator with edge length of 1m and wall conductivity $5.8 \cdot 10^9\text{S/m}$ . . . . .	116
5.7. Time signal and corresponding spectrum of a resonator with edge length of 10m and wall conductivity $5.8 \cdot 10^9\text{S/m}$ . . . . .	117
5.8. Relative error of the Q factor of SIBC resonator in the time domain (ADE P = 5): $\sigma = 5.8 \cdot 10^5\text{S/m}$ , $l = 1\text{m}$ . . . . .	117
5.9. Relative error of $f_0$ of SIBC resonator in the time domain (ADE P = 5): $\sigma = 5.8 \cdot 10^5\text{S/m}$ , $l = 1\text{m}$ . . . . .	118
5.10. Relative error of the Q factor of SIBC resonator in the time domain (ADE P = 10): $\sigma = 5.8 \cdot 10^5\text{S/m}$ , $l = 1\text{m}$ . . . . .	118

---

5.11. Relative error of $f_0$ of SIBC resonator in the time domain (ADE P = 10): $\sigma = 5.8 \cdot 10^5 \text{S/m}$ , $l = 1\text{m}$ . . . . .	119
5.12. Relative error of the Q factor of SIBC resonator in the time domain (RC P = 5): $\sigma = 5.8 \cdot 10^5 \text{S/m}$ , $l = 1\text{m}$ . . . . .	119
5.13. Relative error of $f_0$ of SIBC resonator in the time domain (RC P = 5): $\sigma = 5.8 \cdot 10^5 \text{S/m}$ , $l = 1\text{m}$ . . . . .	120
5.14. Relative error of the Q factor of SIBC resonator in the time domain (RC P = 10): $\sigma = 5.8 \cdot 10^5 \text{S/m}$ , $l = 1\text{m}$ . . . . .	120
5.15. Relative error of $f_0$ of SIBC resonator in the time domain (RC P = 10): $\sigma = 5.8 \cdot 10^5 \text{S/m}$ , $l = 1\text{m}$ . . . . .	121
5.16. Comparison of ADE and RC methods. . . . .	122

---

## Acronyms

---

ABC	Absorbing Boundary Condition
ADE	Auxiliary Differential Equation
CPU	Central Processing Unit
CS	Corrugated Surfaces
CSBC	Corrugated Surface Boundary Condition
CV	Coefficient of Variation
DG-FEM	Discontinuous Galerkin Finite Element Method
DoF	Degree of Freedom
EVP	Eigenvalue Problem
FD	Frequency Domain
FDTD	Finite-Difference Time-Domain Method
FEM	Finite Element Method
FIT	Finite Integration Technique
FVM	Finite Volume Method
HCC	Hammerstad's Correction Coefficient
ITBC	Impedance Transmission Boundary Condition
MoM	Method of Moments

---

---



---

PDE	Partial Differential Equation
PEC	Perfect Electric Conductor
PML	Perfectly Matched Layer
RC	Recursive Convolution
RMS	Root Mean Square
SIBC	Standard Impedance Boundary Condition
TD	Time Domain

---

## List of Symbols

---



---

### Latin Alphabet

---

$a$	auxiliary variable
$a$	constant
$\mathbf{A}$	EVP matrix
$\vec{A}$	vector field
$a_i, a_{i1}, a_{i2}, a_{i3}, a_{i4}$	vector fitting parameters
$A_i$	amplitude of the frequency component $i$ in Prony's method
$\mathcal{A}_i, \vec{\mathcal{A}}_i$	ADE method auxiliary variables
$b$	auxiliary variable
$b$	constant
$\mathbf{B}$	EVP matrix
$\vec{B}$	magnetic flux density
$\vec{B}$	vector field
$c$	speed of light
$\mathbf{C}_B, \mathbf{C}_D, \mathbf{C}_Z, \mathbf{C}_{Z1}, \mathbf{C}_{Z2}$	curl matrices
$\mathbf{C}'_B, \mathbf{C}'_D, \mathbf{C}'_Z$	modified curl matrices
$c_i, c_{i1}, c_{i2}, c_{i3}, c_{i4}$	vector fitting parameters
$d$	distance of the ports of a transmission line

---

$d$	thickness of a thin conductive sheet
$\vec{D}$	electric displacement field
$\mathbf{e}$	vector of electric field degrees of freedom
$\vec{E}$	electric field strength
$\vec{E}, \vec{E}^+, \vec{E}^-, \vec{E}^*$	approximative electric field
$\vec{E}_0$	amplitude of the electric field
$\vec{E}_0, \vec{E}_d$	electric fields on opposite faces of a thin sheet
$\vec{E}_{10}, \vec{E}_{10}', \vec{E}_{20}, \vec{E}_{x0}$	amplitude of the electric field
$\vec{E}_1, \vec{E}_{1'}, \vec{E}_2$	electric field
$e_i, e_{i+1}$	finite elements
$e^{ip}$	electric degree of freedom
$\mathbf{e}^n$	electric degree of freedom at time step $n\Delta t$
$\mathbf{e}_t$	vector of tangential electric field degrees of freedom
$E_x, E_y, E_z$	electric field components in cartesian coordinates
$\vec{E}_t, \vec{E}_x$	tangential electric field
$f, F$	functions
$f_0$	fundamental frequency of a resonator
$f_{0,\text{ref.}}$	reference fundamental frequency of a resonator
$f_i$	resonance frequency
$g, G$	functions
$h$	height of a cylinder
$h$	mesh resolution
$\mathbf{h}$	vector of magnetic field degrees of freedom
$\vec{H}$	magnetic field strength
$\vec{H}, \vec{H}^+, \vec{H}^-, \vec{H}^*$	approximative magnetic field
$h^{ip}$	magnetic degree of freedom
$\mathbf{h}^n$	magnetic degree of freedom at time step $n\Delta t$
$\mathbf{H}(\text{curl}), \mathbf{H}(\text{div})$	function spaces
$\vec{H}_0, \vec{H}_d$	magnetic fields on opposite faces of a thin sheet
$h_{\text{RMS}}$	RMS height of surface corrugations
$\vec{H}_t$	tangential magnetic field

$H_x, H_y, H_z$	magnetic field components in cartesian coordinates
$i$	index
$\hat{i}$	unit vector in Cartesian coordinates
$I$	electric current
$I, I_1, I_2$	inputs of a function
$I_1, I_2$	electric currents into the ports 1 and 2 of a transmission line
$I(z)$	current over a transmission line
$j$	imaginary unit
$j$	index
$\hat{j}$	unit vector in Cartesian coordinates
$\vec{J}$	total current density
$\vec{J}_f$	free current density
$j_s$	surface current density
$k$	wave number
$\vec{k}$	wave vector
$\hat{k}$	unit vector in Cartesian coordinates
$K$	correction coefficient
$K_{\text{HCC}}$	Hammerstad's correction coefficient
$k_1, k_1', k_2$	wave numbers of incident, reflected, and refracted waves
$\vec{k}_1, \vec{k}_1', \vec{k}_2$	wave vectors of incident, reflected, and refracted waves
$l$	edge length of a cubical cavity resonator
$L$	number of frequency components in Prony's approximation
$\mathbf{L}$	PDE operator
$\mathcal{L}$	Laplace operator
$l_e$	dimension of a finite element
$l_x, l_y, l_z$	edge lengths of rectangular cavity resonator
$\vec{M}$	magnetization field



---

$\mathbf{M}_\mu, \mathbf{M}_\varepsilon$	mass matrices
$N$	number of time steps
$N$	number of frequency points in impedance approximation
$\vec{n}, \vec{n}_1, \vec{n}_{1'}, \vec{n}_2, \vec{n}_0, \vec{n}_d$	normal vectors
$N, N_E, N_H$	numbers of degrees of freedom
$N_e$	number of mesh elements
$O, O_1, O_2$	outputs of a function
$O(h), O(\delta), O(\Delta t)$	error of a numerical method
$p$	auxiliary variable
$p$	polynomial order index
$P$	number of interpolants in vector fitting method
$\mathcal{P}$	maximum basis function polynomial order
$\vec{P}$	polarization field
$q$	auxiliary variable
$q$	index
$Q, Q_{\text{rough}}$	quality factors
$Q_{\text{ref.}}$	reference quality factor
$r$	auxiliary variable
$\vec{r}$	position vector
$R$	residual
$R$	response function
$\vec{r}_0$	position vector on the interface
$\mathbb{R}^3$	three-dimensional euclidean space of real numbers
$\mathcal{R}_i, \vec{\mathcal{R}}_i$	RC method auxiliary variables
$R_{\text{min}}$	minimum radius of a conductor for skin effect approximation
$R_S$	surface resistance
$s$	complex variable
$\vec{S}$	Poynting's vector

---

$S, S_{\text{core}}, S_{\text{bottom}}, S_{\text{top}}$	surfaces
$t$	temporal variable
$T$	end of time interval
$t_0$	time instant zero
$t_{\text{min}}$	minimum thickness of a conductor for skin effect approximation
$U, U_{\text{max}}, U_{\text{half}}$	electromagnetic energy stored in a resonator
$U_0$	initial electromagnetic energy stored in a resonator
$u_j$	degrees of freedom
$u(x)$	a solution of a PDE
$\tilde{u}(x)$	an approximative solution of a PDE
$u(t)$	Heaviside step function
$V$	volume
$V_1, V_2$	voltages across the ports 1 and 2 of a transmission line
$V(z)$	voltage across a transmission line
$W$	energy stored in electromagnetic field
$w_i(x)$	weight function
$x, x_1, x_2$	spatial variable
$x(t)$	time domain signal
$y$	spatial variable
$z$	spatial variable
$Z$	standard impedance function
$\bar{Z}$	characteristic impedance of a transmission line
$\bar{Z}$	mean value of standard impedance function
$Z', Z'_i$	modified standard impedance function
$Z_0$	initial guess for impedance
$Z_{11}, Z_{12}$	surface and transmission impedance function of ITBC approximation
$z_{11}, z_{12}, z_{21}, z_{22}$	impedance parameters

---

$Z_{\text{HCC}}$	impedance function of a corrugated surface
$Z_{\text{rough}}$	impedance function of a corrugated surface
$Z_{\text{VF}}, Z_{\text{VF1}},$	impedance approximations
$Z_{\text{VF2}}, Z_{\text{VF3}}, Z_{\text{VF4}}$	

---

## Greek Alphabet

---

$\alpha$	constant
$a$	abscissa of convergence
$\alpha, \alpha_1, \alpha_2, \alpha_{\text{rough}}$	attenuation constants
$\beta$	constant
$\beta, \beta_1, \beta_2$	propagation constants
$\gamma$	auxiliary variable
$\gamma$	penalization factor
$\Gamma$	half-power-width
$\Gamma_{\text{C}}, \Gamma_{\text{S}}, \Gamma_{\text{T}}$	boundaries of computational domain
$\delta$	skin depth
$\delta_0$	skin depth at the fundamental frequency of a resonator
$\delta_{ij}$	Kronecker delta function
$\Delta$	thickness of a layer to which the electromagnetic field is confined in a conductor
$\Delta_{\text{CV}}$	coefficient of deviation, "relative RMS error"
$\Delta_{\text{max}}$	maximum relative deviation
$\Delta_{\text{rel}}, \Delta_{\text{Q, rel}}, \Delta_{\text{f, rel.}}$	relative deviation
$\Delta t$	time step
$\Delta\omega$	transition of angular frequency due to losses in a resonator
$\epsilon, \epsilon_0, \epsilon_r$	total, free space, and relative permittivities
$\epsilon_1, \epsilon_2$	permittivities
$\epsilon_j$	permittivity associated to $j^{\text{th}}$ DG-FEM degree of freedom
$\zeta_{1i}^{\text{A}}, \zeta_{2i}^{\text{A}}$	ADE method coefficients

---

$\zeta_{1i}^R, \zeta_{2i}^R, \zeta_{3i}^R$	RC method coefficients
$\eta_0$	free space impedance
$\theta_1, \theta_{1'}, \theta_2$	angles of incidence, reflection, and refraction
$\lambda$	wavelength
$\mu, \mu_0, \mu_r$ $\mu_1, \mu_2$ $\mu_j$	total, free space, and relative permeabilities permeabilities permeability associated to $j^{\text{th}}$ DG-FEM degree of freedom
$\rho, \rho_f$	total and free charge densities
$\sigma$	electrical conductivity
$\sigma_i$	damping factor of the frequency component $i$ in Prony's method
$\sigma_s$	surface charge density
$\tau$	temporal variable
$\varphi_i$	amplitude of the frequency component $i$ in Prony's method
$\varphi_j, \varphi_E^{ip}, \varphi_H^{ip}$	basis functions
$\chi_e, \chi_m$	electrical and magnetic susceptibility
$\Psi$	angle of propagation in a conductive medium
$\omega$	angular frequency
$\Omega$	domain
$\omega_0$	fundamental angular frequency of a resonator
$\omega_i$	$i^{\text{th}}$ eigenfrequency

---

# Bibliography

- [1] F. Alessandri, G. Baini, G. D’Inzeo, and R. Sorrentino, “Propagation characteristics of lossy distributed gaas fet structures,” in *Microwave Symposium Digest, 1992.*, IEEE MTT-S International, vol. 2, June 1992, pp. 963–966. (Cited on page 10.)
- [2] J. Alvarez, L. Angulo, A. Bretones, and S. Garcia, “A spurious-free discontinuous galerkin time-domain method for the accurate modeling of microwave filters,” *Microwave Theory and Techniques, IEEE Transactions on*, vol. 60, no. 8, pp. 2359–2369, 2012. (Cited on page 10.)
- [3] G. Antonini and A. Orlandi, “Time domain modeling of lossy and dispersive thin layers,” *Microwave and Wireless Components Letters, IEEE*, vol. 17, no. 9, pp. 631–633, 2007. (Cited on page 11.)
- [4] S. Ausserhofer, O. Biro, and K. Preis, “Discontinuous galerkin finite elements in time domain eddy-current problems,” *Magnetics, IEEE Transactions on*, vol. 45, no. 3, pp. 1300–1303, 2009. (Cited on page 11.)
- [5] J. Beggs, “A fdtd surface impedance boundary condition using z-transforms,” *Applied Comp. Electromagn. Society Journal*, vol. 13, no. 3, pp. 14 – 24, 1998. (Cited on pages 11 and 125.)
- [6] J. Beggs, R. Luebbers, K. Kunz, and K. Yee, “Wideband finite difference time domain implementation of surface impedance boundary conditions for good conductors,” in *Antennas and Propagation Society International Symposium, 1991. AP-S. Digest*, vol. 1, 1991, pp. 406–409. (Cited on page 11.)
- [7] R. Burden and J. Faires, *Numerical Analysis*, 7th ed. Brooks/Cole-Thomson Learning, 2001. (Cited on pages 69, 73, 80, 111, and 112.)
- [8] J. Butcher, *Numerical Methods for Ordinary Differential Equations*. Wiley, 2003. (Cited on page 97.)
- [9] Y. Cai, “Faster 3d finite element time domain - floquet absorbing boundary condition modelling using recursive convolution and vector fitting,” *IET*

- 
- Microwaves, Antennas & Propagation, vol. 3, pp. 310–324, March 2009. (Cited on page 11.)
- [10] N. Canouet, L. Fezoui, and S. Piperno, “Discontinuous Galerkin time-domain solution of Maxwell’s equations on locally-refined nonconforming Cartesian grids,” *COMPEL: Int J for Computation and Maths. in Electrical and Electronic Eng.*, vol. 24, no. 4, pp. 1381–1401, April 2005. (Cited on page 38.)
- [11] S. Celozzi and M. Feliziani, “Time domain finite element simulation of conductive regions,” *Magnetics, IEEE Transactions on*, vol. 29, no. 2, pp. 1705–1710, March 1993. (Cited on page 52.)
- [12] —, “Transient scattering problems solution by surface equivalent sources,” *Magnetics, IEEE Transactions on*, vol. 30, no. 5, pp. 3148–3151, 1994. (Cited on page 11.)
- [13] J. Chen, Q.-H. Liu, M. Chai, and J. Mix, “A nonspurious 3-d vector discontinuous galerkin finite-element time-domain method,” *Microwave and Wireless Components Letters, IEEE*, vol. 20, no. 1, pp. 1–3, 2010. (Cited on page 10.)
- [14] Q. Chen, Y. Hong, and R. Temam, “Analysis of a penalty method,” *Journal of Scientific Computing*, vol. 53, no. 1, pp. 3–34, 2012. (Cited on page 10.)
- [15] X. Chen, “Em modeling of microstrip conductor losses including surface roughness effect,” *Microwave and Wireless Components Letters, IEEE*, vol. 17, no. 2, pp. 94–96, 2007. (Cited on page 10.)
- [16] P. Clarricoats, “Low attenuation in corrugated circular waveguides,” *Electronics Letters*, vol. 9, pp. 376–377, August 1973. (Cited on page 10.)
- [17] B. Cockburn, G. Karniadakis, and C. Shu, *Discontinuous Galerkin Methods: Theory, Computation, and Applications*, ser. *Lecture Notes in Computational Science and Engineering*. Springer-Verlag, 2000. (Cited on page 9.)
- [18] B. Cockburn and C.-W. Shu, “The runge-kutta discontinuous galerkin method for conservation laws v: Multidimensional systems,” *Journal of Computational Physics*, vol. 141, no. 2, pp. 199 – 224, 1998. (Cited on page 9.)

- 
- [19] B. Davies, *Integral Transforms and Their Applications*, ser. APPLIED MATHEMATICAL SCIENCES. Springer, 2002. (Cited on pages 93 and 109.)
- [20] V. De Santis, S. Cruciani, M. Feliziani, and M. Okoniewski, “Efficient low order approximation for surface impedance boundary conditions in finite-difference time-domain method,” *Magnetics, IEEE Transactions on*, vol. 48, no. 2, pp. 271–274, 2012. (Cited on page 11.)
- [21] P. Debye, “Zur theorie der spezifischen wÄd'rme,” *Annalen der Physik*, vol. 4, no. 39, pp. 789–839, 1912. (Cited on page 125.)
- [22] D. Deschrijver, M. Mrozowski, T. Dhaene, and D. De Zutter, “Macro-modeling of multiport systems using a fast implementation of the vector fitting method,” *Microwave and Wireless Components Letters, IEEE*, vol. 18, no. 6, pp. 383–385, June 2008. (Cited on page 87.)
- [23] S. Dosopoulos and J. F. Lee, “Interior penalty discontinuous galerkin method for the time-domain maxwell’s equations,” *Magnetics, IEEE Transactions on*, vol. 46, no. 8, pp. 3512–3515, 2010. (Cited on page 10.)
- [24] P. Drude, “Zur elektronentheorie der metalle,” *Annalen der Physik*, vol. 3, no. 306, pp. 566–613, 1900. (Cited on page 87.)
- [25] R. Ehlers and A. Metaxas, “3-d discontinuous sheet for finite-element time-domain modelling of thin metallic films,” *Science, Measurement and Technology, IEE Proceedings*, September 2002. (Cited on page 10.)
- [26] —, “3-d fe discontinuous sheet for microwave heating,” *Microwave Theory and Techniques, IEEE Transactions on*, vol. 51, no. 3, pp. 718 – 726, March 2003. (Cited on page 10.)
- [27] R. Elliott, “On the theory of corrugated plane surfaces,” *Antennas and Propagation, Transactions of the IRE Professional Group on*, vol. 2, no. 2, pp. 71 – 81, April 1954. (Cited on page 10.)
- [28] N. Farahat, S. Yuferev, and N. Ida, “High order surface impedance boundary conditions for the fdtd method,” *Magnetics, IEEE Transactions on*, vol. 37, no. 5, pp. 3242–3245, 2001. (Cited on page 11.)
- [29] O. P. Gandhi, B.-Q. Gao, and J.-Y. Chen, “A frequency-dependent finite-difference time-domain formulation for general dispersive media,” *Microwave Theory and Techniques, IEEE Transactions on*, vol. 41, no. 4, pp. 658–665, 1993. (Cited on page 11.)

- 
- [30] S. Gedney, T. Kramer, C. Luo, J. Roden, R. Crawford, B. Guernsey, J. Beggs, and J. Miller, “The discontinuous galerkin finite element time domain method (dgfetd),” in *Electromagnetic Compatibility, 2008. EMC 2008. IEEE International Symposium on, 2008*, pp. 1–4. (Cited on page 11.)
- [31] S. Gedney, J. Young, T. Kramer, and J. Roden, “A discontinuous galerkin finite element time-domain method modeling of dispersive media,” *Antennas and Propagation, IEEE Transactions on*, vol. 60, no. 4, pp. 1969–1977, 2012. (Cited on pages 11 and 96.)
- [32] S. Gedney and B. Zhao, “An auxiliary differential equation formulation for the complex-frequency shifted pml,” *Antennas and Propagation, IEEE Transactions on*, vol. 58, no. 3, pp. 838–847, 2010. (Cited on page 11.)
- [33] E. Gjonaj and T. Weiland, “A projection penalization approach for the high order dg-fem in the time domain,” in *Electromagnetic Theory (EMTS), 2010 URSI International Symposium on, 2010*, pp. 981–984. (Cited on pages 10, 39, and 110.)
- [34] E. Gjonaj, T. Lau, F. Wolfheimer, S. Schnepf, and T. Weiland, “Accurate modelling of charged particle beams in linear accelerators,” *New Journal of Physics*, vol. 8, no. 11, p. 285, 2006. (Cited on page 38.)
- [35] N. Godel, S. Lange, and M. Clemens, “Time domain discontinuous galerkin method with efficient modelling of boundary conditions for simulations of electromagnetic wave propagation,” in *Electromagnetic Compatibility and 19th International Zurich Symposium on Electromagnetic Compatibility, 2008. APEMC 2008. Asia-Pacific Symposium on, 2008*, pp. 594–597. (Cited on page 11.)
- [36] S. Groiss, I. Bardi, O. Biro, K. Preis, and K. Richter, “Parameters of lossy cavity resonators calculated by the finite element method,” *Magnetics, IEEE Transactions on*, vol. 32, no. 3, pp. 894–897, May 1996. (Cited on pages 10 and 46.)
- [37] B. Gustavsen, “The vector fitting web site,” <http://www.energy.sintef.no/Produkt/VECTFIT/>, 1998, cited on 15.7.2013. (Cited on page 87.)
- [38] —, “Improving the pole relocating properties of vector fitting,” *Power Delivery, IEEE Transactions on*, vol. 21, no. 3, pp. 1587–1592, July 2006. (Cited on page 87.)



- 
- [39] B. Gustavsen and A. Semlyen, “Rational approximation of frequency domain responses by vector fitting,” *Power Delivery, IEEE Transactions on*, vol. 14, no. 3, pp. 1052–1061, July 1999. (Cited on page 87.)
- [40] J. Gustincic, “A general power loss method for attenuation of cavities and waveguides,” *Microwave Theory and Techniques, IEEE Transactions on*, vol. 11, no. 1, pp. 83–87, 1963. (Cited on pages 65 and 105.)
- [41] J. Gyselinck, R. Sabariego, P. Dular, and C. Geuzaine, “Time-domain finite-element modeling of thin electromagnetic shells,” *Magnetics, IEEE Transactions on*, vol. 44, no. 6, pp. 742–745, June 2008. (Cited on page 11.)
- [42] M. Ha and M. Swaminathan, “A laguerre-fdtd formulation for frequency-dependent dispersive materials,” *Microwave and Wireless Components Letters, IEEE*, vol. 21, no. 5, pp. 225–227, 2011. (Cited on page 11.)
- [43] S. Hall, S. Pytel, P. Huray, D. Hua, A. Moonshiram, G. Brist, and E. Sijercic, “Multigigahertz causal transmission line modeling methodology using a 3-d hemispherical surface roughness approach,” *Microwave Theory and Techniques, IEEE Transactions on*, vol. 55, no. 12, pp. 2614–2624, December 2007. (Cited on page 10.)
- [44] E. Hammerstad, F. Bekkadal, ELAB., NTH., and SINTEF., *Microstrip Handbook*, ser. Trondheim. Norges tekniske høyskole, Elektronikklaboratoriet. ELAB rapport, 1975. (Cited on pages 10, 11, and 47.)
- [45] J. Hauer, C. Demeure, and L. Scharf, “Initial results in prony analysis of power system response signals,” *Power Systems, IEEE Transactions on*, vol. 5, no. 1, pp. 80–89, 1990. (Cited on page 106.)
- [46] J. S. Hesthaven, “Spectral penalty methods,” *Applied Numerical Mathematics*, vol. 33, no. 1-4, pp. 23–41, 2000. (Cited on pages 10 and 39.)
- [47] J. S. Hesthaven and T. Warburton, “Nodal high-order methods on unstructured grids,” *J. Comput. Phys.*, vol. 181, no. 1, pp. 186–221, 2002. (Cited on pages 9 and 37.)
- [48] —, *Nodal Discontinuous Galerkin Methods: Algorithms, Analysis, and Applications*, 1st ed. Springer Publishing Company, Incorporated, 2007. (Cited on pages 9 and 33.)

- 
- [49] C. Holloway and E. F. Kuester, “Impedance-type boundary conditions for a periodic interface between a dielectric and a highly conducting medium,” *Antennas and Propagation, IEEE Transactions on*, vol. 48, no. 10, pp. 1660–1672, 2000. (Cited on page 10.)
- [50] R. Horton, “Variation of microstrip losses with thickness of strip,” *Electronics Letters*, vol. 7, pp. 490–491(1), August 1971. (Cited on pages 10, 11, 49, and 51.)
- [51] N. Ida, L. Y., and H. T, “High order surface impedance boundary conditions with the  $a\text{-}\varphi$  formulation,” *Facta Univ. Ser.: Elec. Energ.*, vol. 24, no. 2, pp. 147 – 155, August 2011. (Cited on pages 10 and 46.)
- [52] J. Jackson, C. Witte, and K. Müller, *Klassische Elektrodynamik*, 4th ed. Walter De Gruyter Incorporated, 2006. (Cited on pages 64 and 65.)
- [53] J.-M. Jin, J. Volakis, C. L. Yu, and A. Woo, “Modeling of resistive sheets in finite element solutions [em scattering],” *Antennas and Propagation, IEEE Transactions on*, vol. 40, no. 6, pp. 727–731, 1992. (Cited on page 11.)
- [54] J. Jin, *The Finite Element Method in Electromagnetics*, ser. A Wiley-Interscience publication. Wiley, 2002. (Cited on page 33.)
- [55] M. Karkkainen, “FDTD surface impedance model for coated conductors,” *Electromagnetic Compatibility, IEEE Transactions on*, vol. 46, no. 2, pp. 222–233, 2004. (Cited on page 11.)
- [56] S. Koch, J. Trommler, H. De Gersem, and T. Weiland, “Modeling thin conductive sheets using shell elements in magnetoquasistatic field simulations,” *Magnetics, IEEE Transactions on*, vol. 45, no. 3, pp. 1292–1295, 2009. (Cited on page 11.)
- [57] M. Kunze, “Surface impedances for planar conductors in volume discretization methods without frequency limitations,” in *Microwave Conference (GeMIC), 2011 German, 2011*, pp. 1–4. (Cited on page 11.)
- [58] T. Lau, E. Gjonaj, and T. Weiland, “Investigation of higher order symplectic time integration methods for discontinuous galerkin methods with a centered flux,” in *Computational Electromagnetics in Time-Domain, 2007. CEM-TD 2007. Workshop on, 2007*, pp. 1–4. (Cited on page 39.)

- 
- [59] M. A. Leontovich, "On the approximate boundary conditions for electromagnetic fields on the surface of well conducting bodies," *Investigations of Propagation of RadioWaves*, B. A. Vvdensky, Ed. Moscow, Russia: Academy of Sci. USSR, pp. 5–20, 1948. (Cited on page 10.)
- [60] M. Li, Z. Shen, J. Zou, and J. Yuan, "Applicability of the standard impedance boundary condition in the calculation of 3d eddy current loss in conductors," in *Electromagnetic Field Problems and Applications (ICEF)*, 2012 Sixth International Conference on, 2012, pp. 1–2. (Cited on page 11.)
- [61] T. Liang, S. Hall, H. Heck, and G. Brist, "A practical method for modeling pcb transmission lines with conductor surface roughness and wideband dielectric properties," in *Microwave Symposium Digest, 2006. IEEE MTT-S International*, 2006, pp. 1780–1783. (Cited on page 10.)
- [62] H. Lin, R. Wang, and G. Wang, "Novel weakly conditionally stable fdtd scheme based on trapezoidal recursive convolution for modeling dispersive media," in *Microwave Technology and Computational Electromagnetics*, 2009. ICMTCE. International Conference on, 2009, pp. 418–421. (Cited on page 11.)
- [63] M.-S. Lin, C.-M. Lin, R.-B. Wu, and C. Chen, "Transient propagation in anisotropic laminated composites," *Electromagnetic Compatibility, IEEE Transactions on*, vol. 35, no. 3, pp. 357–365, August 1993. (Cited on page 10.)
- [64] R. Luebbers and F. Hunsberger, "Fdtd for nth-order dispersive media," *Antennas and Propagation, IEEE Transactions on*, vol. 40, no. 11, pp. 1297–1301, 1992. (Cited on page 11.)
- [65] M. Lukic and D. Filipovic, "Modeling of 3-d surface roughness effects with application to  $\mu$ -coaxial lines," *Microwave Theory and Techniques, IEEE Transactions on*, vol. 55, no. 3, pp. 518–525, 2007. (Cited on page 10.)
- [66] R. Makinen, H. De Gersem, T. Weiland, and M. Kivikoski, "Modeling of lossy curved surfaces in 3-d fit/fdtd techniques," *Antennas and Propagation, IEEE Transactions on*, vol. 54, no. 11, pp. 3490–3498, 2006. (Cited on page 11.)
- [67] J. Maloney and G. Smith, "The efficient modeling of thin material sheets in the finite-difference time-domain (fdtd) method," *Antennas and Prop-*

- 
- agation, IEEE Transactions on, vol. 40, no. 3, pp. 323–330, March 1992. (Cited on page 11.)
- [68] J. E. Marsden and T. S. Ratiu, Introduction to Mechanics and Symmetry, 2nd ed., ser. Texts in Applied Mathematics. New York, NY: Springer-Verlag, 1999, no. 17. (Cited on page 39.)
- [69] K. Mitzner, “An integral equation approach to scattering from a body of finite conductivity,” Radio Science, vol. 2, pp. 1459–1470, 1967. (Cited on pages 10 and 125.)
- [70] S. P. Morgan, “Effect of surface roughness on eddy current losses at microwave frequencies,” Journal of Applied Physics, vol. 20, no. 4, pp. 352–362, April 1949. (Cited on pages 10 and 47.)
- [71] K. S. Oh and J. Schutt-Aine, “An efficient implementation of surface impedance boundary conditions for the finite-difference time-domain method,” Antennas and Propagation, IEEE Transactions on, vol. 43, no. 7, pp. 660–666, 1995. (Cited on pages 11, 94, and 96.)
- [72] A. Oppenheim, A. Willsky, and S. Nawab, Signals and Systems, ser. Prentice Hall Signal Processing Series. Prentice Hall, 1997. (Cited on page 92.)
- [73] K. Oughstun and N. Cartwright, “On the lorentz-lorenz formula and the lorentz model of dielectric dispersion,” Opt. Express, vol. 11, no. 13, pp. 1541–1546, Jun 2003. (Cited on page 125.)
- [74] S. Piperno, “Symplectic local time-stepping in non-dissipative dgtd methods applied to wave propagation problems,” INRIA, Tech. Rep. RR-5643. (Cited on pages 39 and 40.)
- [75] G. R. B. Prony, “Essai experimental et analytique sur les lois de la dilatabilite de fluides elastiques et sur celles de la force expansive de la vapeur de l’alkoal, a differentes temperatures,” l’Ecole Polytech., vol. VI, pp. 24–76, 1795. (Cited on page 106.)
- [76] O. Ramadan, “Auxiliary differential equation formulation: an efficient implementation of the perfectly matched layer,” Microwave and Wireless Components Letters, IEEE, vol. 13, no. 2, pp. 69–71, 2003. (Cited on page 11.)

- 
- [77] B. Ramdane, D. Trichet, M. Belkadi, T. Saidi, and J. Fouladgar, "Electromagnetic and thermal modeling of composite materials using multilayer shell elements," in *Electromagnetic Field Computation (CEFC), 2010 14th Biennial IEEE Conference on*, 2010, pp. 1–1. (Cited on page 11.)
- [78] S. Ramo, J. Whinnery, and T. van Duzer, *Fields and Waves in Communication Electronics*. (Cited on page 65.)
- [79] J. C. Rautio and V. Demir, "Microstrip conductor loss models for electromagnetic analysis," *Microwave Theory and Techniques, IEEE Transactions on*, vol. 51, no. 3, pp. 915–921, 2003. (Cited on page 10.)
- [80] J. Reitz, F. Milford, and R. Christy, *Foundations of electromagnetic theory*, ser. *Physics Series*. Addison-Wesley, 1979. (Cited on pages 13, 18, 19, 27, and 92.)
- [81] I. Rekanos, "FDTD schemes for wave propagation in davidson-cole dispersive media using auxiliary differential equations," *Antennas and Propagation, IEEE Transactions on*, vol. 60, no. 3, pp. 1467–1478, 2012. (Cited on page 11.)
- [82] Z. Ren, "Degenerated whitney prism elements-general nodal and edge shell elements for field computation in thin structures," *Magnetics, IEEE Transactions on*, vol. 34, no. 5, pp. 2547–2550, September 1998. (Cited on page 11.)
- [83] D. Riley and N. Riley, "First order models for thin-material sheets and coatings in the finite-element time-domain method," vol. 4, pp. 3489 – 3492, June 2004. (Cited on page 11.)
- [84] R. D. Ruth, "A Canonical Integration Technique," *IEEE Transactions on Nuclear Science*, vol. 30, no. 4, pp. 2669–2671, 1983. (Cited on page 39.)
- [85] S. Rytov, "Calculation of skin effect by perturbation method", *zhurnal experimental'noi i Teoreticheskoi Fiziki*, vol. 10, no. 2, pp. 180–189, 1940. (Cited on pages 10 and 125.)
- [86] M. Sarto, "A new model for the ftd analysis of the shielding performances of thin composite structures," *Electromagnetic Compatibility, IEEE Transactions on*, vol. 41, no. 4, pp. 298–306, 1999. (Cited on pages 10 and 11.)

- 
- [87] R. Schulz, V. Plantz, and D. Brush, “Shielding theory and practice,” *Electromagnetic Compatibility, IEEE Transactions on*, vol. 30, no. 3, pp. 187–201, August 1988. (Cited on page 10.)
- [88] T. B. A. Senior, “Impedance boundary conditions for imperfectly conducting surfaces,” *Applied Scientific Research, Section B*, vol. 8, pp. 418–436, 1960. (Cited on pages 10 and 11.)
- [89] Y. Shlepnev and C. Nwachukwu, “Roughness characterization for interconnect analysis,” in *Electromagnetic Compatibility (EMC), 2011 IEEE International Symposium on*, August 2011, pp. 518–523. (Cited on page 10.)
- [90] G. S. Smith, “On the skin effect approximation,” *American Journal of Physics*, vol. 58, no. 10, pp. 996–1002, 1990. (Cited on pages 10, 42, 43, 44, 48, and 76.)
- [91] J. A. Stratton, *Electromagnetic Theory*, 1st ed. McGraw-Hill Companies (New York), 1941. (Cited on pages 13, 24, 27, and 29.)
- [92] D. Sun, J. Manges, X. Yuan, and Z. Cendes, “Spurious modes in finite-element methods,” *Antennas and Propagation Magazine, IEEE*, vol. 37, no. 5, pp. 12–24, 1995. (Cited on pages 10 and 39.)
- [93] F. Teixeira, “Time-domain finite-difference and finite-element methods for maxwell equations in complex media,” *Antennas and Propagation, IEEE Transactions on*, vol. 56, no. 8, pp. 2150–2166, 2008. (Cited on page 11.)
- [94] L. Tsang, H. Braunisch, R. Ding, and X. Gu, “Random rough surface effects on wave propagation in interconnects,” *Advanced Packaging, IEEE Transactions on*, vol. 33, no. 4, pp. 839–856, November 2010. (Cited on page 10.)
- [95] S. Van Den Berghe, F. Olyslager, and D. De Zutter, “Accurate modeling of thin conducting layers in fdtd,” *Microwave and Guided Wave Letters, IEEE*, vol. 8, no. 2, pp. 75–77, 1998. (Cited on pages 10, 11, and 51.)
- [96] T. Weiland, “A discretization model for the solution of Maxwell’s equations for six-component fields,” *Archiv Elektronik und Uebertragungstechnik*, vol. 31, pp. 116–120, 1977. (Cited on page 9.)

- 
- [97] R. W.H. and T. Hill, “Triangular mesh methods for the neutron transport equation,” in Proceedings of the American Nuclear Society, 1973. (Cited on page 9.)
- [98] I. Woyna, E. Gjonaj, and T. Weiland, “Broadband surface impedance boundary conditions for the high order time domain discontinuous galerkin method,” *COMPEL: The International Journal for Computation and Mathematics in Electrical and Electronic Engineering*, vol. 33, no. 4, 2014, to be published. (Cited on pages 41, 53, 60, 85, and 123.)
- [99] K. Yee, “Numerical solution of initial boundary value problems involving maxwell’s equations in isotropic media,” *Antennas and Propagation, IEEE Transactions on*, vol. 14, no. 3, pp. 302–307, 1966. (Cited on page 9.)
- [100] S. Yuferev and L. Kettunen, “Implementation of high order surface impedance boundary conditions using vector approximating functions,” *Magnetics, IEEE Transactions on*, vol. 36, no. 4, pp. 1606–1609, 2000. (Cited on page 11.)
- [101] S. Zaglmayr, “High order finite element methods for electromagnetic field computation,” Ph.D. dissertation, Johannes Kepler University, Linz, Austria, 2006. (Cited on page 35.)
- [102] H.-X. Zheng and K.-W. Leung, “FDTD implementation and application of high order impedance boundary condition using rational functions,” *Antennas and Propagation, IEEE Transactions on*, vol. 57, no. 8, pp. 2397–2408, 2009. (Cited on page 11.)
- [103] O. Zienkiewicz, R. Taylor, and J. Zhu, *The finite element method*. Elsevier/Butterworth-Heinemann, 2005. (Cited on page 9.)

---

---

## Acknowledgement

---

This work is supported by the 'Excellence Initiative' of the German Federal and State Governments and the Graduate School of Computational Engineering at Technische Universität Darmstadt.

Additionally, finishing this thesis would not have been possible without support and help of several people and institutions. I would like to sincerely thank especially:

- Graduate School of Computational Engineering, not only for the financial support, but also for organizing numerous activities during my Ph.D. phase
- Prof. Dr.-Ing. Thomas Weiland for his support and help throughout the thesis work, and offering an excellent working environment at TEMF
- Prof. Dr.-Ing. Irina Munteanu for her support and help, and for being the co-referent of my Ph.D. thesis
- PD Dr.rer.nat. Erion Gjonaj for his support and excellent ideas and hints throughout my whole time in TEMF
- Adj. Prof. Riku Mäkinen (TU Tampere) for introducing me with the topic of my thesis, and with TEMF and Prof. Dr.-Ing. Thomas Weiland
- My colleagues and friends at TEMF and GSCE, especially M.Sc. Marija Nikolovski
- My friends in Finland and in Germany
- My mom Ulla-Maija, dad Olli, sister Maarit and her family, for the invaluable support
- My husband Lars and our son Samu, for giving a meaning to all of this



---

---

## Curriculum Vitae

---



Irene Kaarina Woyna (nee Hiltunen)  
Born 15.1.1983 in Tampere, Finland

### Education

08/90-06/91 Olkahisen koulu school, Tampere, Finland  
91-06/95 Tammelan koulu school, Tampere, Finland  
08/95-06/99 Tammerkosken koulu school, Tampere, Finland  
08/99-06/02 Tampereen lyseon lukio high school, Tampere, Finland  
06/02 Maturity exam, Tampereen lyseon lukio high school, Tampere, Finland

### Academic Studies

08/04-11/08 Electrical engineering, Tampere University of Technology, Tampere, Finland. Major subject Electromagnetism, minor subjects Technical Physics and Power Electronics.  
11/08 Master of Science in electrical engineering "with distinction". Master thesis subject "Electromagnetic Design of Electrically Controlled Switch", supervisor Prof. Lauri Kettunen.

### Employment

2007-2012 Teaching Assistant, Tampere University of Technology and TU Darmstadt.  
05/2007-12/2007 Tampere Municipal Electric Department, Tampere, Finland.

---

03/2008-10/2008 Research Assistant, Department of Electronics, Tampere University of Technology.

10/2008-03/2011 Researcher, Department of Electronics, Tampere University of Technology.

04/2011-10/2014 Wissenschaftliche Mitarbeiterin, Computational Electromagnetics Laboratory (TEMF), TU Darmstadt.

### Publications

2010 I. Hiltunen, A. Rasku, R. Makinen: "A Fully Automated Implementation of Conformal 3D Surface-Impedance Model for Finite-Difference Method", 2010 ACES Conference, The 26th Annual Review of Progress in Applied Computational Electromagnetics, Tampere, Finland, April 26th-29th, 2010, pp. 310-315.

2010 A. Rasku, H. Sillanpaa, I. Hiltunen, R. Makinen: "Multiline Material Parameter Extraction Method Performance Analysis", APMC 2010. 2010 Asia-Pacific Microwave Conference, December 7th-10th, 2010, Yokohama, Japan, pp. 1905-1908.

2012 I. Woyna, E. Gjonaj, T. Weiland: "Broadband Surface Impedance Boundary Conditions for Higher Order Time Domain Discontinuous Galerkin Method", SCEE2012, Scientific Computing in Electrical Engineering, September 11th-14th, Zurich, Switzerland.

2014 I. Woyna, E. Gjonaj, T. Weiland: "Broadband Surface Impedance Boundary Conditions for Higher Order Time Domain Discontinuous Galerkin Method", The international journal for computation and mathematics in electrical and electronic engineering, vol. 33(4), to be published.

### Awards

2012 Young Scientist Award at SCEE2012, Scientific Computing in Electrical Engineering, September 11th-14th, Zurich, Switzerland, for the contribution of "Broadband Surface Impedance Boundary Conditions for Higher Order Time Domain Discontinuous Galerkin Method"